

②

IDA DOCUMENT D-626

DTIC FILE COPY

PHYSICS OF HIGH-TEMPERATURE AIR
PART II. APPLICATIONS

Ernest Bauer

August 1990

DTIC
ELECTE
NOV 19 1990
S E D

DISTRIBUTION STATEMENT A
Approved for public release;
Distribution Unlimited



INSTITUTE FOR DEFENSE ANALYSES
1801 N. Beauregard Street, Alexandria, Virginia 22311-1772

90 11 19 211

IDA Log No. HQ 89-34632

DEFINITIONS

IDA publishes the following documents to report the results of its work.

Reports

Reports are the most authoritative and most carefully considered products IDA publishes. They normally embody results of major projects which (a) have a direct bearing on decisions affecting major programs, (b) address issues of significant concern to the Executive Branch, the Congress and/or the public, or (c) address issues that have significant economic implications. IDA Reports are reviewed by outside panels of experts to ensure their high quality and relevance to the problems studied, and they are released by the President of IDA.

Group Reports

Group Reports record the findings and results of IDA established working groups and panels composed of senior individuals addressing major issues which otherwise would be the subject of an IDA Report. IDA Group Reports are reviewed by the senior individuals responsible for the project and others as selected by IDA to ensure their high quality and relevance to the problems studied, and are released by the President of IDA.

Papers

Papers, also authoritative and carefully considered products of IDA, address studies that are narrower in scope than those covered in Reports. IDA Papers are reviewed to ensure that they meet the high standards expected of refereed papers in professional journals or formal Agency reports.

Documents

IDA Documents are used for the convenience of the sponsors or the analysts (a) to record substantive work done in quick reaction studies, (b) to record the proceedings of conferences and meetings, (c) to make available preliminary and tentative results of analyses, (d) to record data developed in the course of an investigation, or (e) to forward information that is essentially unanalyzed and unevaluated. The review of IDA Documents is suited to their content and intended use.

The work reported in this document was conducted under contract MDA 903 89 C 0003 for the Department of Defense. The publication of this IDA document does not indicate endorsement by the Department of Defense, nor should the contents be construed as reflecting the official position of that Agency.

This Document is published in order to make available the material it contains for the use and convenience of interested parties. The material has not necessarily been completely evaluated and analyzed, nor subjected to formal IDA review.

Approved for public release; distribution unlimited

IDA DOCUMENT D-626

PHYSICS OF HIGH-TEMPERATURE AIR
PART II, APPLICATIONS

Ernest Bauer

August 1990



INSTITUTE FOR DEFENSE ANALYSES

IDA Independent Research Program

REPORT DOCUMENTATION PAGE

Form Approved
OMB No. 0704-0188

Public Reporting burden for this collection of information is estimated to average 1 hour per response, including the time for reviewing instructions, searching existing data sources, gathering and maintaining the data needed, and completing and reviewing the collection of information. Send comments regarding this burden estimate or any other aspect of this collection of information, including suggestions for reducing this burden, to Washington Headquarters Services, Directorate for Information Operations and Reports, 1215 Jefferson Davis Highway, Suite 1204, Arlington, VA 22202-4302, and to the Office of Management and Budget, Paperwork Reduction Project (704-0188), Washington, DC 20503.

1. AGENCY USE ONLY (Leave blank)		2. REPORT DATE August 1990	3. REPORT TYPE AND DATES COVERED Final--January 1989 to January 1990
4. TITLE AND SUBTITLE Physics of High-Temperature Air Part II, Applications			5. FUNDING NUMBERS IDA Independent Research Program
6. AUTHOR(S) Ernest Bauer			8. PERFORMING ORGANIZATION REPORT NUMBER IDA Document D-626
7. PERFORMING ORGANIZATION NAME(S) AND ADDRESS(ES) Institute for Defense Analyses 1801 N. Beauregard Street Alexandria, VA 22311-1772			
9. SPONSORING/MONITORING AGENCY NAME(S) AND ADDRESS(ES)			10. SPONSORING/MONITORING AGENCY REPORT NUMBER
11. SUPPLEMENTARY NOTES			
12a. DISTRIBUTION/AVAILABILITY STATEMENT Approved for public release; distribution unlimited			12b. DISTRIBUTION CODE
13. ABSTRACT (Maximum 200 words) This document is the second part of a set of notes intended to help the reader become familiar with the specialized literature of several applied topics in the physics of high-temperature air, discussing missile reentry (Chapter 5), nuclear weapons effects (Chapter 6), and some topics in the propagation of electromagnetic radiation through the atmosphere (Chapter 7). It presents a simple overview of some key physical factors, and gives references both to relevant textbooks and to the "gray" literature of technical reports specific to the field. Part I of these notes (IDA Document D-487, May 1990) consists of a general introduction (Chapter 1), a discussion of equilibrium air at temperatures to 10,000 K (Chapter 2), a discussion of the radiation from high-temperature air (Chapter 3), and Chapter 4, which gives a brief discussion of some specific mechanisms for heating the earth's atmosphere, ranging from shock heating through nuclear explosions to solar ultraviolet radiation.			
14. SUBJECT TERMS High-temperature air, reentry physics, nuclear weapons effects, atmospheric transmission, cloud physics, cloud-free line-of-sight			15. NUMBER OF PAGES 178
			16. PRICE CODE
17. SECURITY CLASSIFICATION OF REPORT UNCLASSIFIED	18. SECURITY CLASSIFICATION OF THIS PAGE UNCLASSIFIED	19. SECURITY CLASSIFICATION OF ABSTRACT UNCLASSIFIED	20. LIMITATION OF ABSTRACT SAR

ACKNOWLEDGMENTS

Many people have helped with identifying the specific topics addressed in both parts of this document, with reviewing one or more versions of the document, and with detailed critiques of specific parts of the material. I particularly want to thank Parney Albright,^a Bohdan Balko,^a Larry Bernstein,^b Ricky Byrn,^c Rex Finke,^a Ronald Finkler,^a Forrest Gilmore,^d William Jeffrey,^a Steven Kramer,^a Rich Loda,^a Jeff Nicoll,^a Sol Penner,^e Bill White,^f John Zinn,^g and Marty Zlotnick^h for their contributions. It goes without saying that all remaining errors and obscurities are my sole responsibility; and I would appreciate it if readers give me their comments on how these notes can be improved further.



Accession For	
NTIS GRA&I	<input checked="" type="checkbox"/>
DTIC TAB	<input type="checkbox"/>
Unannounced	<input type="checkbox"/>
Justification	
By	
Distribution/	
Availability Codes	
Dist	Avail and/or Special
A-1	

-
- ^a IDA/STD
 - ^b Spectral Science Inc., Burlington, MA.
 - ^c University of California, San Diego.
 - ^f Mission Research Corp., Nashua, NH.
 - ^g Los Alamos National Laboratory, NM.
 - ^h Nicholls Research Corp., Vienna, VA.

ABSTRACT

This document is the second part of a set of notes intended to help the reader become familiar with the specialized literature of several applied topics in the physics of high-temperature air, discussing missile reentry (Chapter 5), nuclear weapons effects (Chapter 6), and some topics in the propagation of electromagnetic radiation through the atmosphere (Chapter 7). It presents a simple overview of some key physical factors, and gives references both to relevant textbooks and to the "gray" literature of technical reports specific to the field.

Part I of these notes (IDA Document D-487, May 1990) consists of a general introduction (Chapter 1), a discussion of equilibrium air at temperatures to 10,000 K (Chapter 2), a discussion of the radiation from high-temperature air (Chapter 3), and Chapter 4, which gives a brief discussion of some specific mechanisms for heating the earth's atmosphere, ranging from shock heating through nuclear explosions to solar ultraviolet radiation.

CONTENTS

Acknowledgments	iii
Abstract	v
Figures	xi
Tables	xv
Contents (IDA Document D-487).....	xvii
Executive Summary	S-1
5.0 SOME TOPICS IN REENTRY PHYSICS	5-1
5.1 The Nature of the Problem	5-1
5.2 Overview of Reentry Phenomenology	5-3
5.3 ICBM Trajectories	5-11
5.4 Normal Shock.....	5-12
5.4.1 Introduction	5-12
5.4.2 Conservation Laws	5-15
5.4.3 Jump Conditions	5-15
5.4.4 Some Results for Polytropic Gases	5-15
5.4.5 Energy Transfer and Non-Equilibrium Conditions.....	5-16
5.4.6 Numerical Results for the Stagnation Temperature.....	5-18
5.5 Equations of Gas Dynamics	5-18
5.6 Boundary Layer Flow.....	5-21
5.7 Transition from Laminar to Turbulent Flow.....	5-22
5.7.1 Introduction	5-22
5.7.2 "Poiseuille" Flow in a Tube	5-23
5.7.3 Boundary Layer Flow	5-23
5.7.4 Atmospheric Turbulence	5-24
5.8 Some Characteristics of Ablators and Ablation	5-24
5.9 The Optical Signature of a Reentry Vehicle.....	5-25
5.9.1 Introduction	5-25
5.9.2 Typical Shape and Heating of a Generic Reentry Vehicle	5-26
5.9.3 Thermal Emission Signature	5-27
5.9.4 Diffuse Scattering of Sunlight	5-28
5.9.5 Earthshine Scattering	5-30
5.9.6 Signal due to Sunlight Scattered from the Earth or Clouds.....	5-32
5.9.7 Total Signature of a Reentry Vehicle	5-33
5.9.8 Introduction to the Optical Signatures Code (OSC)	5-33

6.0	PRIMER ON NUCLEAR WEAPONS EFFECTS	6-1
6.1	Introduction	6-1
6.2	Nuclear Explosions in the Lower Atmosphere	6-6
6.2.1	Introduction	6-6
6.2.2	Qualitative Description of a Low Air Burst	6-8
6.2.3	A Simple Model of Low-Altitude Fireballs	6-12
6.2.3.1	Fireball Size and Motion	6-12
6.2.3.2	Blast	6-12
6.2.3.3	Thermal Fluence	6-15
6.2.4	Near-Surface Bursts	6-15
6.2.5	Damage Mechanisms in the Lower Atmosphere	6-17
6.2.6	Electromagnetic Pulse (EMP)	6-18
6.3	High-Altitude Nuclear Explosions	6-19
6.3.1	Phenomenology	6-19
6.3.1.1	Introduction	6-19
6.3.1.2	Description of W.W. White	6-19
6.3.1.3	Discussion of the Different Features of Fig. 6.7	6-25
6.3.2	Multiburst Phenomenology	6-26
6.3.3	Heave	6-30
6.3.4	Damage Mechanisms due to High-Altitude Nuclear Bursts	6-37
6.4	Systems Implications of High-Altitude Nuclear Explosions	6-37
6.4.1	Introduction	6-37
6.4.2	Ionization Effects on Radio and Radar Propagation	6-39
6.4.2.1	Electromagnetic Wave Propagation in an Ionized Medium	6-39
6.4.2.2	The Disturbed Ionosphere	6-39
6.4.2.3	Some Design Parameters for EHF Propagation in a Structured Ionized Medium	6-42
6.4.3	Redout: Backgrounds for IR Sensors	6-44
6.5	Quality of the Predictions	6-48
7.0	SOME TOPICS IN THE PROPAGATION OF ELECTROMAGNETIC RADIATION THROUGH THE ATMOSPHERE	7-1
7.1	Introduction	7-1
7.2	Transmission through the Atmosphere: Molecular Absorption	7-4
7.2.1	Introduction	7-4
7.2.2	The Nature of the Problem	7-5
7.2.3	The LOWTRAN Code	7-8
7.2.4	FASCODE, a Line-by-Line Model	7-11
7.2.5	Atmospheric Transmittance/Radiance Above 50 km Altitude	7-11
7.3	Atmospheric Visibility and Aerosols	7-12
7.3.1	Introduction: Visibility	7-12
7.3.2	Atmospheric Aerosols	7-13
7.3.3	Mie Scattering by Small (Spherical) Dielectric Particles	7-14
7.3.3.1	Very Small Particles	7-15
7.3.3.2	Very Large Particles	7-16
7.3.3.3	Angular Distribution	7-16
7.3.4	Rayleigh Scattering by Air Molecules in the Visible and Near-UV	7-17

7.4	Physics of Clouds	7-20
7.5	Cloud-Free Line of Sight (CFLOS) Analyses	7-33
7.5.1	Introduction	7-33
7.5.2	Data Bases	7-34
7.5.3	Some Representative Analyses	7-37
7.5.4	Horizontal Viewing	7-39
7.6	Atmospheric Turbulence	7-42
7.7	Non-Linear Effects for High-Intensity Light Beams	7-46
7.7.1	Introduction	7-46
7.7.2	Thermal Blooming	7-47
8.0	BIBLIOGRAPHY	8-1
APPENDIX E*-- Formal Aspects of the Equations of Gas Dynamics.....		E-1
APPENDIX F -- Some Details of the Calculation of RV Optical Signatures		F-1
APPENDIX G -- The Illumination of a Flat Plate by Earthshine		G1
APPENDIX H -- Electromagnetic-Radiation Effects on Electrical and Electronic Systems		H-1
APPENDIX I -- Scattering of Sunlight from a Cloud		I-1

* Appendices A-D are in Part I of these Notes, IDA Document D-487.

FIGURES

5.1	Energy Transfer on Reentry. (a) Schematic of Slowing-Down and Heating-Up as Function of Altitude. (b) Energy Conversion for ICBM Reentry ($u \sim 7$ km/sec) (c) Energy Conversion for Ultra-High-Speed Reentry ($u \sim 11$ km/sec): Effects of Hot Gas Radiation	5-7
5.2	Schematic of Air Flow Around a Reentry Vehicle	5-8
5.3	Surface Temperature Profiles on a Quartz Phenolic Ablative Reentry Vehicle at Different Altitudes	5-9
5.4	ICBM Trajectories	5-13
5.5	General Characteristics of Boundary Layers	5-21
5.6	Computing the Target Irradiance Due to Solar Scattering	5-29
5.7	Computing the Target Irradiance due to Earthshine Scattering	5-31
6.1	Fireball Expansion (ENW, p. 74) "Breakaway" corresponds to the situation when the hot, incandescent interior of the fireball can be seen through the air shock, which cools and becomes less opaque as it expands--see discussion in Section 6.2.2	6-7
6.2	Nuclear Cloud Rise Height as Function of Yield	6-7
6.3	Thermal Power Emitted from an Air Burst as a Function of Time and Height of Burst.....	6-10
6.4	Variation of Apparent Fireball Surface Temperature with Time in a 20-kt Explosion	6-11
6.5	Peak Overpressure from a 1 Kiloton Free Air Burst for Sea Level Ambient Conditions	6-14
6.6	Dust Mass Lofted into the Stabilized Cloud by a Near-Surface Nuclear Explosion	6-16
6.7	Phenomenology of High-Yield Burst at 200 km Altitude and Midlatitude.....	6-20
6.8	Motion of the Plume Along the Geomagnetic Field Lines	6-22

6.9	Massive Multiburst, Case MS-1.1 (Source: White et al., 1987a). (a) Vertical view showing the location of the bursts over the earth; (b) Total mass density at $t = 1$ minute (60 bursts); (c) Electron density at $t = 1$ minute; (d) Total mass density at $t = 16.7$ minutes (1000 bursts); (e) Electron density at $t = 16.7$ minutes	6-27
6.10	Enhanced Total Density due to Heave from Multiple Nuclear Explosions. (We show the ambient density corresponding to low and high solar activity, and the perturbed density $P(60)$ along the plume corresponding to 60 one-Mt bursts, and the general heave $H(1000)$ due to 1000 one-Mt bursts.) Both Mass and Number Density are Shown, in kg/m^3 and no./cm^3 respectively. High-altitude nuclear test data are indicated	6-31
6.11	Enhanced Plasma Temperature due to Multiple Nuclear Explosions [Calculations for the 1000-burst case MS at (a) $t = 1$ min, (b) $t = 2$ min, and (c) $t = 16.4$ min]	6-32
6.12	Enhanced Ionization due to Single and Multiple Nuclear Explosions as Function of Altitude	6-41
6-13	Limb-Viewing IR Radiance Following a 1-Mt Detonation at 200-km HOB. (a) 85-km Tangent Height, (b) 140-km Tangent Height	6-46
7.1	Atmospheric Transmittance Models: LOWTRAN and HITRAN (now FASCODE) Compared	7-2
7.2	LOWTRAN Empirical Transmittance Function versus EOD	7-10
7.3	Representative Extinction Coefficients for Atmospheric Aerosols as Function of Altitude	7-15
7.4	(Mie) Scattering by a Dielectric Sphere of Refractive Index $N_1 = 1.25$ at Different Wavelengths	7-18
7.5	Scattering from Distributions of Water Droplets (of mean radius $4 \mu\text{m}$) at Different Wavelengths	7-19
7.6	Saturated Vapor Pressure of Water Vapor Over Water and Over Ice as Function of Temperature	7-20
7.7	Latent Heat of Evaporation/Condensation of Water	7-21
7.8	Sedimentation Speed of Water Droplets in the Atmosphere	7-22
7.9	Generic Temperature Profile in the Atmosphere	7-24
7.10	Some "Representative" Cloud Types	7-26
7.11	Steady-State Horizontal Cumulative Wind Speed Profiles (m/sec) for Cape Canaveral Space Center	7-31

7.12	Horizontal Dispersion as Function of Travel Time	7-32
7.13	Probability of CFLOS as Function of Elevation Angle θ and Cloud Cover C, for both U.S. and Soviet/Eastern European Models	7-38
7.14	Limb-viewing observations of aerosol-cloud extinction from the NASA SAM-II sensor at $\lambda = 1 \mu\text{m}$ (SAGE is similar). The maximum in extinction in (a) at 7 km is presumably due to high-altitude clouds	7-40
7.15	Seasonally Derived $1.0 \mu\text{m}$ Transmission Curves From SAGE Plotted as a Function of Tangent Altitude and Probability for Three Northern Hemisphere Latitude Bands	7-41
7.16	Probability of Attaining a Given Tangent Height in Horizontal Viewing as a Function of Horizontal Atmospheric Transmittance	7-43
7.17	Optical Turbulence in the Atmosphere: a Sample of the Parameter C_n^2 as Function of Altitude	7-45
F.1	Simplified Geometrical Profile of an RV	F-3
G.1	Sketch for the Evaluation of Eq. (G.1)	G-4
G.2	The Integral I(b)	G-5
I.1	Scattering Geometry	I-5
I.2	Scattering From a Large Cloud at Different Wavelengths: Effective Diffuse Reflectivity	I-7

TABLES

5.1	A Representative ICBM Trajectory	5-14
5.2	Energy Balance Behind a Normal Shock in Air.....	5-17
5.3	Stagnation Temperature Computed Under Various Conditions	5-18
5.4	Common Aerodynamic Dimensionless Parameters.....	5-20
5.5	Parameters Used Here	5-27
5.6	Representative Numbers for Solar Scattering	5-30
5.7	Earthshine Scattered Target Signal	5-32
5.8	Signal Due to Sunlight Scattered from the Earth or Clouds	5-33
5.9	Total Signature of Reentry Vehicle	5-34
6.1	Typical Energy Distribution from a Nuclear Explosion in Vacuum	6-2
6.2	Total Exposure in Vacuum from a Nuclear Weapon of Yield Y(Mt) at a Range R(km)	6-3
6.3	Atmospheric Transmission for a Horizontal Path thickness of 10-km Length for 3 keV X-rays, 1 MeV Neutrons, and 1 MeV Gamma Rays at Different Altitudes	6-4
6.4	Effects of a Nuclear Weapon Exploded in the Lower Atmosphere	6-4
6.5	Effects of a Nuclear Weapon Exploded in the Upper Atmosphere	6-5
6.6	Propagation Disturbances in a Structured Ionized Medium.....	6-40
6.7	Electromagnetic Propagation Parameters in a Structured Ionized Medium	6-43
6.8	Levels of Understanding of Nuclear Environment	6-49
7.1	High and Total Cloudiness at Representative Locations in the Northern Hemisphere	7-3
7.2	Listing of Different Spectral Regions	7-5
7.3	Complex Refractive Index $m = N_1 - i N_2$ for Different Materials	7-14

7.4	Some Representative Examples of Cloud Properties	7-28
7.5	Representative Scales of Atmospheric Motions	7-30
7.6	A Do-It-Yourself Actual Example of Cloudiness: Cloudiness During 13-31 May 1988 in the Washington, DC, Area	7-35
7.7	Cloud Cover: Mean Horizontal Sizes of Clouds and Spaces Between Them	7-36
F.1	Thermal Emission Signal Computation	F-4
I.1	Scattering Parameters at Different Wavelengths	I-7

CONTENTS--IDA Document D-487*

Acknowledgments	iii
Figures	vii
Tables	viii
EXECUTIVE SUMMARY	S-1
1. INTRODUCTION	1-1
2. COMPOSITION OF HIGH-TEMPERATURE AIR	2-1
2.1 Introduction	2-1
2.1.1 Basic Data for Air	2-1
2.1.2 On Thermodynamic Equilibrium	2-6
2.1.3 Outline of the Chapter	2-6
2.2 Equilibrium Dissociation and Ionization for a Single Species	2-8
2.2.1 Introduction	2-8
2.2.2 Dissociation of Molecular Oxygen	2-8
2.2.3 Ionization of Atomic Oxygen	2-10
2.3 Equilibrium Composition of (Dry) Air As Function of Temperature	2-11
2.4 Effects of Dissociation Energy on Thermodynamic Properties	2-13
2.5 Collisions and Non-Equilibrium Processes	2-20
2.6 Some Comments on Heat Transfer in High-Temperature Air	2-25
3. RADIATION FROM HIGH-TEMPERATURE AIR	3-1
3.1 Introduction	3-1
3.2 Blackbody Radiation	3-2
3.3 Equation of Radiative Transfer	3-8
3.3.1 Without Scattering	3-8
3.3.2 With Scattering	3-9

* For reader convenience, the contents of Part I of this work, published as IDA Document D-487, May 1990, are provided here.

3.3.3	Opacities	3-11
1.	Diffusion Approximation in an Optically Thick Medium	3-12
2.	Emission Approximation in an Optically Thin Medium.....	3-12
3.4	Atomic Line Radiation: Transitions, f-Number and Absorption Cross Section, Line Shape, Curves of Growth	3-15
3.5	Molecular Band Radiation	3-23
3.6	Atomic Radiation in General: Free-Free, Free-Bound, Bound-Bound	3-30
3.7	Absorption Coefficient of High-Temperature Air	3-35
3.8	Radiation From High-Temperature Air	3-40
4.	SOME HEATING MECHANISMS	4-1
4.1	Introduction	4-1
4.2	Reentry Heating	4-2
4.3	Nuclear Fireball	4-7
4.4	Upper Atmosphere	4-12
5.	BIBLIOGRAPHY	5-1
Appendix A--	Electronic Structure of Some Air Atoms and Molecules	A-1
Appendix B--	Partition Function for the Dissociation of a Diatomic Molecule	B-1
Appendix C--	Einstein A- and B-Coefficients, f-Numbers and Band Strengths	C-1
Appendix D--	Excerpts from Physical Constants, USAF, 1985, and U.S. Standard Atmosphere, 1962	D-1

EXECUTIVE SUMMARY

This document is the second part of a set of notes intended to help a new Ph.D. in physics or chemistry (or person of equivalent training) become introduced to the specialized literature in the applied fields of atmospheric nuclear weapons effects, missile reentry, upper atmospheric physics, and remote sensing through the atmosphere. Thus, the document is not a substitute for a course in high-temperature gas dynamics and in atmospheric physics, but it presents a simple overview of some key physical factors and gives references both to relevant textbooks and to the "gray" literature specific to the field.

Part I of these notes (IDA Document D-487, May 1990) consists of a general introduction (Chapter 1), a discussion of equilibrium air at temperatures to approximately 10,000 K (Chapter 2), a discussion of the radiation from high-temperature air (Chapter 3), and--as a bridge to the present Part II--a brief discussion of some specific mechanisms for heating the earth's atmosphere, ranging from shock heating through nuclear explosions to solar ultraviolet radiation (Chapter 4).

The present Part II of the notes begins with Chapter 5, which gives an introduction to reentry physics. This begins by identifying the problem of reentry heating, including a sketch of a typical ICBM trajectory. There follows a discussion of a normal shock in air, of various commonly used approximations to the equations of gas dynamics including boundary layer flow, and brief treatments of the laminar-turbulent transition including the differences between aerodynamic and atmospheric turbulence, and of ablation. The chapter finishes with a simple physical discussion of the optical signature of a reentry vehicle.

Chapter 6 is a primer on nuclear weapons effects. It surveys a typical weapon output, and both low- and high-altitude phenomenology including a discussion of some high-altitude multiburst effects. The chapter closes with a discussion of some systems implications of multiple high-altitude bursts and an indication of the quality of predictions in this field.

Chapter 7 addresses selected topics in the propagation of electromagnetic radiation through the atmosphere. After a discussion of molecular absorption in the atmosphere and of the physics of the LOWTRAN and FASCODE computer codes, there is an overview of

atmospheric visibility and aerosols followed by a discussion of cloud physics and of cloud-free line-of-sight (CFLOS) analyses. The chapter closes with a brief discussion of atmospheric turbulence in its effects on electromagnetic signal propagation and a sketch of some non-linear effects that can become important for high-energy laser propagation.

5.0 SOME TOPICS IN REENTRY PHYSICS

5.1 THE NATURE OF THE PROBLEM

An ICBM or a satellite entering the earth's atmosphere from low earth orbit has an effective entry speed of approximately 7 km/sec, or Mach Number $M \sim 20$. During its descent to the surface of the earth a large fraction of its kinetic energy of directed motion will be transformed into heat as a result of frictional resistance of the atmosphere. The kinetic energy involved is $\sim 2 \times 10^7$ joule/kg, which is an order of magnitude greater than the latent heat of vaporization of water, or of the same magnitude as the vaporization energy of carbon, which is one of the highest values known for this quantity. Thus the problem of designing a reentry vehicle which would dissipate or reject this amount of energy is a very severe one; it was solved in the 1955-58 time frame.

The initial plan was to let the vehicle reenter relatively gradually so that the thermal energy could be radiated away. Experimental work with shock tubes, rocket exhausts, etc., showed that the radiant heat load on the vehicle was not nearly as severe as had been thought because a 1.0-cm-thick layer of hot air does not radiate nearly as much as a blackbody at the same temperature (see, e.g., Section 3.8 of Part I). It proved possible to use an ablative heat shield, in which the entry vehicle is coated with materials that decompose, rejecting large quantities of energy per unit mass of the ablator.

For orientation, an ICBM is designed for high-speed reentry. Its peak heating occurs near 20 km, and its peak deceleration is ~ 50 g; it uses an ablative heat shield. The Space Shuttle or other manned entry vehicle is limited to very much lower deceleration; the Shuttle flies a lifting reentry with peak deceleration ~ 1 g. Its peak heating occurs near 60 km and it dissipates frictional heat by radiation, using special tiles for heat protection.

A typical reentry vehicle has dimension of order 1.0 m, so that it has a significant encounter with the atmosphere only at densities sufficiently high for the gas-kinetic mean free path l_{gk} (defined in Section 2.5 of Part I) to be smaller than 1.0 m, which requires

altitudes below ~ 130 km.¹ Thus a *shock* gradually develops in front of the vehicle as it descends below this altitude; a *boundary layer* (which is perhaps 1.0 cm thick) can only develop where the mean free path is much less than the boundary layer thickness, or at altitudes below ~ 85 km. Section 5.2 gives a brief overview of some aspects of reentry phenomenology, and the rest of this Chapter expands on that discussion.

Section 5.3 reviews ICBM trajectories and sketches how the Space Shuttle differs from this. Section 5.4 gives a discussion of a normal shock for the case of a polytropic gas.² Section 5.5 gives a broad overview of hypersonic aerodynamics, introducing the various dimensionless parameters that are used in this field; it is supplemented by Appendix E which derives the equations of gas dynamics (which are representations of the conservation of mass, momentum, and energy) from the Boltzmann equation. This leads naturally to the Euler and Navier-Stokes equations, including the empirical characterization of viscosity and heat conductivity coefficients in laminar flow. Section 5.6 sketches an application of the equations of fluid mechanics to boundary layer flow, with a qualitative indication of how the airflow around a hypersonic vehicle can be represented. As the vehicle enters the denser atmosphere the air flow in the boundary layer becomes turbulent, and so the transition from laminar to turbulent flow is taken up in Section 5.7, where some elements of this large and difficult topic are discussed. The key point is that frictional heat transfer is much larger in turbulent than in laminar flow. Some characteristics of ablation and ablative materials used for thermal protection of high-performance reentry vehicles are mentioned in Section 5.8.

The various topics addressed here in cursory fashion are intended to provide an indication of some of the factors that have to be considered in the phenomenology of reentry vehicles. The final section of this chapter gives an introduction to the optical (visible and infrared) signature of a reentering body. The discussion is qualitative and closes with an introduction to the Optical Signatures Code (OSC) which provides quantitative answers to these questions. This code embodies a great deal of experience from reentry physics, in effect codifying the various elements that have been discussed here and their overall application to missile reentry.

¹ At higher altitudes there are occasional collisions which slow down a spacecraft only gradually and cause a satellite in a 200-km orbit to de-orbit in a time of order one year.

² A *polytropic* gas is one with $\gamma = c_p/c_v = \text{constant}$. This does not apply to air under reentry conditions because of the dissociation of O_2 --see Part I, Section 2.4.

5.2 OVERVIEW OF REENTRY PHENOMENOLOGY

When an ICBM or low-earth-orbiting satellite traveling at hypersonic speed³ enters the earth's atmosphere, it is slowed down by collision with air molecules. This produces a *hypersonic shock wave* that stands off in front of the vehicle. At still lower altitudes (or higher densities) a *boundary layer* is produced on the vehicle.

During the slowing down of a vehicle in atmospheric entry, its kinetic energy is transformed into thermal energy of the surrounding air, and some of this thermal energy reaches the surface of the vehicle. Figure 5.1a shows schematically how the atmospheric density, velocity, deceleration and heating rate change with altitude, indicating how, as the vehicle enters the denser lower atmosphere, its velocity gradually decreases, with peaks in deceleration and in heating rate at intermediate altitudes (30-60 km). Figures 5.1b and 5.1c demonstrate in semi-quantitative form how energy is converted. In Figs. 5.1b and 5.1c we show the energy conversion fraction, which is that fraction of the kinetic energy lost by the vehicle which reaches the surface, as a function of altitude.

At very high altitudes in the *free molecular flow regime* where the gas kinetic mean free path l_{gk} is not small compared to critical vehicle dimensions, as much as half of the kinetic energy lost by the vehicle appears as heat input to the body. At lower altitudes in the *continuum* regime,⁴ a boundary layer of hot air develops around the reentry vehicle and transfers thermal energy to the vehicle, mainly by conduction and convection at speeds of around 7 km/sec. Note that while the energy conversion fraction here may be only 0.01 because most of the energy goes into the air, yet here the heat load on the vehicle will be much greater than in the free molecular flow regime because the total energy transferred is so much larger.

Figure 5.1b shows a representative variation of energy conversion fraction with altitude for a relatively blunt vehicle traveling at ICBM velocity of about 7 km/sec. Note the transition from laminar to turbulent convection in the 30-km altitude range.

If a vehicle travels at ICBM velocity (or low earth-orbiting velocity, which is only about 10 percent higher--cf., e.g., Gazley, 1961), when it transfers all its kinetic energy

³ *Supersonic* means that the vehicle velocity v is greater than the local sound speed a ; *hypersonic* means that the velocity v is very much greater than the local sound speed a . For low earth orbit and ballistic missile reentry we typically have a *Mach number* $M = v/a \sim 20$.

⁴ This is said to occur when the gas-kinetic mean free path l_{gk} is very much smaller than a critical vehicle dimension.

into thermal energy of air, the peak air temperature ("stagnation temperature" defined in Section 5.4) is in the range 6000 - 8000 K, (depending on pressure) with O₂ largely and N₂ partly dissociated. For super-orbital or near escape velocity of 11 km/sec the enthalpy of air is increased by a factor $(11/7)^2 \sim 2.5$, and the stagnation temperature is somewhat higher (8000-10,000 K) but now radiative heat transfer (which goes as T^4 rather than as $\text{grad } T$) becomes important at the lower altitudes, in addition to conductive and convective heat transfer. Figure 5.1c shows schematically how gaseous radiation effects become important at low altitudes for these very high velocities, changing the energy conversion fraction.

Figure 5.2 gives an overview of the air flow around a non-lifting (i.e., ballistic) reentry vehicle. It demonstrates:

1. The *shock wave A* associated with the encounter of the vehicle moving through the ambient air, which is thereby displaced non-adiabatically by the vehicle. Except at the *front stagnation point B* where the shock is normal, this is an oblique shock which extends downstream, typically for many vehicle lengths, and then gradually fades out.
2. The *stagnation point B* is that region in the flow in which all the kinetic energy of directed motion is transformed into thermal energy, so that the maximum temperature in the flow or stagnation temperature is attained here.⁵
3. The *boundary layer C*, which begins in the stagnation region at the front of the vehicle and then gradually grows as it moves downstream along the body. In hypersonic flow this is a region close to a solid body in which the ambient air interacts with the solid boundary through collisions, certainly through frictional (viscous) interactions and sometimes also through ablation or other chemical reactions. Within the boundary layer the flow is generally subsonic and can be treated as incompressible but viscous--i.e., collisional interactions with the body are important. Outside the boundary layer the flow is treated as supersonic, i.e., compressible, so that the flow equations are non-linear and thus difficult to solve, but the detailed interaction of the flow with the body is not important.
4. Past the downstream end of the body the flow has to revert gradually to the original undisturbed flow. This is a complex process:

⁵ See Fig. 5.3, which shows that the peak or stagnation temperature is reached at the blunt nose of the RV. Table 5.2 (below) gives the energy balance behind a normal shock in air, and shows that for ICBM or even IRBM entry ($u_0 = 7$ km/sec and 5 km/sec respectively) more energy goes into O₂ dissociation than into any other degrees of freedom.

- 4.1 Behind the body the boundary layer continues as the *shear layer* which thickens gradually but shrinks down to form a minimum width or *neck D* before expanding gradually to form a *wake E* which extends downstream for many vehicle lengths before gradually fading out like the bow shock *A*.
- 4.2 Between the end of the body and the neck, and inside the shear layer there is the *recirculation region F* which is filled by air flowing out of the shear/boundary layer proper; the character of the flow is shown in Fig. 5.2.
- 4.3 Note that near the rear of the recirculation region there is a *rear stagnation point G* where the temperature becomes almost as large as at the front stagnation point.⁶
- 4.4 The wake itself produces a *trailing shock*.
5. Note that there is a *Prandtl-Meyer expansion fan H* associated with a turning of the boundary layer past the end of the body.
6. There may also be a secondary shock near the front of the vehicle where the shape changes from hemispherical to conical, and for vehicles of more complex shape (e.g., sphere-cylinder-conical flare) there will be similar shocks and expansion fans associated with every turning of the flow.
7. If one asks for the mean temperature of the flow field surrounding the body, there is a maximum at the stagnation point (typically 7500 K for ICBM reentry); in the boundary layer along the body the temperature is very much less--typically 2000-3000 K for an ablating vehicle.⁷ Past the rear of the body the temperature varies with location, with a maximum at the rear stagnation point, but in the wake proper beyond the neck the temperature gradually decreases to its ambient value.

Figure 5.3 shows the temperature profile at various stations along a "high-performance" ablatively cooled entry vehicle at different altitudes. At very high altitudes the peak temperature develops first on the rounded (i.e., blunt) nose, and then gradually, as the boundary layer builds up, so does the frictional heating along the side of the body. This heating (which at flow velocities below approximately 10 km/sec is due mainly to conduction and convection rather than to radiation) increases down to the altitude of peak heating which here occurs at 70,000 ft (21 km). The heating rate then declines. Note the

⁶ The temperature here is not quite as large as at the front stagnation point because of various energy losses in the flow.

⁷ Figure 5.3 gives some representative temperature profiles along an ablative reentry vehicle at different altitudes.

sudden increase in temperature at station 36 in. at 90,000 ft. altitude. This is due to the transition from laminar to turbulent flow. The precise character of transition varies-- Fig. 5.3 comes from a computer calculation.

The discussion centering on Figs. 5.1-5.3 demonstrates many of the significant physical factors that contribute to reentry phenomenology, but it is evidently not an adequate account of hypersonic aerodynamics. However, it does introduce and set in context a number of the physical concepts that are discussed later, in particular hypersonic shocks (Section 5.4), the characteristics of the equations of fluid mechanics and their approximations (Section 5.5), the concept of a boundary layer (Section 5.6), the laminar-turbulent transition (Section 5.7), and the significance of ablation (Section 5.8).

Note that, e.g., Anderson (1986) indicates that there are five distinct effects characterizing hypersonic flows:

1. There is a shock wave on the body close to its surface, i.e., a thin shock layer.
2. Viscous effects are strong and can dominate the flow field by thickening the boundary layer and merging the shock into the viscous layer.
3. At low densities there can be temperature and velocity discontinuities ("slip conditions") at the surface of the body.
4. Hypersonic flows are high-energy flows, leading to non-ideal behavior of the gas flowing around the body. The principal effects are vibrational excitation and dissociation which lead to a change in specific heats, in specific heat ratio $\gamma = c_p/c_v$, and also in chemical composition.
5. In hypersonic flow over a blunt-nosed body, the shock wave around the body is highly curved and there is a vorticity (angular momentum) interaction.

Items 1-3 and 5 are discussed in the aerodynamics literature, see, e.g., Anderson 1982, 1984, 1986, while item 4 is discussed in Chapter 2 of Part I.

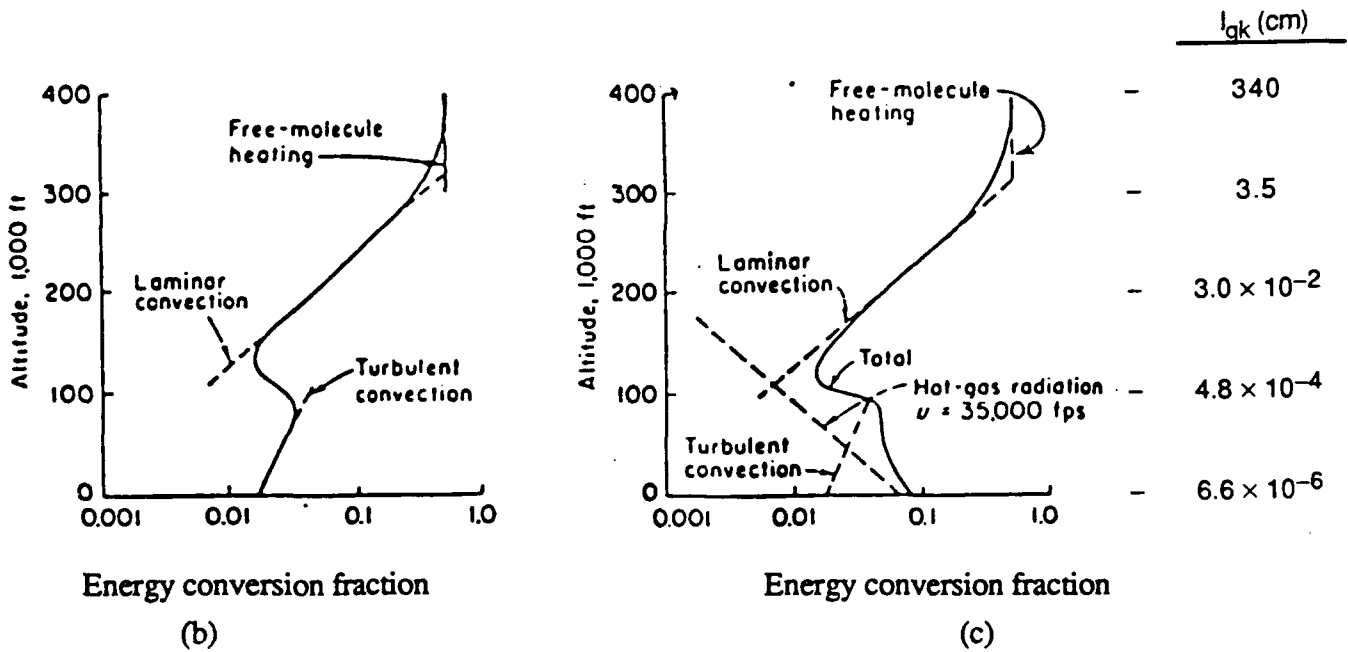
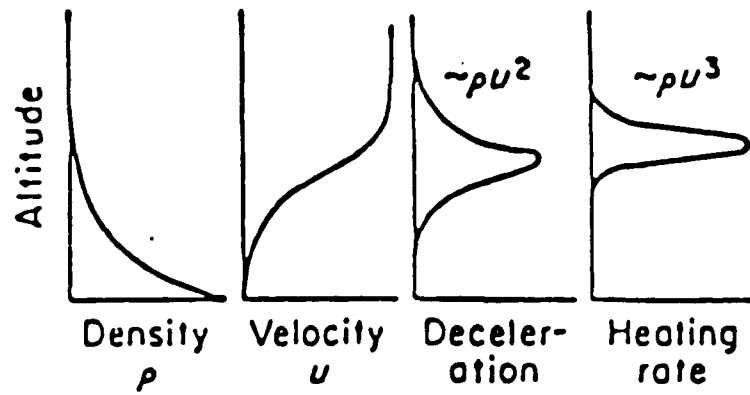


Figure 5.1. Energy Transfer on Reentry. (a) Schematic of Slowing-Down and Heating-Up as Function of Altitude. (b) Energy Conversion for ICBM Reentry ($u \sim 7$ km/sec) (c) Energy Conversion for Ultra-High-Speed Reentry ($u \sim 11$ km/sec): Effects of Hot Gas Radiation. (Source: Gazley, 1961)

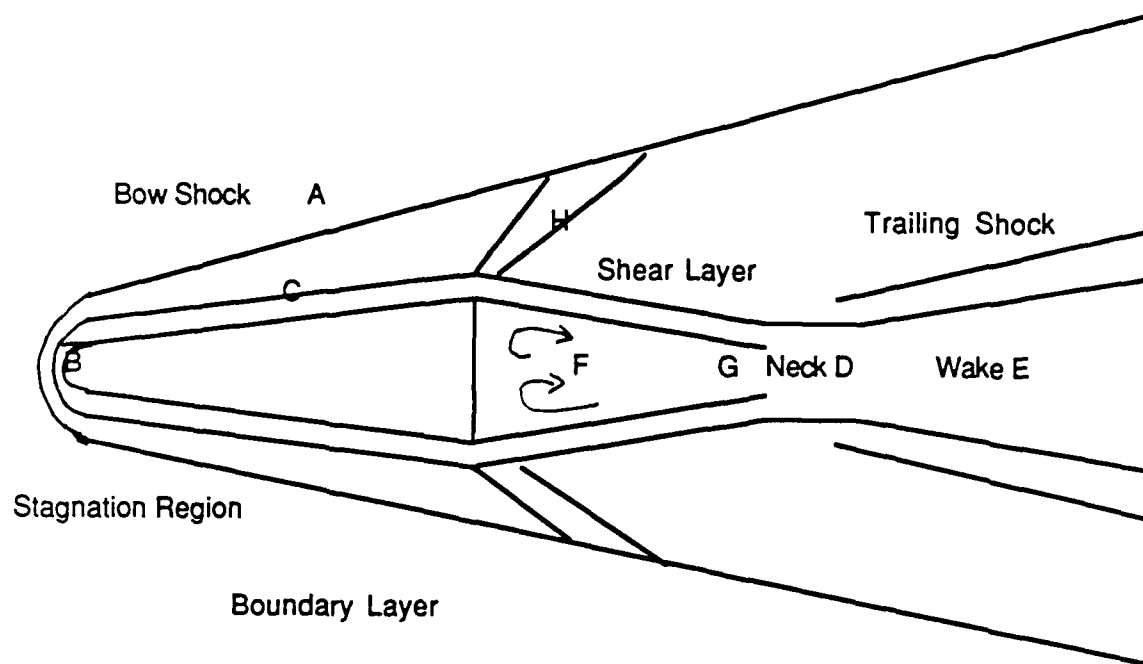


Figure 5.2. Schematic of Air Flow Around a Reentry Vehicle

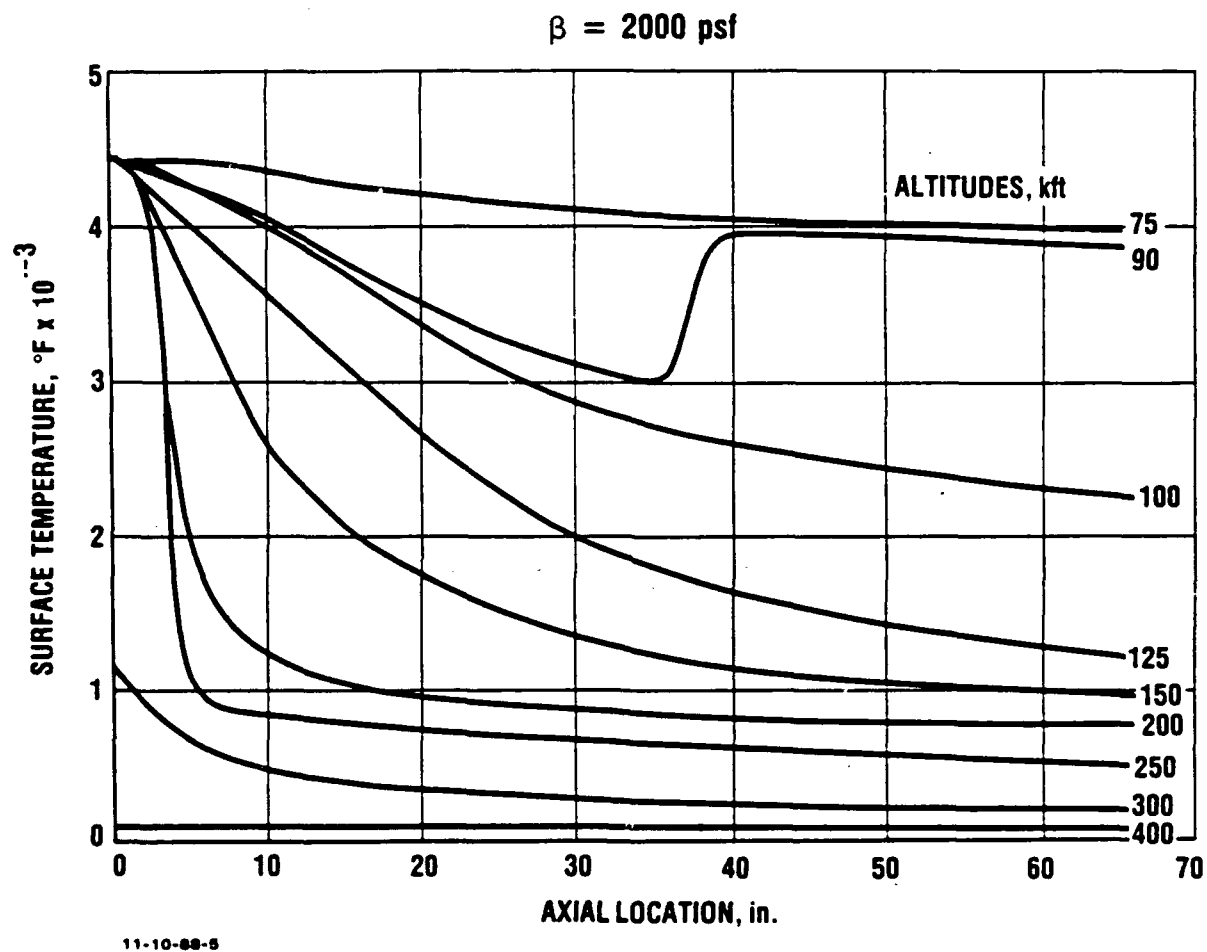


Figure 5.3. Surface Temperature Profiles on a Quartz Phenolic Ablative Reentry Vehicle at Different Altitudes (from R. Bartle, AVCO Systems Division)

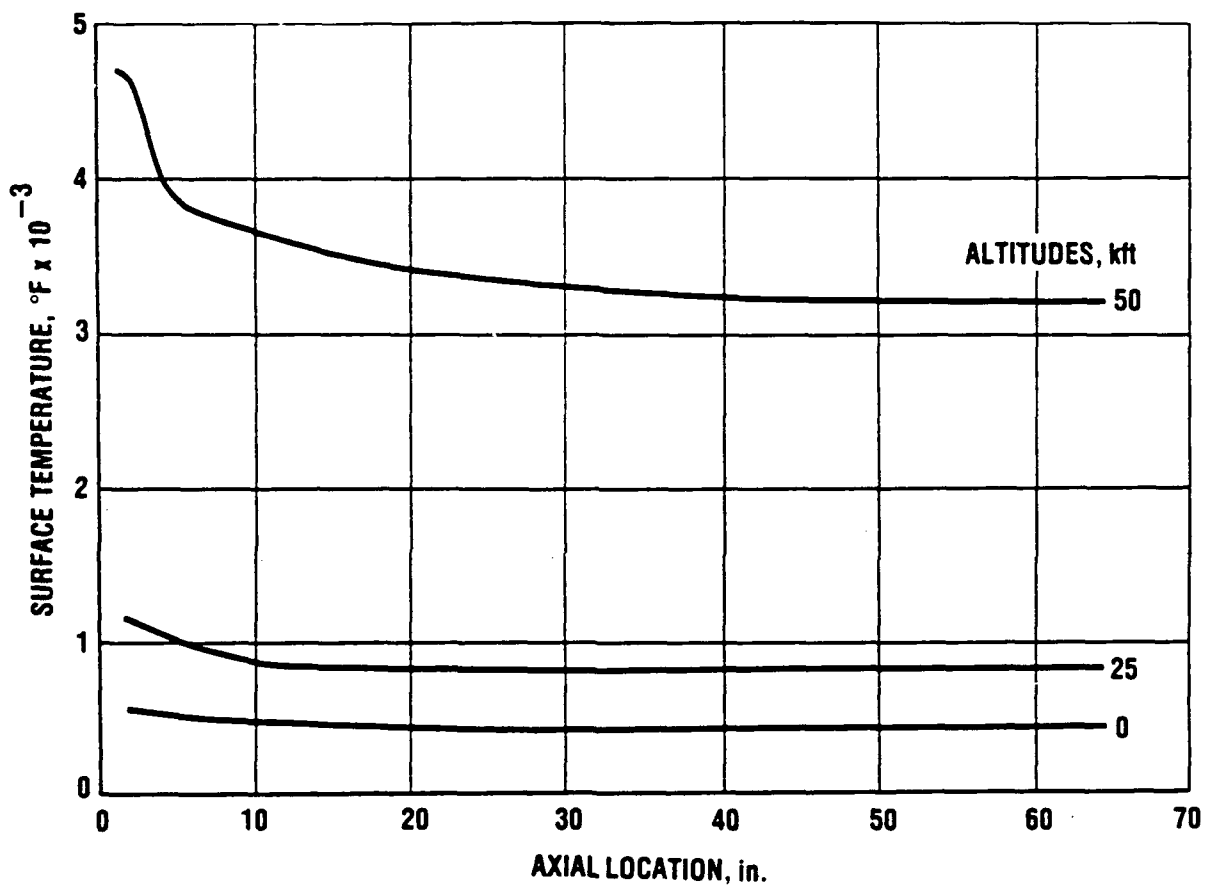


Figure 5.3. (continued)

5.3 ICBM TRAJECTORIES

Figure 5.4 shows some representative trajectories for an Intercontinental Ballistic Missile (ICBM) of range 9000 km. It shows the altitude, with time markers every 30 sec from burnout, for four different trajectories. These are customarily characterized by the reentry angle, which is defined as the path angle to the horizontal at 400,000 ft (122 km) altitude during reentry or at booster burnout. These both typically occur near 400,000 ft altitude.

A normal or minimum energy trajectory corresponds roughly to 24-deg reentry angle. A depressed trajectory (15-deg reentry angle) would make the ICBM harder to detect from space because of its lower maximum height; more energy is needed to overcome frictional heating in the atmosphere. A lofted trajectory (35-40 deg reentry angle) requires more energy to send the ICBM higher above the earth's surface. The range of reentry angles, 15 deg to 40 deg, roughly covers the range considered.

Table 5.1 gives some details of the trajectory for a "representative" 10,000-km, minimum-energy trajectory. It is shown here to let the reader see how various parameters change along the trajectory. As a function of time, we show the horizontal range, altitude, velocity, path angle γ to the horizontal, and a representative stagnation temperature⁸ T_1 along the trajectory. In the reentry phase we also show the large (negative) acceleration and the ballistic coefficient β ⁹

$$\beta = W/C_D A , \quad (5.1)$$

where W = mass of vehicle , A = projected area, and C_D = drag coefficient.¹⁰ β changes slightly along the entry trajectory, principally because C_D changes with velocity, including effects of the laminar-to-turbulent transition.

For a representative ICBM trajectory with a 23-deg reentry angle, peak heating (for a vehicle with $\beta \sim 2000 \text{ lb/ft}^2$) occurs at 23 km (75,000 ft) with a peak deceleration of

⁸ The values of T_1 shown here correspond to a particular value of spherical nose radius. They assume equilibrium radiation and no thermal inertia, so that the numerical values are representative rather than accurate. They do display exit heating as well as entry heating. An ambient value $T = 300 \text{ K}$ is assumed, so that significant heating only occurs for T_1 different from 300 K.

⁹ β is normally measured in lb/ft^2 ; $2000 \text{ lb/ft}^2 = 9774 \text{ kg/m}^2$ is a representative value for the present generation of ablatively cooled reentry vehicles. (For a satellite, values of $50\text{-}200 \text{ kg/m}^2$ are typical, giving rise to lifetimes of order several years in 400-500 km orbits.)

¹⁰ $C_D = 2$ for a flat plate normal to the flow, and $C_D = 2 \sin^2\theta$ for a cone of half-angle θ .

50-60 g. By contrast, the first generation of U.S. reentry vehicles (1957-1960 time frame) used a copper heat sink with $\beta \sim 100 \text{ lb/ft}^2$, so that peak heating occurred near 50 km (150 kft) and extended over a much longer time so that radiative heat transfer was adequate to dissipate the slower rate of heat generation; the peak deceleration was of order 10 g. The first U.S. manned space vehicle (Mercury) used a somewhat similar reentry technology, but all subsequent U.S. manned space vehicles have flown a lifting reentry which can be much gentler than a ballistic trajectory. Thus the Space Shuttle reentry angle is approximately 1 deg and its peak heating occurs near 61 km (200,000 ft); its peak deceleration is $\sim 1 \text{ g}$. The Shuttle, with its much slower reentry and thus lower heating rate than an ICBM, uses radiative cooling and is covered with tiles which dissipate excess thermal energy by radiation, unlike ballistic missiles which have ablative heat shields.

5.4 NORMAL SHOCK

5.4.1 Introduction

A normal shock is the most violent elementary discontinuity that one studies in aerodynamics. It is a one-dimensional motion which is observed when a supersonic gas flow strikes a flat plate located perpendicular to the flow direction; or equally, when a flat plate (piston) moves supersonically into a stationary gas. The flow behind the discontinuity is always subsonic. A shock is adiabatic but non-isentropic.

We use the following notation:

upstream/supersonic = subscript 1

downstream/subsonic = subscript 2

ρ = density

u = flow velocity

a = sound speed

e = internal energy per gm = $\int_0^T (C_v/M) dT$

h = $e + p/\rho$ = enthalpy per gm = $\int_0^T (C_p/M) dT$

M = molecular weight.

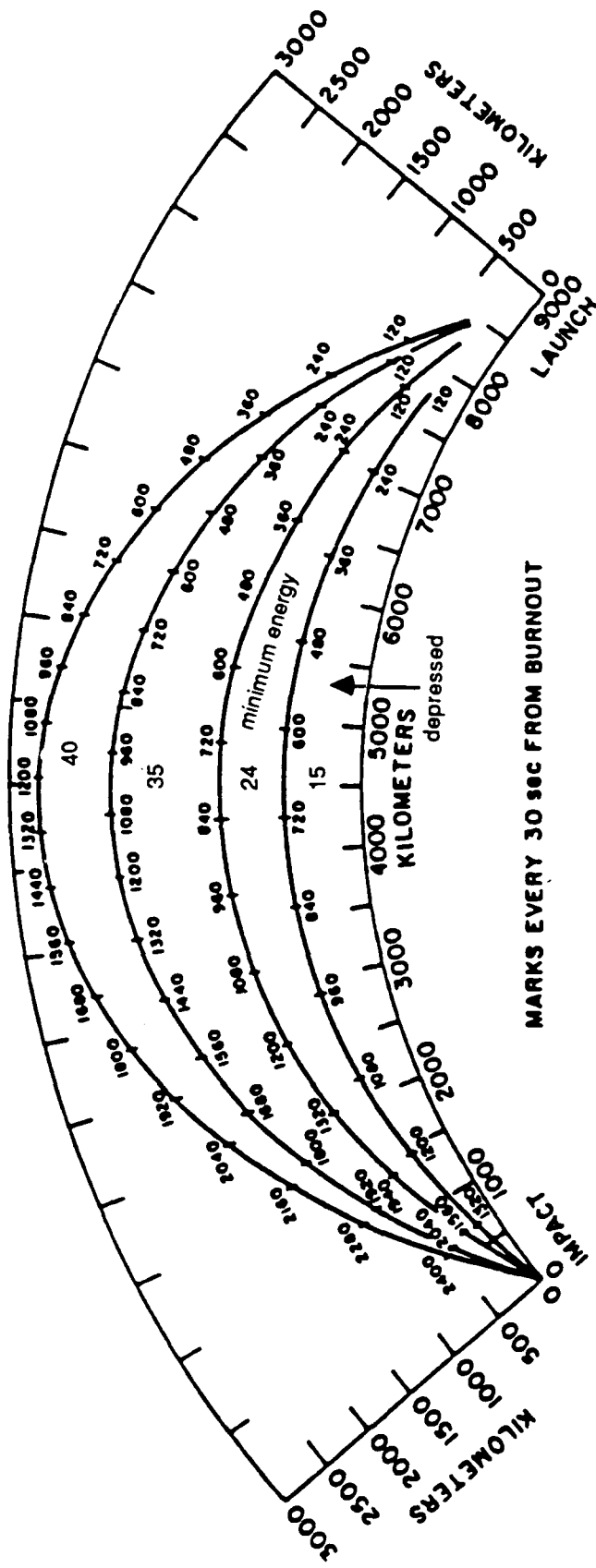


Figure 5.4. ICBM Trajectories (Source: APS, 1987)

Table 5.1. A Representative ICBM Trajectory

Time(sec) (sec)	Range (km)	Altitude (km)	Velocity (km/sec)	Acceleration (g)	β (kg/m ²)	Path angle (deg.)	T ₁ (K)	
0	0	0	0			90	300	
43	5.1	10.2	0.61			54.3	970	
60	13.8	20.6	1.01			46.7	1180	
74	26.0	32.4	1.45			42.2	1240 (M)	
90	47.4	50.7	2.12			38.5	1200	
105	77.8	74	2.96			36.2	1060	Stage 1 Burnout
121	116	101	3.06			34.2	475	
150	194	151	3.44			30.8	300	
210	398	263	4.64			25.5		
263.5	656	385	6.70			23.4	300	Stage 2 Burnout
463	1740	857	6.13			19.6		Stage 3 Burnout
1176	4930	1580	5.77			0.0		Apogee
1890	8120	855	6.12			-19.7		
2100	9260	355	6.75			-23.6	300	
2180	9750	129	7.05		1610	-24.7	300	
2182	9770	120	7.06		523	-24.8	540	
2193	9830	90.2	7.10		4070	-24.9	1480	
2203	9890	60.1	7.14		6730	-25.0	2950	
2213	9960	29.9	7.04	6.0	7330 (M)	-25.2	4950	
2218	9990	15.7	6.01	44	7240	-25.3	5790(M)	
2220	10000	11.0	4.94	63 (M)	7200	-25.4	5440	
2230	10020	0	0.96	17	3380	-27.6	1750	

* Data kindly provided by R.E.Finke, IDA/STD.

We consider a *polytropic* gas for which

$$C_p/C_v = \text{constant} = \gamma = 1 + 1/s \quad , \quad (5.2)$$

where $s = 1/(\gamma - 1)$. For an ideal monatomic gas, $\gamma = 5/3$, for an ideal diatomic gas $\gamma = 7/5$, but for dissociating air (i.e., at temperatures in the range 2000-6000 K), $\gamma' \sim 1.15$ (see, e.g., Gilmore, 1955, p. 67). For a polytropic gas

$$p/\rho = RT/M ; e = sRT/M ; h = (1 + s) RT/M \quad . \quad (5.3)$$

Indeed, $e \sim T$ is the definition of a polytropic gas.

5.4.2 Conservation Laws

The conservation laws for mass, momentum, and energy are

$$\rho_1 u_1 = \rho_2 u_2 = m \text{ (constant)} \quad (5.4)$$

$$p_1 + \rho_1 u_1^2 = p_2 + \rho_2 u_2^2 = P \text{ (constant)} \quad (5.5)$$

$$h_1 + (1/2) u_1^2 = h_2 + (1/2) u_2^2 = [(1/2) (\gamma + 1)/(\gamma - 1)] a^*{}^2 \quad , \quad (5.6)$$

where

$$a^*{}^2 = u_1 u_2 \quad . \quad (5.7)$$

5.4.3 Jump Conditions

It is convenient to introduce a density ratio

$$\epsilon = \rho_1/\rho_2 = u_2/u_1 \quad , \quad (5.8)$$

which characterizes the strength of the shock. Given conditions upstream of the shock (u_1, T_1, ρ_1 , or p_1) and the equation of state, then when the density ratio ϵ is specified, so are conditions downstream of the shock. In particular, there is a *Hugoniot* condition

$$h_2 - h_1 = (1/2) u_1^2 (1 - \epsilon^2) \quad (5.9)$$

or

$$p_2 - p_1 = \rho_1 u_1^2 (1 - \epsilon) \quad . \quad (5.10)$$

5.4.4 Some Results for Polytropic Gases

These results are specific for polytropic gases, but comparable results apply to air--the Mollier chart--see, e.g., Feldman (1957), Logan and Treanor (1957). We have

$$a_2^2/a_1^2 = A + B M_1^2 \text{ where } M_1 = u_1/a_1 \quad (5.11a)$$

$$\text{and } A = 2s B ; B = 1/(2s + 1) \quad (5.11b)$$

$$\epsilon = A/M_1^2 + B \quad (5.11c)$$

$$T_2/T_1 = 1 + M_1^2 (1 - \epsilon^2)/2s \quad (5.11d)$$

$$p_2/p_1 = (1/\epsilon) (T_2/T_1) . \quad (5.11e)$$

Notice that as $M_1 \rightarrow \infty$, $\epsilon \rightarrow B$, and we have the following:

$$\text{Monatomic ideal gas: } \gamma = 1.67, s = 3/2 ; B = 1/4 \quad (5.12a)$$

$$\text{Diatomic, polytropic gas (e.g., undissociated air): } \gamma = 1.4, s = 5/2 ; B = 1/6 \quad (5.12b)$$

Dissociated air [very rough, see Gilmore (1955), p. 67]:

$$\gamma' = 1.15 ; s = 20/3 ; B = 0.07 . \quad (5.12c)$$

Thus the density ratio ϵ across the shock remains finite but the temperature ratio can become very large: $T_2/T_1 \sim M_1^2 \rightarrow \infty$ as $M_1 \rightarrow \infty$, so that large flow velocities give very high "stagnation" temperatures and pressures, but only moderate increases in density.

5.4.5 Energy Transfer and Non-Equilibrium Conditions

A shock is in fact not an instantaneous discontinuity, but has some finite thickness and structure. This is determined by the transfer of energy from initial kinetic energy into various degrees of freedom. Figure 4.2(c) in Part I shows the effects of kinetics: translational and rotational equilibration occurs very rapidly, giving a high translational temperature immediately across the shock as all the directed energy of motion is transformed into random translational and rotational energy. Transfer into vibrational excitation takes longer and leads to a lower temperature as the energy is distributed among more degrees of freedom. Dissociation and electronic excitation take longer still, giving yet a further reduction in kinetic temperature while ionization is slower still, yielding the final equilibrium temperature. Table 5.2 shows the actual energy distribution for a normal shock in air at 5-7 km/sec where most of the energy goes into dissociation, a significant amount into vibrational excitation, and very little into ionization. By contrast, for a normal shock in Argon most of the energy goes into ionization--see, e.g., Bauer, 1969.

Table 5.2. Energy Balance Behind a Normal Shock In Air (Source: Bauer, 1969)

(A velocity of 5 km/sec corresponds to IRBM entry while 7 km/sec corresponds to ICBM entry.
The ambient conditions are $p_o = 0.01$ atm., $T_o = 294$ K,
and energies are listed in eV/molecule or atom.)

u_o	5 km/sec	7 km/sec
Upstream of the shock		
Directed kinetic energy	3.76	7.3
Thermal enthalpy $c_p T$	0.006	0.006
Downstream of the shock		
Stagnation temperature (K)	5800 (~ 0.5 eV)	7500 (~ 0.65 eV)
Enthalpy of translation (3/2) kT	1.25	1.62
Rotational enthalpy, kT	0.5	0.65
Vibrational enthalpy	0.37	0.51
Dissociation energy	1.51	2.72
Electronic energy	0.011	0.075
Ionization energy	0.002	0.006
Chemical energy ($N_2 + O_2 \rightleftharpoons 2NO$)	-0.02	-0.01
Equilibrium composition downstream of the shock		
[N ₂]	0.579	0.304
[NO]	0.0164	0.00615
[O ₂]	0.000974	0.000124
[N]	0.0840	0.418
[O]	0.319	0.272
[e ⁻] = [NO ⁺]	0.000137	0.000630

5.4.6 Numerical Results for the Stagnation Temperature

Some results for T_2 (for $T_1 = 294$ K so that $a_1 = 343.8$ m/sec) are shown in Table 5.3 where we compare the results for an ideal monatomic gas (see Eq. 5.12a), a diatomic non-dissociating gas (see Eq. 5.12b) and calculations for dissociating air with $\gamma' = 1.15$ (see Eq. 5.12c) with the numerical calculations for air and Argon.

Table 5.3. Stagnation Temperature Computed Under Various Conditions
($T_1 = 294$ K, i.e., $a_1 = 343.8$ m/sec)

u_1 (km/sec)	5	7	10.7
$M_1 = u_1/a_1$	14.5	20.4	31.1
Stagnation Temperature (K):			
Ideal monatomic gas (Eq. 5.12a)	19,600	38,500	89,300
Argon (see Bauer, 1969)	13,000	15,700	—
Undissociated air (Eq. 5.12b)	12,300	24,100	55,700
Air (see Table 5.2)	5800	7500	—
Dissociated polytropic air (Eq. 5.12c)	4900	9400	21,600

Note that the results for dissociated air depend on density and are only schematic, because for dissociating air enthalpy e depends on both p and T in a complicated way. The value of γ' is not a constant. One sees that in the case of dissociating air a large amount of energy goes into breaking chemical bonds while in Argon a large amount of energy goes into ionization. Table 5.2 shows that the other available internal degrees of freedom also take up significant amounts of energy--evidently, the more the internal energy, the lower the stagnation temperature.

5.5 EQUATIONS OF GAS DYNAMICS

To solve fluid mechanical flow problems, one has to write down the equations of motion which correspond to the conservation of mass, momentum, and energy, together with appropriate collisional (dissipative) terms, and terms arising from chemical reactions (mainly dissociation) and from ablation. These are five equations in the five variables (three velocity components, density and pressure), but they are a set of coupled non-linear partial differential equations which are too difficult to solve without approximation using present computational power: certainly in the 1930s to 1960s time frame when most basic work in this field was done it was necessary to make some very significant approximations.

Appendix E sketches how one can derive the various approximations, in particular the Euler and the Navier-Stokes equations, from the Boltzmann equation, and also gives simple expressions for the gas kinetic transport coefficients (viscosity, thermal conductivity, and diffusion coefficient). Here we give an overview of the physical content of these equations. The Euler equations correspond to a perfect fluid which cannot sustain tangential (shearing) forces, only normal (pressure) forces. They are useful under many conditions, but they do not work near surfaces because they cannot explain the drag force on a surface in a fluid (because they do not have a viscous drag term). The Navier-Stokes equations do have viscous and thermal conduction terms, and thus are more generally applicable but correspondingly more difficult to evaluate. In the boundary layer, the flow interacts with a surface, so that the viscous terms are important and one has to use the Navier-Stokes equations--but because the flow is subsonic, it can be treated as incompressible, which is a great simplification that will now be demonstrated.¹¹

Compressibility is a measure of the change of volume ΔV under an external force, here the pressure p . Thus, we may define a modulus of elasticity E by the equation

$$\Delta p = -E (\Delta V/V_0) . \quad (5.13)$$

For a gas, $E = p_0$, the initial pressure, and the relation between changes in density ρ and volume V is

$$\Delta \rho / \rho_0 = -\Delta V / V_0 , \quad (5.14)$$

so that

$$\Delta p / p_0 = \Delta \rho / \rho_0 , \quad (5.15)$$

i.e., the flow can be treated as incompressible if $\Delta \rho / \rho_0 \ll 1$. Now from Bernoulli's equation

$$p + (1/2) \rho u^2 = \text{constant} , \quad (5.16)$$

where u = flow velocity, we find

$$\Delta \rho / \rho_0 = (1/2) \rho_0 u^2 / E = (1/2) \rho_0 u^2 / p_0 = (1/2) (u/a)^2 , \quad (5.17)$$

so that the effects of compressibility can be ignored if $M^2/2 \ll 1$, where $M = u/a$ is the Mach number.

Traditionally, aerodynamicists use similarity solutions to a great extent, with a number of dimensionless parameters. The common dimensionless parameters are listed in Table 5.4 together with an indication of their physical meaning. The most important ones

¹¹ Analysis after Schlichting, 1979, p. 9.

are the Mach and Reynolds numbers. Note that the Reynolds Number and also the Knudsen number contain a characteristic length. The choice of characteristic length depends on the problem at hand; it may be distance along or perpendicular to the flow. This will be discussed further in Section 5.5.1.

Note that many aerodynamics calculations are done assuming $Le = Pr = Sc = 1$, which tends to simplify the equations to be solved.

Table 5.4. Common Aerodynamic Dimensionless Parameters

Mach Number	$M = u/a$	The physical meaning of M^2 is that it compares flow energy to internal energy, so that when $M \ll 1$ the thermophysics is not coupled to the flow
Reynolds Number	$Re_x = \rho u x / \mu = (\text{Inertial force, } \rho u \partial u / \partial x) + (\text{Frictional force, } \mu \partial^2 u / \partial y^2)$ where x = distance along the flow , y = distance perpendicular to flow (applies to boundary layer)	
Lewis Number	$Le_{ij} = D_{ij} \rho c_p / k$	Compares diffusive transport of energy with heat conduction
Prandtl Number	$Pr = \mu c_p / k$	Compares momentum and heat conduction transport
Schmidt Number	$Sc = \mu / \rho D$	Compares diffusive and momentum transport
Damkoehler No.(1)	$Dam_1 = x/u t_{chem}$ (t_{chem} = characteristic time for chemical reaction)	
Damkoehler No.(2)	$Dam_2 = q/c_p T_o$ (q = heat added/gm; T_o = characteristic temperature)	
Knudsen Number	$Kn = l_g k / d$	(d = characteristic distance for flow; $Kn > 1$ at very low densities/ high altitudes--implies failure of continuum concept)
Richardson Number	$Ri = - (g/r)(\partial r / \partial z) / (\partial u / \partial z)^2$ (g = gravitational acceleration, z = vertical distance). Ri is the ratio of an atmospheric buoyancy term that may promote either stability or instability, and a wind shear term that always tends to produce turbulence. Ri is important in atmospheric flows such as wind, cumulus convection, etc.	

5.6 BOUNDARY LAYER FLOW

Consider the flow of a fluid parallel to a flat plate. Normally there is no slip along the surface of the plate, i.e., the parallel velocity next the surface is zero, while of course far from the surface of the plate it has the ambient value $u(\infty)$. Thus, the velocity profile parallel to the surface has the general character shown in Fig. 5.5 .

The fact that u differs from $u(\infty)$ close to the wall cannot be explained by the Euler equations (which do not take into account molecular collisions of any kind, either gas-gas or gas-wall). However, the Navier-Stokes equations which contain a viscosity term to account for molecular collisions can explain how the fluid can support a shear stress and thus must be used within the boundary layer.

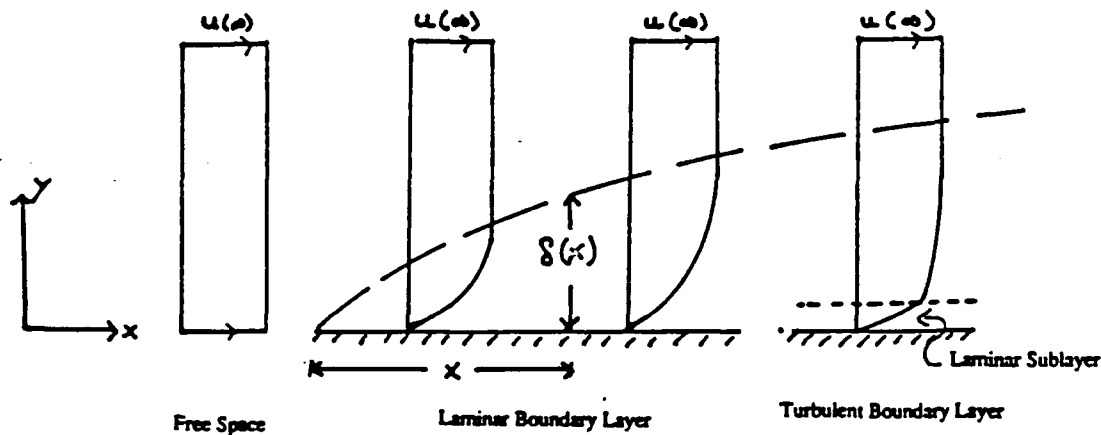


Figure 5.5. General Characteristics of Boundary Layers

The thickness $\delta = \delta(x)$ of the boundary layer as a function of distance x along the surface can be explained in terms of the rough equality of frictional and inertia forces--see the discussion of Reynolds number Re in Table 5.4--from which we write

$$\text{Inertia force, } \rho u \partial u / \partial x \sim \rho u^2 / x \quad (5.18a)$$

$$\text{Friction force, } \mu \partial^2 u / \partial y^2 \sim \mu u / \delta^2 \quad , \quad (5.18b)$$

and equating these terms gives

$$\delta = A \sqrt{(\mu x / \rho u)} \quad , \quad (5.19)$$

where A is a numerical coefficient whose value for a laminar boundary layer is approximately equal to 5 (cf. Schlichting, 1979, p. 76.)

When the Reynolds number becomes sufficiently large (see Section 5.7 below) the flow becomes turbulent, and then the flow velocity profile changes. A turbulent boundary layer has a laminar sublayer close to the wall and a smaller velocity gradient $\partial u / \partial y$ outside because the effective (eddy) viscosity is greater than the molecular viscosity so that the shear stress $\tau = \mu \partial u / \partial y$ remains roughly constant.

In physical terms we can understand the boundary layer as that region of the fluid in which collisions of molecules with the wall are important. Thus, the flow of a fluid past a solid surface is divided into two regions. Within the boundary layer we must consider collisions, but the mean flow speed tends to be relatively low so that the comparatively simple equations of incompressible flow may be adequate, while outside the boundary layer the flow speed is high so that compressibility effects are important, but the effects of collisions do not have to be considered explicitly. Thus the effects on the flow of ablation will only be important in the boundary layer and not in the high-speed flow outside. Some characteristics of ablation are discussed in the Section 5.8 below.

5.7 TRANSITION FROM LAMINAR TO TURBULENT FLOW

5.7.1 Introduction

The idealization of streamline or laminar flow is observed under rather specialized conditions, but once the characteristics of the flow itself become significant (in terms of lift, drag, heat transfer, etc.) the conditions are normally relatively severe--e.g., high fluid density, high speed, high shear, or whatever--so that the smooth, laminar flow generally

breaks up into turbulent, irregular flow with greater effective frictional drag and greater heat transfer than in the idealized case of laminar flow.

A turbulent flow is inherently irregular and unstable on a small scale, although it has some statistical regularities. Thus, the theory of turbulent flows is both more complicated and also less well developed than that of laminar flows. In a turbulent flow the energy dissipation rate is much larger than the molecular viscous dissipation rate. It is often convenient to introduce an effective or *eddy* viscosity coefficient which is much larger than the molecular viscosity μ which is introduced in Appendix E, Eq. (E.18). However, the eddy viscosity is not just a property of the medium but depends on the history of the "air parcel" under consideration. One cannot simply tabulate and look up an eddy viscosity in general, but has to investigate flows of the same medium under similar conditions.

To ask for the transition from laminar to turbulent flow one has to specify the conditions of the flow, and here I give three distinct and different examples. The numerical values come from Schlichting (1979), pp. 39, 41, 26, and 513. In particular, conditions in flows involving walls (see Sections 5.6.2, 5.6.3) where the Reynolds number is significant are quite different from free atmospheric flows (see 5.6.4) where the instability is induced by the interplay of buoyancy and wind shear, so that the Richardson's number

$$Ri = - (g/\rho) (\partial\rho/\partial z)/(\partial u/\partial z)^2_{\text{wall}} , \quad (5.20)$$

where the vertical coordinate z increases going upward, is the critical parameter.

5.7.2 "Poiseuille" Flow in a Tube

Consider the flow of fluid in a long narrow tube of diameter d . As the pressure head and hence the velocity u increases, the flow becomes turbulent when

$$Re_d = \rho u d/\mu > Re_{c1} \sim 2300-10,000 , \quad (5.21)$$

where the lower limit applies to a tube with a very rough walls which enhance the onset of turbulence, while the upper limit corresponds to exceedingly uniform conditions in the flow (smooth walls).

5.7.3 Boundary Layer Flow

Consider flow with velocity u along a flat plate. A *boundary layer* builds up, and at a distance x along the flow for which the Reynolds Number Re_x exceeds a critical value, Re_{c2}

$$Re_x = \rho u x / \mu > Re_{c2} \sim 3.2 \times 10^5 - 10^6 \quad (5.22a)$$

the flow becomes turbulent. Note, however, that this can be expressed differently. In terms of the boundary layer thickness $\delta = \delta(x)$ of Eq.(5.19), the flow becomes turbulent when

$$Re_\delta = \rho u \delta / \mu > Re_{c3} \sim Re_{c1} \sim 2300 - 10,000. \quad (5.22b)$$

5.7.4 Atmospheric Turbulence

In free atmospheric flows the physics is different, and also there is normally no well-defined distance such as d , x , or δ . Thus the Reynolds number is not a significant parameter. Here the flow becomes turbulent if the turbulent energy production due to wind shears is large compared with the buoyancy term. In this case, the criterion for turbulence is expressed in terms of the Richardson's Number Ri of Eq.(5.20), and the flow becomes turbulent if

$$Ri < Ri_c, \quad (5.23)$$

where $Ri_c \sim 0.042$.

5.8 SOME CHARACTERISTICS OF ABLATORS AND ABLATION

Ablation is a self-regulating mass transfer process which can be used to reduce the frictional heating of a vehicle during entry into the earth's atmosphere. The vehicle surface is coated with some material which decomposes by a variety of different physical and chemical processes, all of which involve taking up energy from the gas flow and thus reducing heat transfer into the reentry vehicle:

- (a) Melting and vaporization (two phase changes)--e.g., refractory oxides such as quartz or silica
- (b) Sublimation (phase change directly from solid to vapor)--e.g., Teflon
- (c) Chemical decomposition--here a variety of things can occur:
 - Depolymerization: complex (hydrocarbon) polymer breaks down into a monomer at high temperatures, and the monomers may react with oxygen in the boundary layer
 - Pyrolysis: thermal decomposition of molecules at high temperature. For organic compounds this leads to gases (hydrogen, methane, acetylene, etc.) and char (carbon) residue
 - Combustion: oxidation of material--e.g., graphite

- Charring ablators--such as carbon phenolic, quartz phenolic, silica phenolic and asbestos phenolic--are very commonly used.

The analysis of ablation is very complex and highly specific to the particular ablative material used. It is necessary to analyze the changes in both the entry vehicle and also in the boundary layer, considering chemical reactions to the extent necessary. For a historical perspective for the development of ablative reentry vehicles, see Sutton, 1982.

5.9 THE OPTICAL SIGNATURE OF A REENTRY VEHICLE

5.9.1 Introduction

For a variety of applications one needs to know the range of values of the optical (UV-LWIR) signatures of generic reentry vehicles (RVs). There exist many specific observations and calculations, which are coordinated through the USA/SDC-Teledyne Brown Optical Signatures Code (OSC), but before one goes to such an elaborate model it helps to have a simple understanding of the physical factors involved. The object of this discussion is to provide such an understanding.

Explicitly, as representative reentry vehicle we consider a round-nosed cone of 10-degree half-angle and length 1.7 m, which is described¹² in Appendix F. Viewed broadside-on, its area is

$$A_b \sim 1.9 \text{ m}^2 \quad (5.24)$$

The variability in actual RV signatures is due to the following factors:.

- | | |
|----------------------------------|---|
| (i) Size: | the RV used in our calculations is "average" |
| (ii) Shape and weight: | determines peak heating altitude |
| (iii) Ablative coating: | different coatings give different peak temperatures |
| (iv) Reentry angle and velocity: | determines peak heating altitude |
| (v) Solar illumination geometry: | this is very important between UV and MWIR, where solar illumination is critical |
| (vi) Cloud cover | determines the reflection of sunlight and also has an influence on earthshine emission. |

¹² This RV has the same ballistic coefficient β as the RV whose temperature profile is shown in Fig. 5.3.

As a result of factors (i)-(iv), the LWIR RV signature as computed here is likely to vary by a factor 2-3 at high and low altitudes, but by a factor 10 near peak heating where the factors (ii)-(iv) above will be more critical. However, in the shorter wavelength region, where solar illumination predominates (in the daytime), variations by factors of 100 or greater are possible. There may be effects of non-equilibrium chemistry, and significant contributions may come from the flow field of the reentry wake.

For definiteness, we present computations for three different wavelengths:

- $\lambda = 0.5 \mu\text{m}$, visible
- $\lambda = 3.5 \mu\text{m}$, Mid-IR (MWIR)
- $\lambda = 12 \mu\text{m}$, Long-Wave IR (LWIR).

These are all atmospheric transmission regions, so that atmospheric transmittance is generally close to one. Table 5.5 gives the numerical values used here for a variety of parameters at these different wavelengths. The parameters are defined later on in the text, as indicated.

In Section 5.9.2 we discuss the shape and heating of the RV; in Section 5.9.3 we compute the thermal emission signature which dominates in the longer-wavelength IR; Section 5.9.4 demonstrates how to calculate the solar scattering (which is important at the shorter wavelengths), Section 5.9.5 gives the earthshine-scattering contribution, and Section 5.9.6 calculates the signature due to sunlight scattered from clouds or the earth's surface. Section 5.9.7 combines all these results and Section 5.9.8 refers to the Optical Signatures Code (OSC) which is used for quantitative reentry vehicle signatures.

5.9.2 Typical Shape and Heating of a Generic Reentry Vehicle

Figure 5.3 provides the computed temperature profile for a particular reentry vehicle as a function of altitude at a specific range and reentry angle. In free space [altitudes $> 400,000$ ft (122 km)] the RV is at a uniform temperature of approximately 300 K. As it descends into the sensible atmosphere, a bow shock begins to develop so that first the nose heats up: thus at 300,000 ft (92 km) there is considerably less radiation than is observed at lower altitudes (but significantly more than in free space). For the particular case shown here the nose temperature has reached its peak value (due to stagnation point shock heating--cf. Section 5.4) by 250,000 ft (76 km). As the RV descends further, its skirt temperature increases as the boundary layer builds up. Note that the temperature profile at 90,000 ft (27 km) altitude shows an abrupt rise in temperature along the body. This

indicates the transition to turbulence (Section 5.7) in the particular computation scheme used by AVCO in deriving the results of Fig. 5.3.

For computational purposes, we break up the target (viewed broadside-on) into eight segments $j = 1, 2, 8$, each of fractional area α_j (i.e., $\sum_j \alpha_j = 1$). The details of the computation are given in Appendix F.

Table 5.5. Parameters Used Here

<ul style="list-style-type: none"> Transmittance: <ul style="list-style-type: none"> Because these are all transmission bands and most of the atmosphere is between the earth and the target, we shall take $\tau_S = 1$ and $\tau_E = 0.8$ at all wavelengths considered. 				
<ul style="list-style-type: none"> Emittance and Reflectance: 				
	λ (μm)	0.5	3.5	12
Target emittance ϵ		0.5	0.7	0.9
Target reflectance $\rho (= 1 - \epsilon)$		0.5	0.3	0.1
Earth emittance ϵ_E^*		0.3	0.9	0.9
<ul style="list-style-type: none"> Earth Surface Temperature: From LOWTRAN-5 Midlatitude Summer Atmosphere we take $T_E = 287$ K 				

* From McClatchey et al., 1972--see, e.g., Part I of these Notes, Fig. 3.3.

5.9.3 Thermal Emission Signature

If we divide the target into segments α_j , then for a reentry vehicle having an emissivity-area product ϵA , the temperature history of Fig. 5.3, the thermal emission in a spectral band k at height h is

$$L_{T,\Theta} \text{ (W/sr-}\mu\text{m)} = \epsilon A \sum_j \alpha_j B[\lambda_k; T_j(h)] \quad , \quad (5.25)$$

where $T_j(h)$ = temperature of segment j at height h (see Fig. 5.3)

λ_k = center wavelength of band k (μm)

$B(\lambda, T)$ = blackbody spectral radiance ($\text{W/m}^2\text{-sr-}\mu\text{m}$) for wavelength λ and temperature T .

The results for $L_{T,\theta}$ for all three wavelengths and four altitudes are shown in Appendix F; the results will be set in context and discussed in Section 5.9.7.

5.9.4 Diffuse Scattering of Sunlight

At the shorter wavelengths, a target is seen largely by reflected sunlight, and here the magnitude of the signature depends on the solar spectral irradiance $M_S(\lambda)$ and also--to a critical degree--on the character of the scattering.¹³ The reflectance of both sunlight and earthshine may generally be taken as diffuse Lambertian characterized by a bi-directional reflectance ρ ,¹⁴ so that L_{sca} , the radiance of the surface ($W/m^2\text{-sr-}\mu m$) is related to E_{inc} , the irradiance on the surface ($W/m^2\text{-}\mu m$) by the relation:

$$L_{sca} (W/m^2\text{-sr-}\mu m) = (\rho/\pi) E_{inc} (W/m^2\text{-}\mu m) \quad (5.26)$$

The computation of the signal due to sunlight scattered diffusely by the target is sketched in Fig. 5.6. Explicitly, the solar (spectral) irradiance M_S ($W/m^2\text{-}\mu m$) is attenuated by the transmission factor τ_S ,¹⁵ scattered diffusely (see Eq. 5.26) by the target of effective area A to give the signal

$$L_{T,S} (W/\text{sr-}\mu m) = A M_S \tau_S \cos\phi_1 (\rho/\pi) \cos\phi_2 \quad (5.27)$$

where the target is modeled as a flat plate with $A = A_b$ of Eq. (5.24) and the angles are defined in Fig. 5.6.¹⁶ This is then attenuated by the transmittance τ_{path} from target to sensor to give a target radiance $L_{T,S} \tau_{path}$.

Table 5.6 gives the solar scattering at $\lambda = 0.5$, 3.5 , and $12 \mu m$ for a specific set of numerical assumptions that are called out in the text and footnotes. Note that--unlike the thermal emission signal discussed in Section 5.9.3--the results are independent of altitude h or RV temperature.¹⁷

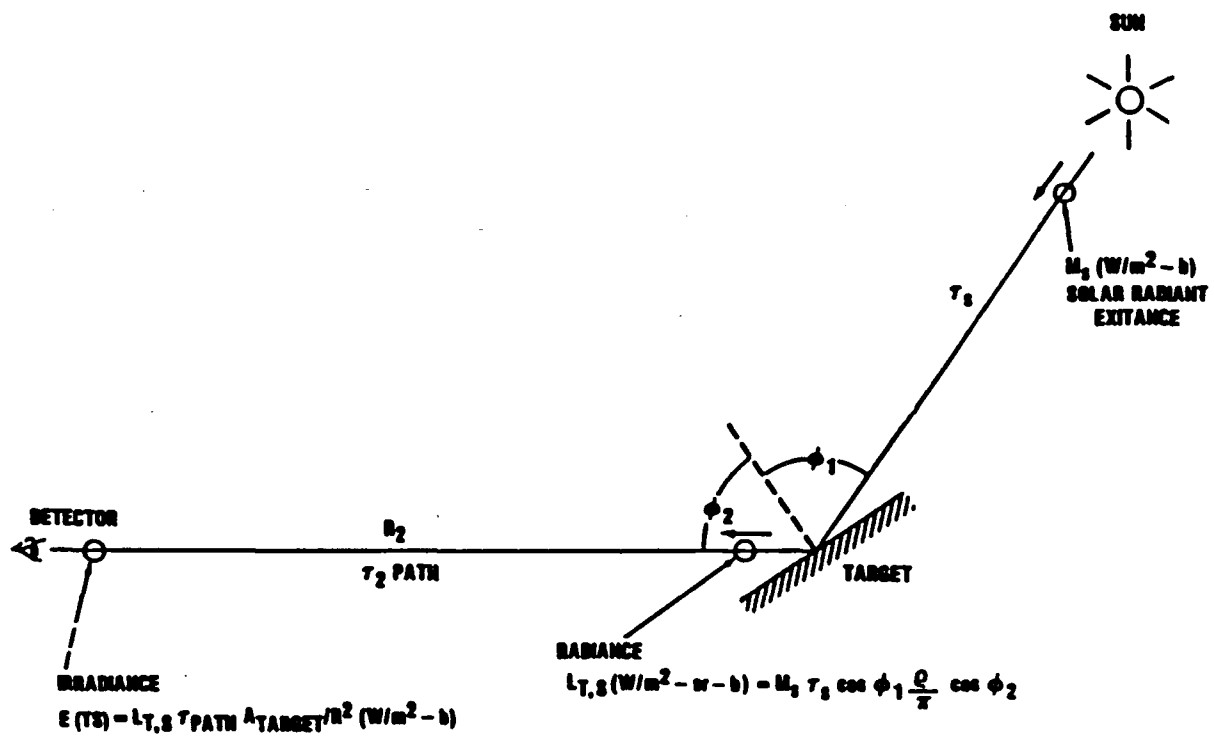
¹³ Note that there is a large contribution due to sunlight scattered from the earth or clouds--see Section 5.9.6.

¹⁴ $\rho = 1 - \epsilon$, where ϵ = emissivity of the surface. Numerical values used are listed in Table 5.4.

¹⁵ All transmittance factors are taken equal to one in the numerical examples because we are dealing with transmission windows in the atmosphere.

¹⁶ We use $\phi_1 = \phi_2 = 45^\circ$, i.e., $\cos \phi_1 \times \cos \phi_2 = 0.5$.

¹⁷ Except for possible differences in scattering geometry and atmospheric transmittance with altitude.



7-00-01-0

Figure 5.6. Computing the Target Irradiance Due to Solar Scattering

Table 5.6. Representative Numbers for Solar Scattering

λ (μm)	0.5	3.5	12
Solar irradiance $H_S(\lambda)$ ($\text{W}/\text{m}^2\text{-}\mu\text{m}$)	940	14.6	0.12
Bidirectional reflectance ρ	0.5	0.3	0.1
Scattered Signal, $L_{T,S}$ ($\text{W}/\text{sr}\text{-}\mu\text{m}$)	280	2.6	$7.1 \text{ E-}3$

5.9.5 Earthshine Scattering

The computation of the signal due to earthshine scattered diffusely by the target, $L_{T,E}$, is sketched in Fig. 5.7. This computation is somewhat more complex than that of $L_{T,S}$ because one has to integrate contributions from different portions of the earth's surface, in contrast to the sun which can be treated as a (distant) point source.

The signal from the target due to earthshine scattering, $L_{T,E}$, is obtained by starting with earth radiance $L_E = \epsilon_E B(T_E)$, tracking the irradiance of the target, and then going through the diffuse scattering process of Eq. (5.26). Figure 5.7 sketches the procedure. Given L_E , one attenuates by the atmospheric transmittance factor to the target

$$\tau_E(\phi_a) = \tau_E^{\sec\phi_a} , \quad (5.28)$$

multiplies by the solid angle factor $dA_E/[R_E(\phi_a)]^2$ reduced by the projection $\cos\phi_1$, and then integrates over the whole accessible surface of the earth. This somewhat intricate procedure is discussed in detail in Appendix G. Next we have diffuse (Lambertian) scattering as in Eqs. (5.26) and (5.27), which gives the following expression for the earthshine-scattered signal of the target as seen by the sensor, $L_{T,E}$,

$$L_{T,E} = A_b \int dA_E L_E \cos\phi_1 [R_E(\phi_a)]^{-2} \tau_E(\phi_a) (\rho/\pi) \cos\phi_2 \quad (5.29)$$

$$= A_b 2 \epsilon_E(\lambda) B(\lambda, T_E) \rho \cos\phi_2 I_T(\tau_E, \beta) \quad (5.30)$$

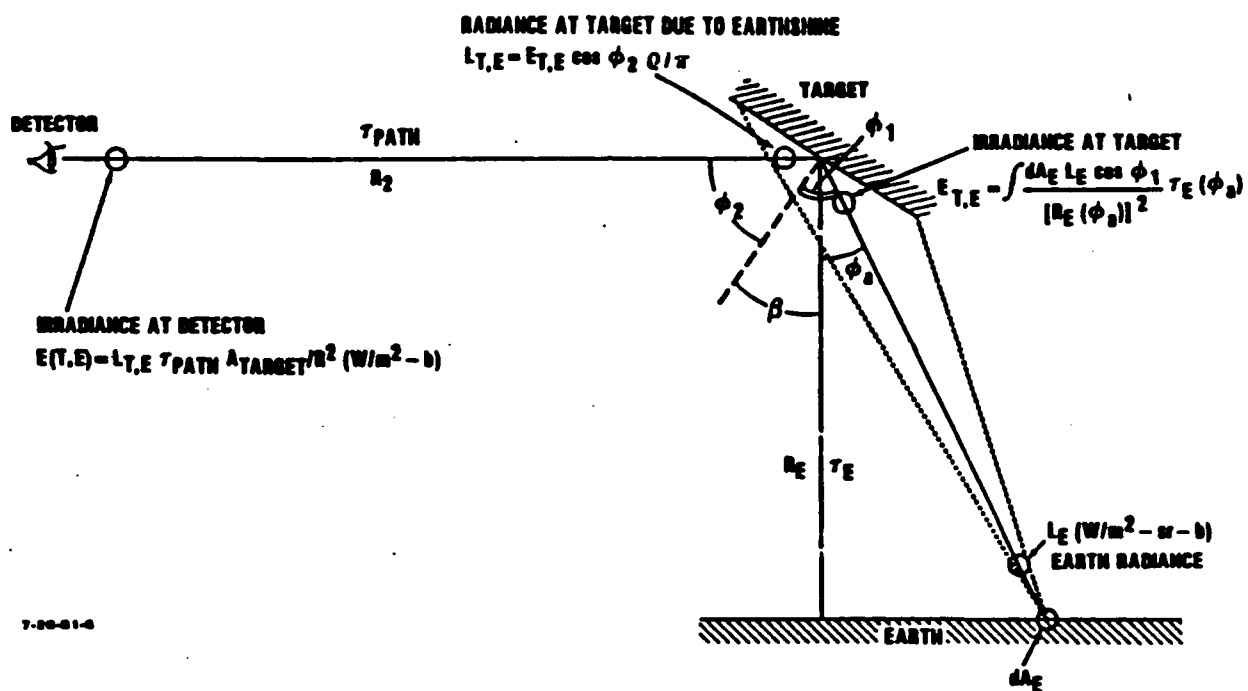


Figure 5.7. Computing the Target Irradiance due to Earthshine Scattering

where the integral $I_T(\tau_E, \beta)$ is discussed in Appendix G, and the angle of attack, β , as well as the angles ϕ_1 and ϕ_2 are defined in Fig. 5.7.¹⁸ Numbers analogous to Table 5.6 are listed in Table 5.7. Numerical values for the various parameters used are listed in Table 5.5.

Table 5.7. Earthshine Scattered Target Signal

	λ (μm)	0.5	3.5 12
ϵ_E	0.3	0.9	0.9
Earth Radiance Term, $B(\lambda, T_E)$ ($\text{W}/\text{m}^2\text{-sr-}\mu\text{m}$)	1.1 E-34	0.14	7.5
Earthshine radiance, $L_{T,E}$ ($\text{W}/\text{sr-}\mu\text{m}$)	3.0 E-36	7.0 E-3	0.12
* Note that $\tau_E = 0.8$, i.e., $b = \ln(1/\tau_E) = 0.22$, and thus $I_T(b) = 7 \times 10^{-2}$ from Fig. G.2 of Appendix G.			

5.9.6 Signal due to Sunlight Scattered from the Earth or Clouds¹⁹

At the shorter wavelengths, an important contribution to the target signature comes from sunlight that is scattered from the earth or from cloud tops and is then reflected diffusely from the target. Reference to Fig. 3-3 of Part I shows that the reflectance of various natural surfaces in the visible and near-IR, ρ_{nat} , is variable but quite significant. Thus the solar irradiance M_S ($\text{W}/\text{m}^2\text{-}\mu\text{m}$) is attenuated by a transmission factor τ'_S and the signal reflected from the earth or from cloud tops is $M_S \tau'_S (\rho_{\text{nat}}/\pi)$, so that from an analysis similar to that for earthshine scattering in Section 5.9.5, [see Eq.(5.30)], one finds that

$$L_{T,SS} = A_b M_S \tau'_S (\rho_{\text{nat}}/\pi) \rho \cos\phi_2 I_T(b) \quad . \quad (5.31)$$

Table 5.8 gives values of M_S , ρ_{nat} , ρ , and $L_{T,SS}$ for $\lambda = 0.5$, 3.5 and 12 μm ; in the calculation we have used the same numerical values for the various parameters as in Sections 5.9.4 and 5.9.5, namely $\cos \phi_2 = 0.707$, $\tau'_S = \tau_E = 0.8$, $I_T(b) = 7 \times 10^{-2}$.

¹⁸ We use $\beta = \phi_1 = \phi_2 = 45$ deg.

¹⁹ I wish to thank Dr. Rich Loda for pointing out the importance of this term.

Table 5.8 Signal due to Sunlight Scattered from the Earth or Clouds

λ (μm)	0.5	3.5	12
Solar Irradiance $H_S(\lambda)$ ($\text{W/m}^2\text{-}\mu\text{m}$)	940	14.6	0.12
Earth (or cloud) reflectance, ρ_{nat}	0.5	0.2	0.1
Target bidirectional reflectance, ρ	0.5	0.3	0.1
Radiance due to scattered sunlight, $L_{T,SS}$ ($\text{W/sr-}\mu\text{m}$)	240	2.1E-2	2.8E-5

5.9.7 Total Signature of a Reentry Vehicle

With the exception of specular reflection or glints,²⁰ the signature of a reentry vehicle is the sum of contributions due to solar scattering, $L_{T,S}$, thermal emission $L_{T,\Theta}$, and earthshine scattering $L_{T,E}$ (which turns out to be small). Combining the results of Tables 5.6 through 5.8, we show the results in Table 5.9, which are quoted in units of $\text{W/sr-}\mu\text{m}$:

- (a) In Table 5.9 the only figures which vary with altitude (i.e., temperature--see Fig. 5.3) are those for the thermal emission, $L_{T,\Theta}$, which are largest at peak heating near 75,000 ft (23 km) altitude.
- (b) $L_{T,\Theta}$ varies strongly with temperature: note that the visible and MWIR radiance is very large because at a peak temperature near 2600 K the RV glows brightly.
- (c) In fact, $L_{T,\Theta}$ is much larger than the solar scattering contribution, $L_{T,S}$, in the visible near peak heating.
- (d) Recall that non-equilibrium considerations and wake contributions are not included here.

5.9.8 Introduction to the Optical Signatures Code (OSC)

The OSC is a computer program--now (1989) in its 15th version--which has been developed during the last 15 years. Its objective is to develop IR optical signatures of reentry vehicles, PenAids, chaff, etc., in Midcourse and Reentry phases, in a computerized

²⁰ The signal due to glint is $L_{T,S*} = A_b r M_S \tau_S \cos\phi_1 \times \cos\phi_2$ instead of Eq. (5.27), where r = specular reflectivity, which may be close to one. Reference to Table 5.6 shows that this can be significantly larger than $L_{T,S}$. However, the actual reflected power has to be multiplied by the fraction of the total area that gives such specular reflection, which is normally very much smaller than one. Accordingly, this contribution to the signal is not considered here.

Table 5.9. Total Signature of Reentry Vehicle

	λ (μm)	0.5	3.5	12
<u>$h = 300$ kft (91 km).</u>				
Solar scattering,	$L_{T,S}$	280	2.6	7 E-3
Thermal emission,	$L_{T,\theta}$	2 E-8	38	45
Earthshine scattering,	$L_{T,E}$	3 E-36	7 E-3	0.1
Solar-Earth/Cloud Scatt.	$L_{T,SS}$	240	1E-2	2.8E-5
Total signal	L_{tot}	520	41	45
<u>$h = 150$ kft (46 km)</u>				
	$L_{T,S}$	280	2.6	7 E-3
	$L_{T,\theta}$	840	6500	340
	$L_{T,E}$	< ——— small ——— >		
	$L_{T,SS}$	240	small	small
	L_{tot}	1300	6500	340
<u>$h = 75$ kft (23 km) Peak Heating.</u>				
	$L_{T,S}$	280	2.6	7 E-3
	$L_{T,\theta}$	53,000	76,000	1400
	$L_{T,E}$	< ——— small ——— >		
	$L_{T,SS}$	240	small	small
	L_{tot}	29,000	41,000	730
<u>$h = 25$ kft (7.6 km)</u>				
	$L_{T,S}$	280	2.6	7 E-3
	$L_{T,\theta}$	5 E-9	840	180
	$L_{T,E}$	< ——— small ——— >		
	$L_{T,SS}$	240	small	small
	L_{tot}	520	840	180

form which is accessible to the user. Because of long-term continuity by the developer (Teledyne Brown Engineering, Huntsville, AL 35807, Tel. 205-726-xxxx), there is a lot of collective memory (by John Davis x 1125, S. Murty x 1109, et al.); but because of the computer format it is frequently easier to get numbers than human judgment. In the production of the code much laboratory and field data have been absorbed and analyzed. There is in addition a great deal of information on material properties (optical, thermal, etc.), on reentry flow fields, heat transfer, ablation, and on optical signatures. Murty (1987) has presented some very nice lecture notes on endoatmospheric²¹ heating theory.

Information about the code may be obtained²² from Ellen Montenegro, TBE-1413, or from Tom Prestwood, USASDC, Passive Sensor Division, DASD-H-YP, Huntsville, AL 35807, Tel. 205-895-4572. While the code is largely Unclassified, the validation data make the whole thing Secret. The code as a whole consists of a number of different codes.²³ To get results that can be trusted, significant effort on the user's part is required.

²¹ "Endoatmospheric" means within the atmosphere, i.e., at altitudes below 60-100 km, as contrasted with "exoatmospheric," or above the sensible atmosphere.

²² These names and phone numbers are correct as of October 1989.

²³ Many of the individual codes were developed by various reentry contractors during the 1960s, so that there are probably deficiencies in corporate memory.

6.0 PRIMER ON NUCLEAR WEAPONS EFFECTS

6.1 INTRODUCTION

When a nuclear weapon is detonated, a very large amount of energy is produced, either by the fission of uranium or plutonium or by fusion reactions involving D, T, or ${}^6\text{Li}$. All these reactions produce neutrons and sustain chain reactions; fission produces on the order of 200 MeV per atom while a fusion reaction produces 3-17 MeV, and the yield-to-mass ratio obtained by either mechanism is the same within a factor 3 or so. One kiloton (kt) of energy²⁴ is 10^{12} calories or 4.2×10^{12} Joules, and corresponds to the complete fission of 0.057 kg of uranium. The detonation is by no means 100 percent efficient; a representative mass of a nuclear weapon is of the order of 10^2 - 10^3 kg. Thus we see that most of this material remains as *Bomb Debris*. This material is heated to a very high temperature during the detonation, being largely vaporized and ionized. A significant fraction of the energy of the detonation appears as debris kinetic energy. The debris expansion velocity u is (see, e.g., Holland, 1977, p. 162.)

$$u \sim (Y/M)^{1/2} \sim 10^7\text{-}10^8 \text{ cm/sec} , \quad (6.1)$$

where Y (Megatons, Mt) is the total yield of the weapon and M is the total mass participating in the expansion.

Most of this energy is emitted in a time of the order of 0.1-1 μsec . In this time the bomb radiates essentially all of its energy as a blackbody of 1-10 keV blackbody temperature, which corresponds to EM radiation of wavelength 12-1.2 Å, i.e., soft X-rays. The total energy output of a nuclear weapon is distributed roughly as is shown in Table 6.1.²⁵ Note that the largest part of the energy output is in the form of (3-30 KeV) X-rays, while debris kinetic energy provides most of the rest.²⁶

²⁴ Which corresponds roughly to the heat of combustion of 1000 tons of TNT.

²⁵ See, e.g., Holland, 1977, p. 162 (but more X-ray yield than listed there), also ENW, 1964 or 1977, Ch.1-2.

²⁶ For orientation on mass-yield relations, note that (a) If $Y = 20 \text{ kT} = 8 \times 10^{13} \text{ J}$, a velocity of 10^7 - 10^8 cm/sec means that a mass of order 100-1000 kg is involved; (b) The U.S. 8-in. (203-mm) Howitzer M115 fires projectiles in the 90-95 kg range. One of these is the nuclear M422 round whose yield is in the 5-10 kt range [Jane's *Armour and Artillery* (1986-87) p. 673.]

Table 6.1 Typical Energy Distribution from a Nuclear Explosion in Vacuum

X-ray yield	70%
Debris kinetic energy	25%
Delayed nuclear radiation	5%
Prompt neutrons	0.1-1%
Prompt gamma rays	0.01-0.1%

It is clear that only a small fraction of the mass of the device undergoes fission, and only a small fraction of the yield comes out as nuclear radiation.²⁷ The nuclear radiation is frequently not considered in the analysis of vulnerability, and in most discussions of phenomenology it does not matter whether the weapon is a fission or fusion device, since most of the energy comes out as X-rays and debris kinetic energy.

If the energy is assumed to be distributed isotropically, then the X-ray flux $W(R)$ due to a warhead of yield $Y(\text{Mt})$ at range R (km) is²⁸

$$W(R) = 6400 (Y/R^2) \text{ cal/cm}^2, \quad (6.2)$$

and this is the principal kill mechanism in the high-altitude range. Thus, for a vehicle hardened to 1 cal/cm^2 , the kill radius for a 1 Mt bomb is 270 km.

A typical total exposure due to a nuclear weapon detonated in vacuum is listed in Table 6.2. The shielding listed for the γ -ray dose is not large, but is representative for a space-based sensor.

Within the atmosphere, the bomb-generated X-rays are absorbed rather rapidly. Table 6.3 indicates the atmospheric extinction of different bomb radiations in the atmosphere. We see that the (soft) X-rays are absorbed below ~ 70 km, while neutrons and gamma rays are transmitted down to ~ 20 km. Note:

²⁷ Electrons and protons and other positive ions interact so strongly with ambient atoms and molecules that they do not travel far enough to be significant, but the uncharged neutrons and gamma rays interact sufficiently weakly with the ambient environment that they travel a long way and thus can be significant from the standpoint of their effect on biological organisms and on electronic solid state devices, which are very sensitive to ionizing radiation.

²⁸ This is the standard equation, which assumes that 80% of the bomb's yield goes into X-rays distributed isotropically. (The figure of 80% is conventional here, as compared with 70% or other values in Table 6.1.)

- (a) The absorption and extinction (= absorption + scattering) coefficient of X-rays in air as a function of energy is given in Fig. 4-3 of Part I of these notes (Bauer, 1990). Note that the extinction coefficient falls off very rapidly with increasing energy, and scattering is only important at the highest energies .
- (b) Typically, the X-ray spectrum of a nuclear weapon corresponds to a blackbody (Planck) distribution of approximately 1 keV temperature. The Planck spectrum is of the form ²⁹

$$F(u) = 15 \pi^{-4} u^3 / (e^u - 1) , \quad (6.3)$$

where $u = E/kT$; note that $F(u)$ has a maximum at $u = 2.8$.

Table 6.2. Total Exposure In Vacuum from a Nuclear Weapon of Yield $Y(\text{Mt})$ at a Range $R(\text{km})$ *

X-ray flux	$6400 (Y/R^2)$	cal/cm^2
γ -ray dose	$2.1 (Y/R^2)$	$\text{Mrad}(\text{Si})$ behind 23 mil Ta and $2 \text{ g/cm}^2 \text{ Al}^{**}$
γ -ray dose rate	$1.9 \times 10^{13} (Y/R^2)$	$\text{rad}(\text{Si})/\text{sec}$
Neutron flux	$1.6 \times 10^{15} (Y/R^2)$	cm^{-2}

- * Numbers kindly provided by William Chadsey and Rich Sutton of SAIC.
- ** 1 $\text{rad}(\text{Si})$ corresponds to the absorption of 100 erg/gm in Si. If we assume that all the γ -rays of effective energy 1 $\text{MeV} = 1.6 \times 10^{-6} \text{ ergs}$ are absorbed in 1 g/cm^2 , then 1 Mrad corresponds to a γ -ray flux of $10^8 / 1.6 \times 10^{-6} \text{ cm}^{-2} = 6.25 \times 10^{13} \text{ cm}^{-2}$. 23 mil Ta and $2 \text{ g/cm}^2 \text{ Al}$ is a minimum level of shielding normally used in spacecraft.

We see from Table 6.3 that at altitudes below 50 km the X-ray energy (which represents most of the bomb output) is absorbed near the burst, giving rise to a well-confined fireball³⁰ whose mass is actually of order of 10^6 tons/Mt yield. Table 6.4 indicates schematically how the fireball is created and enumerates the damage mechanisms within the atmosphere, which are sketched out in Section 6.2.4, following a discussion in Section 6.2.3 of near-surface bursts.

²⁹ See, e.g., Eq. (3.1), also Figs. 3.1 and 3.2, all in Section 3 of Part I of these Notes (Bauer, 1989).

³⁰ In fact, the debris is also stopped near the burst point in the lower atmosphere; at high altitudes the (largely ionized) debris follows the geomagnetic field lines.

Table 6.3. Atmospheric Transmission for a Horizontal Path Thickness of 10-km Length for 3 keV X-rays, 1 MeV Neutrons, and 1 MeV Gamma Rays at Different Altitudes.

Altitude (km)	Dens.(kg/m ³) for:	Transmission through 10 km horizontal path		
		3 keV X-rays	1 MeV neutrons	1 MeV gamma rays
	(Ext. coefft.):	(170 cm ² /g)	(1.7 × 10 ⁻²⁴ cm ² /atom)	(0.1 cm ² /g)
0	1.23	0	0	0
10	0.41	0	2 × 10 ⁻¹⁸	4 × 10 ⁻¹¹
20	0.089	0	1 × 10 ⁻⁴	5.5 × 10 ⁻³
30		0	0.17	0.72
40	0.0040	0	0.67	0.79
50		0	0.90	0.94
60		1 × 10 ⁻²³	0.97	0.98
70	8.8 × 10 ⁻⁵	3 × 10 ⁻⁷	0.99	1.00
80		0.03	1.00	1.00
90		0.58	1.00	1.00
100	5.0 × 10 ⁻⁷	0.92	1.00	1.00

Table 6.4. Effects of a Nuclear Weapon Exploded In the Lower Atmosphere

X-rays absorbed in Atmosphere	Shock/Blast wave →	Damage
Fireball		
Debris slowed down in Atmosphere	Thermal Radiation →	Damage
Nuclear Radiation (neutrons and γ-rays*)	—————→	Damage (Secondary)

* Only weakly absorbed in atmosphere - see Table 6.3.

At altitudes above 75-100 km the ambient density is so low that thermal X-rays are no longer absorbed within the atmosphere, and so the effects of a nuclear explosion are qualitatively different than at lower altitudes. Table 6.5 sketches the phenomenology and damage mechanisms in this altitude regime.

Table 6.5. Effects of a Nuclear Weapon Exploded In the Upper Atmosphere

X-rays*	• Emitted upwards, propagate freely	→	Damage (Primary Kill)
	• Emitted downwards, absorbed to heat air		
	Heated Air**	• Ionized	→ Radio Blackout
		• Radiates	→ Redout
Debris***	Transfers energy to heat air		
Nuclear Radiation	(propagates freely)	→	Damage (Secondary)

* Distributed roughly isotropically.

** May be moved upwards by Heave (see Section 6.3.3)

*** Travels along (possibly perturbed) geomagnetic field lines.

Overall high-altitude phenomenology is discussed in Section 6.3. Section 6.3.1 describes single-burst phenomenology at high altitudes; unlike the limited extent of nuclear fireballs within the atmosphere, the very tenuous upper atmosphere is disturbed out to distances of hundreds of kilometers, and thus not only the long-range effects of individual bursts but also the interaction between multiple bursts become very important. Multiburst phenomenology is discussed in Section 6.3.2 and a particular phenomenon called *Heave*, which involves the rise of relatively large masses of air heated by the absorption of X-rays and UV radiation, is treated in Section 6.3.3.

At high altitudes there is a highly ionized region of large extent which interferes with radio wave propagation; this "blackout" is discussed in Section 6.4.2; there is also a large region of heated air which radiates (mainly in the infrared) to produce an enhanced IR background, the so-called "redout" which is discussed in Section 6.4.3.

It must be stressed that the high-altitude multi-burst phenomenology is based on models which are not based on actual nuclear test observations. Section 6.5 discusses overall uncertainties in nuclear effects predictions.

6.2 NUCLEAR EXPLOSIONS IN THE LOWER ATMOSPHERE

6.2.1 Introduction

The previous discussion--see in particular Tables 6.3 and 6.4--points out that a fireball is produced at sufficiently high ambient densities or sufficiently low altitudes. The phenomenology of fireball formation and evolution in the atmosphere is described qualitatively in Section 6.2.2, which sketches the evolution and cooling of the fireball as it goes from the initial X-ray temperature of 1-10 keV (10^7 - 10^8 K) to ~ 1 eV (12,000 K) within some 10 sec for a Mt-range weapon (for more detail, see Brode, 1968). Section 6.2.3 gives a simple numerical model of the evolution of the fireball and its blast and thermal damage mechanisms. Two special issues for a near-surface burst--crater formation and atmospheric dust loading--are discussed briefly in Section 6.2.4. Some numbers for damage mechanisms due to a low air burst are sketched in Section 6.2.5 and Electro-magnetic Pulse (EMP) effects are outlined in Section 6.2.6.

Let us begin with some numbers for orientation. As a measure of the size of a nuclear fireball, its effective radius at thermal minimum³¹ for a near-surface burst of yield Y (Mt) is

$$R_{\text{eff}} \sim R_a Y^{0.4} \quad , \quad (6.5)$$

where $R_a \sim 430$ m, i.e., $R_{\text{eff}} \sim 90$ m for a 20 kt weapon or 430 m for a 1 Mt weapon (see ENW, 1977, p. 70).

Figure 6.1 shows how a low-altitude fireball expands with increasing time, and Fig. 6.2 shows the stabilized cloud rise height of the nuclear cloud as a function of weapon yield at mid-latitudes. To get a feel for the order of magnitude of the energy of a nuclear detonation, note that a 20-100 kt weapon rises to the mid-latitude tropopause (~ 11 km). This can be understood, since reasonably large thunderstorms--which have a comparable energy content--rise to this same height.³²

³¹ This will be defined in Section 6.2.2.

³² The energy that drives a thunderstorm is the latent heat of vaporization of the atmospheric moisture, which is in the range 600-700 cal/g which is $(2.5-3) \times 10^6$ J/kg or 0.6-0.7 kt(energy)/kt(mass). The water vapor density in a cloud is 1-10 g H₂O/m³ or 10^3 - 10^4 tons H₂O per km³, so that the latent heat of a thunderstorm of volume 1 km³ is ~ 0.6 -7 kt of energy.

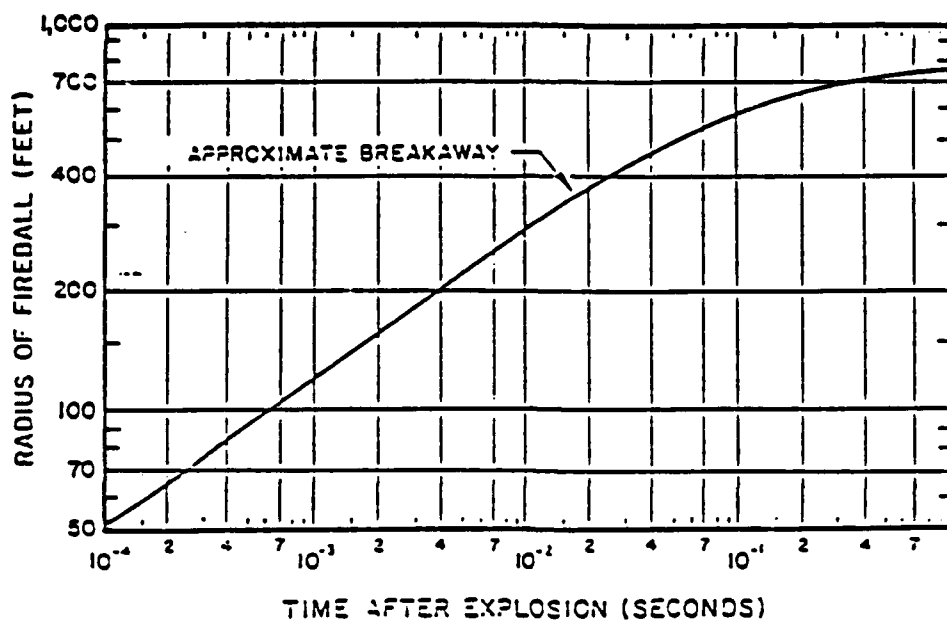
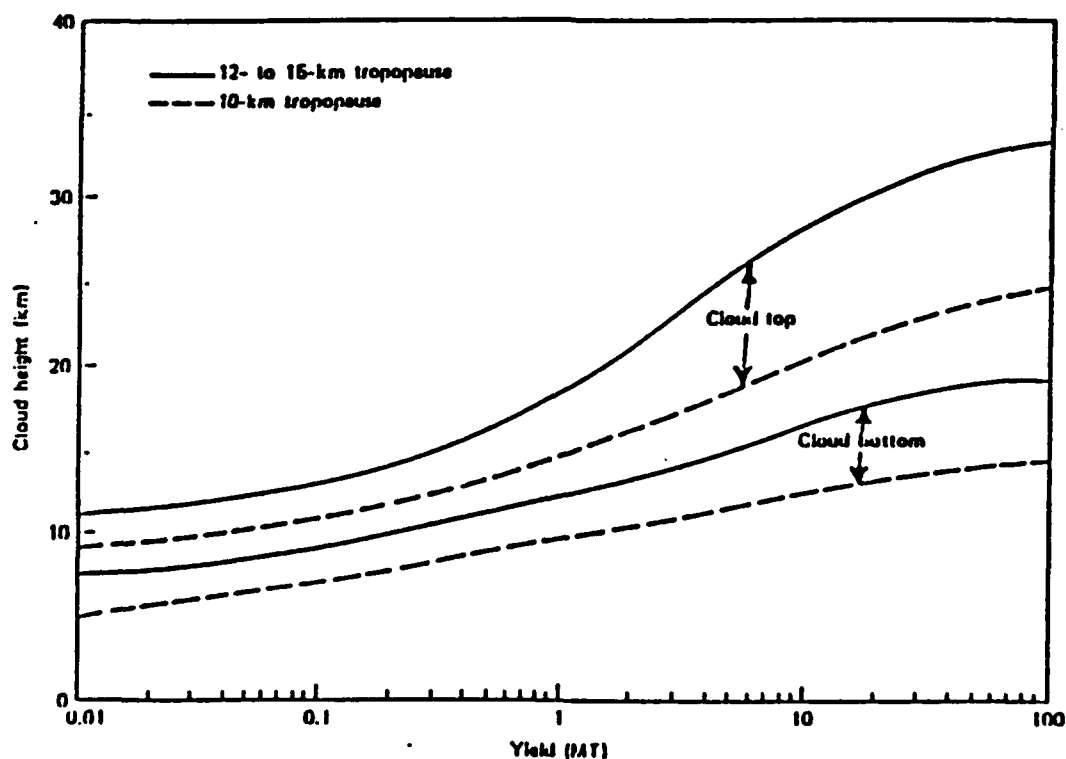


Figure 6.1. Fireball Expansion (ENW, p. 74) "Breakaway" corresponds to the situation when the hot, incandescent interior of the fireball can be seen through the air shock, which cools and becomes less opaque as it expands - see discussion in Section 6.2.2.



10-17-80-10 (P-1551, p. 6.2)

Figure 6.2. Nuclear Cloud Rise Height as Function of Yield.
[Synthesized by H. Mitchell (Falcon Research) from various sources, see, e.g., Bauer (1979)]

6.2.2 Qualitative Description of a Low Air Burst [quoted from J. Zinn (LANL--see Barasch, 1979)].

Within the first microsecond after detonation, the entire nuclear yield is deposited in the bomb materials, heating them to extremely high temperatures in the range 10^7 K. Some of this energy is immediately radiated away in the form of X-rays and extreme ultraviolet radiation, but this radiation is immediately reabsorbed in the air within the first few meters surrounding the device. The air is thereby heated to a very high temperature, in the range of 10^6 K, with a corresponding increase in pressure to several thousand atmospheres. This heated air and the hot bomb vapors (debris) in the interior constitute the initial fireball. The fireball subsequently expands through a combination of radiative and hydrodynamic processes. An intense shock wave (thin region of highly compressed air) is formed at the surface, which expands outward at a high velocity. Inside the shock, the energy is rapidly redistributed through emission and reabsorption of ultraviolet radiation.

Fig. 6.3 shows the thermal power radiated from a nuclear burst at different altitudes as a function of time. At the low altitudes under discussion here, the power is emitted in two pulses.

The time variation of light emission during the first pulse of Fig. 6.3 is controlled by the radial growth of the shock. Although the shock surface is intensely luminous, the shock is opaque to visible light, thus concealing the air and bomb debris in its interior. As the shock expands, it engulfs cold air, causing its temperature to decrease, with a corresponding decrease in brightness. The optical energy emission rate (power) is proportional to the fireball brightness times the area of its surface. After detonation, the optical power first increases, because the increase in surface area outweighs the decrease in brightness. Later it decreases, because the decrease in brightness is dominant.

During the early expansion and cooling of the fireball, the ultraviolet radiation in the interior decreases rapidly until it cannot effectively redistribute the energy. Thereafter the shock temperature falls more rapidly than the temperature in the interior. As the expansion proceeds, the shock continues to cool, and as it does so, it becomes less and less opaque to visible light, while also becoming less luminous. A point is reached, corresponding to the minimum temperature region in Fig. 6.3, where the shock becomes sufficiently transparent to allow light from the hotter interior to begin to escape, causing the optical output to begin increasing again³³. Further growth of the shock results in increasing transparency and a further increase of the luminosity of the inner region.

As the expansion continues further, the temperature of the inner fireball decreases, due to the combined effects of hydrodynamic expansion and loss of energy by radiation. This cooling eventually results in the decrease in luminosity following the second maximum in Fig. 6.3. After the second

³³ This is denoted by "breakaway" in Fig. 6.1.

maximum, the inner fireball gradually becomes transparent, revealing the bomb debris inside, whose brightness also decreases with time.

The majority of the total energy radiated by the fireball comes from the second peak, which is not very different in its instantaneous brightness relative to the first peak, but last about 100 times longer. By the time this "thermal pulse" is over, the available energy has either been radiated away, trapped in the debris and entrained air of the fireball, or it is propagating in the shock wave, which is now well outside the visible fireball.

Note that with increasing height of burst, the minimum in radiated power shown in Fig. 6.3 declines, disappearing above 40 km.

Figure 6.4 gives an alternative representation of what is shown in Fig. 6.3 by listing the evolution with time of the fireball temperature from a 20 kt burst.³⁴ We note that the fireball remains in the 1000-10,000 K temperature range for times of 3-30 sec, i.e., long enough so that its phenomenology has considerable implications to, for example, strategic defense systems. For a discussion, see ENW, 1964, Ch. 1 and 2, in particular pp. 87-100.³⁵

³⁴ Comparable results are obtained for other yields. Minimum and maximum temperatures are essentially independent of yield, but the time at which these temperatures occur scale approximately with the 0.4th power of yield--see ENW, 1977, p. 70.

³⁵ See also Zeldovich and Raizer, 1966, Vol. II, p. 611f, for a description taken from the first (1957) edition of ENW, which Zeldovich and Raizer describe as better than that in the 1962/64 edition. Note that there now exists a 3rd (1977) edition of ENW. This is poorer still from the standpoint of describing what actually was observed during a nuclear explosion, because by 1977 the observations of atmospheric nuclear tests of 1962 and earlier had been massaged to provide a homogenized but not necessarily more accurate description of what goes on.

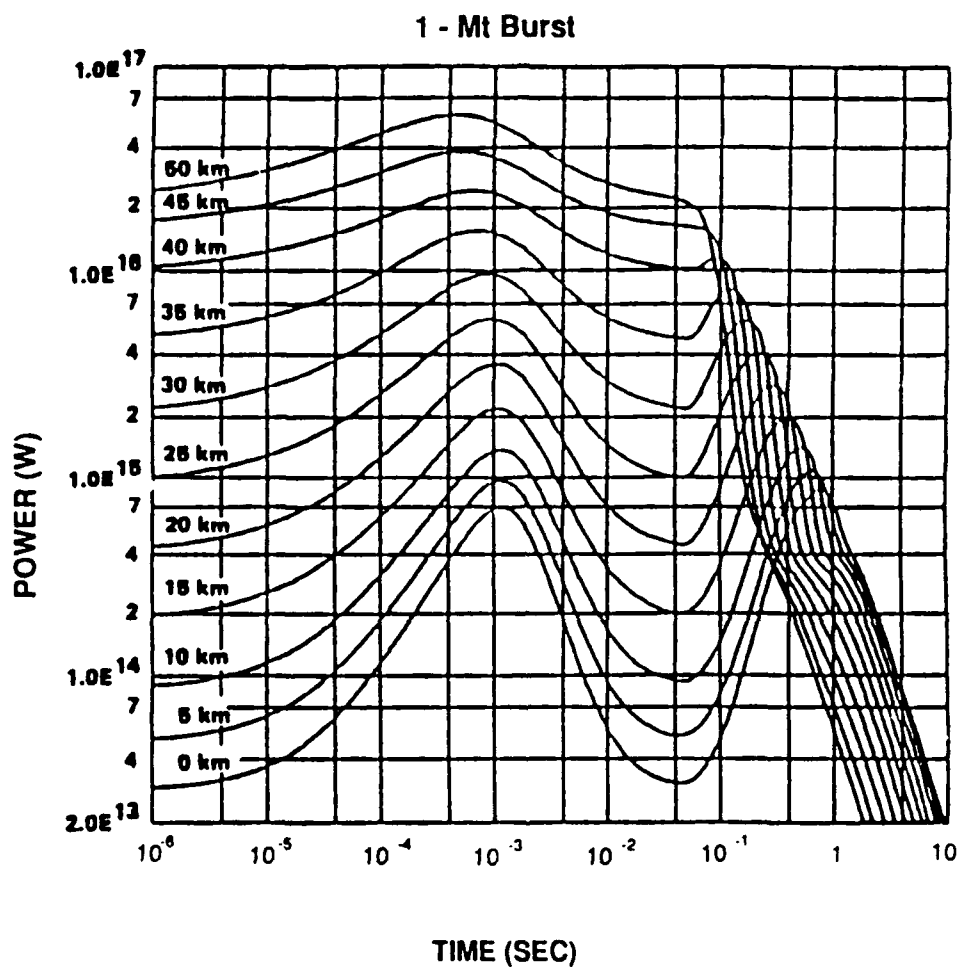


Figure 6.3. Thermal Power Emitted from an Air Burst as a Function of Time and Height of Burst (Obtained from N.R.Byrn, Nichols Research Corp.)

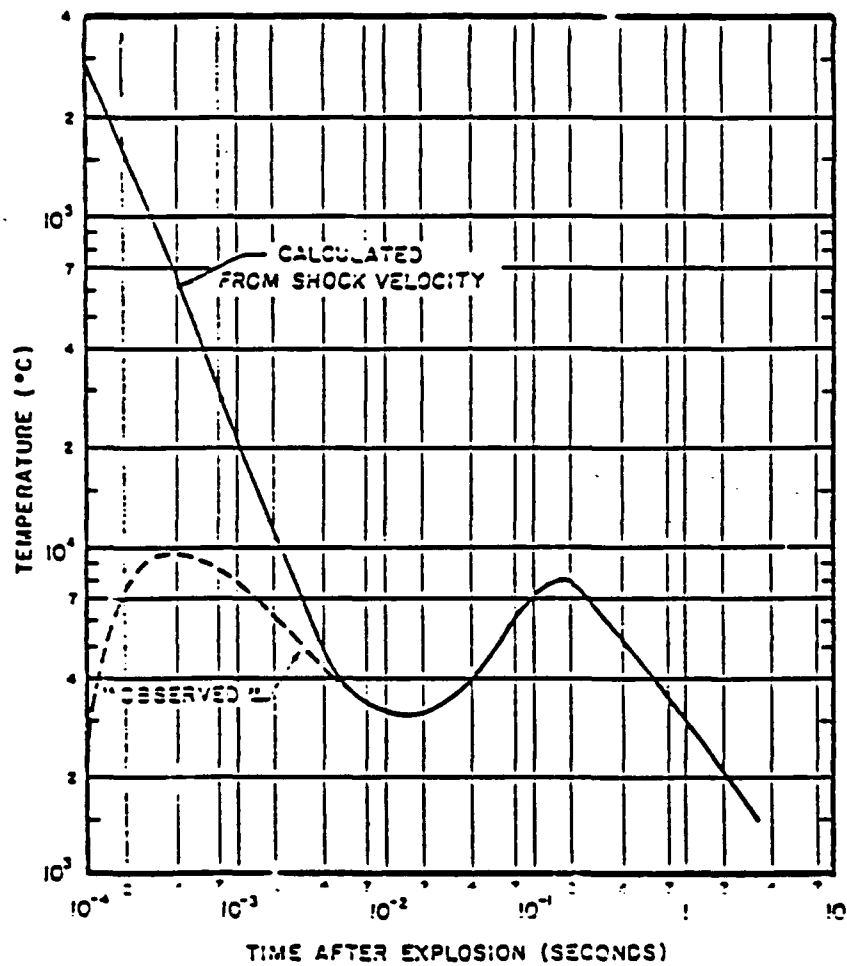


Figure 6.4. Variation of Apparent Fireball Surface Temperature with Time in a 20-kt Explosion. (Source: ENW, 1964, p. 75)

6.2.3 A Simple Model of Low-Altitude Fireballs (Source: Ewing & Barrett, 1989)

6.2.3.1 Fireball Size and Motion

This discussion assumes spherical fireballs (i.e., ignores the development of a toroid), applies for air bursts³⁶ below 50 km burst height and to times up to 60 seconds after burst.

A simple estimate for the radius is

$$R(t) = 0.85 Y^{0.33} (\rho_o/\rho)^{0.3} + 0.037 Y^{0.3} (\rho_o/\rho)^{0.2} (t-t^*) \text{ (km)} \quad (6.6)$$

where $Y =$ total weapon yield (Mt)

$\rho_o =$ air density at sea level

$\rho =$ air density at burst altitude

$t =$ time after burst (sec)

$$t_{pe} = (Y \rho_o/\rho)^{1/3} \text{ (sec)} \quad (6.7)$$

$$t^* = t_{pe} + Y \text{ (sec).}$$

Eq. (6.6) applies for times greater than t^* ; note that t_{pe} is an approximation to the time of pressure equilibrium, i.e., at earlier times there are major pressure forces giving rise to vigorous motions. The first term in Eq. (6.6) is the initial fireball radius, the second accounts approximately for expansion. An approximate expression for the rise velocity of low altitude fireballs, again for the first 60 sec after burst, is

$$v_{rise} = 0.11 Y^{0.2} (\rho_o/\rho)^{0.15} \text{ (km/sec)} \quad (6.8)$$

6.2.3.2 Blast

The partitioning of energy between blast and thermal output begins to change above 10 km altitude, and thus a simple blast efficiency factor

$$B_{eff} = \text{Max}[\text{Min}(1; 1.15 - 0.015 H); 0] \quad (6.9)$$

where H (km) = height of burst. Thus $B_{eff} = 1.0$ at $H = 0$, 0.85 at 20 km, 0.4 at 50 km, and 0 for $H > 77$ km.

³⁶ An *air burst* is one detonated so high that the fireball does not interact with the ground; in the following Section (6.2.4) we discuss bursts that do interact with the ground.

Peak overpressure (traditionally expressed in psi) is obtained by scaling the effective blast yield $B_{\text{eff}}Y$ (Mt) to a standard 1 kt explosion at sea level. Figure 6.5 is a plot of this standard free-air burst taken from Glasstone & Dolan, 1977; the dashed curve is a fit of the functional form that follows [Eq.(6.10)].

With horizontal range from the burst expressed in km, peak overpressure for the standard burst can be approximated by

$$PST = 10^{[18.7/(\log D_{ST} + 3.72) - 5.0]} \quad (6.10)$$

where

$$\begin{aligned} PST &= \text{overpressure for 1 kt at sea level (psi)} \\ D_{ST} &= \text{horizontal range at sea level (km)} \\ D_{ST} &= D / Y_{\text{SCALE}}^{1/3} \quad (\text{km}) \\ D &= \text{actual horizontal range (km)} \end{aligned} \quad (6.11a)$$

$$\begin{aligned} Y_{\text{SCALE}} &= \text{scale blast yield (kt)} \\ Y_{\text{SCALE}} &= 1000 B_{\text{eff}} Y / p_{\text{amb}} \quad (\text{kt}) \end{aligned} \quad (6.11b)$$

$$p_{\text{amb}} = \text{ambient pressure (atm.)} = 2.83 T_{\text{amb}}(\text{K}) \rho_{\text{amb}}(\text{g/cm}^3) .$$

This formulation assumes that the ambient pressure is approximately constant between the burst altitude and the altitude of interest.

Overpressure at the point of interest is

$$p = PST p_{\text{amb}} \quad (\text{psi}) \quad (6.12)$$

Dynamic pressure (= kinetic energy per unit volume of air just behind the shock front) is³⁷

$$q = (5 p^2 / 2) / (7 \times 14.7 p_{\text{amb}} + p) \quad (6.13)$$

and the shock velocity at any altitude is

$$V = a \{ 1 + [6 p / (7 \times 14.7 p_{\text{amb}})] \}^{1/2} \quad (\text{m/sec}) \quad (6.14)$$

where a = sound speed at this altitude = $340 (T_0/T)^{1/2}$ (m/sec) if T_0 = temperature at sea level and T = temperature at relevant altitude.

³⁷ This formula assumes that $\gamma = c_p/c_v = 1.4$ and that sea level pressure is 14.7 psi.

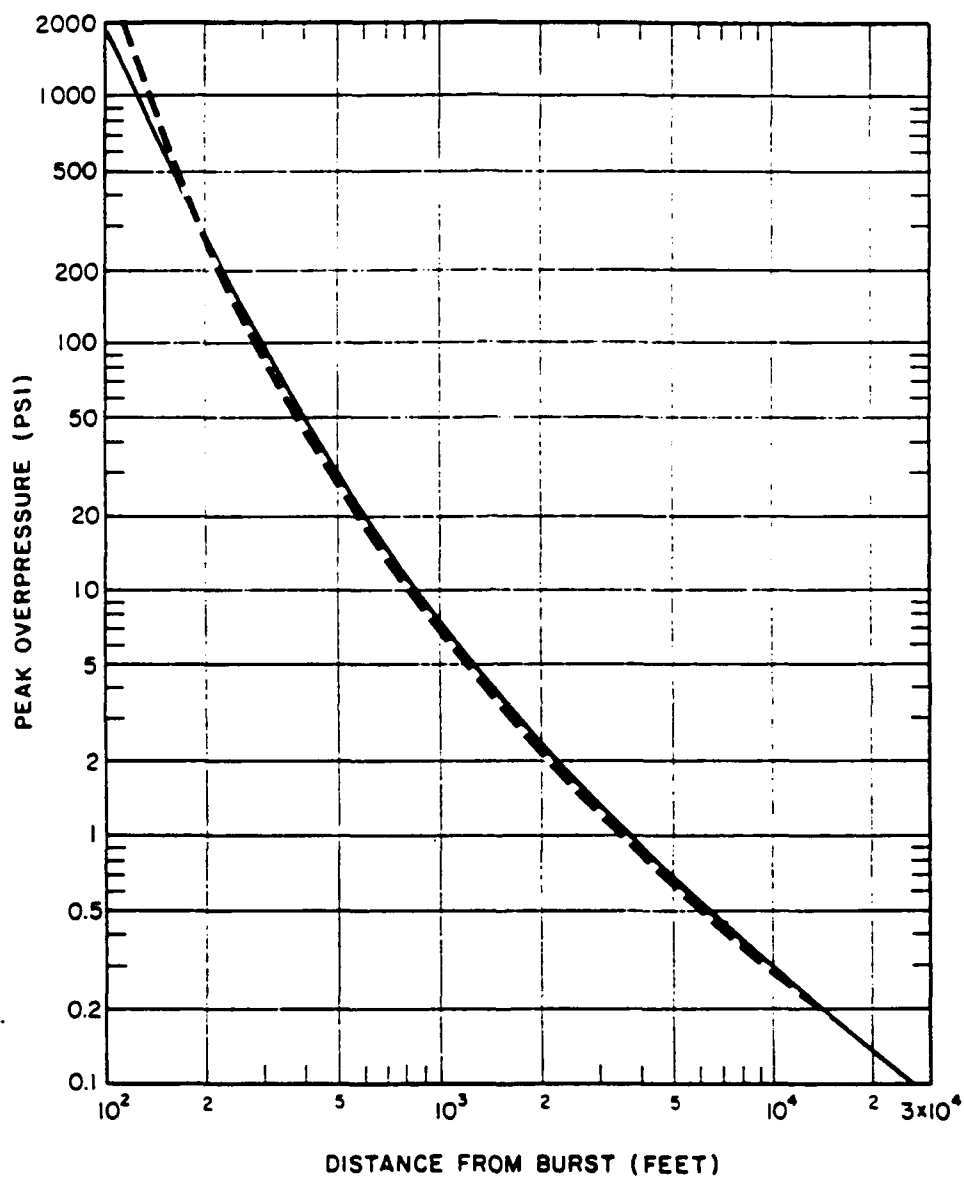


Figure 6.5. Peak Overpressure from a 1 Kiloton Free Air Burst for Sea Level Ambient Conditions. [Solid curve--Glasstone & Dolan, 1977, p.109; dashed curve-Eq.(6.10)]

6.2.3.3 Thermal Fluence

At altitudes up to about 250 km, this can be expressed as

$$\text{Fluence} = 10^5 f Y \tau / (4\pi R^2) \quad (\text{cal/cm}^2) \quad (6.15)$$

where τ = atmospheric transmission

R = range from burst point to field point (km)

f = fraction of total weapon energy emitted as thermal radiation, which can be approximated as:

$$f = 0.5 \quad \text{for } 0 < H < 70 \text{ km} \quad (6.16a)$$

$$f = 1.2 - H/100 \quad \text{for } 70 \text{ km} < H < 115 \text{ km} \quad (6.16b)$$

$$f = 0.05 \quad \text{for } 115 \text{ km} < H < 250 \text{ km} \quad (6.16c)$$

6.2.4 Near-Surface Bursts

When a bomb is detonated so close to the ground that the explosion interacts with the ground, a crater will be formed and a large fraction of the energy goes to produce this crater and to send a shock wave through the ground. Because the earth density is larger (by a factor ~ 1000) than the air density, the crater radius will be significantly smaller than the fireball radius; thus, for a 1 Mt near (but below!) surface burst the radius of the crater is on the order of 200 m, while the radius for a 1-Mt airburst at thermal minimum is ~ 400 m (see ENW, 1977). This ground shock due to a surface burst will lead to structural damage. As the height of burst decreases so that the interaction of the explosion with the ground becomes stronger, more of the energy goes to produce a crater and to send a shock through the ground. For a discussion of ground and subsurface bursts, see ENW, 1977, Ch. 6.

When a bomb is detonated so close to the surface that the fireball touches the ground, a crater will be formed and a--possibly large--dust cloud will be sent into the atmosphere. Figure 6.6 shows the anticipated mass of dust that is lofted for a given yield as a function of the "scaled height of burst"--which scales with yield as $Y^{1/3}$. Figure 6.6a shows the data base, and Fig. 6.6b a currently accepted model. Typically, the dust particles will be quite small--mainly less than $1 \mu\text{m}$ --but the results are, of course, highly variable, depending on the local geology.

There are very few larger particles ($> 1\text{-}10 \mu\text{m}$), but they are particularly important for public health because a large fraction of the radioactivity produced mainly by fission

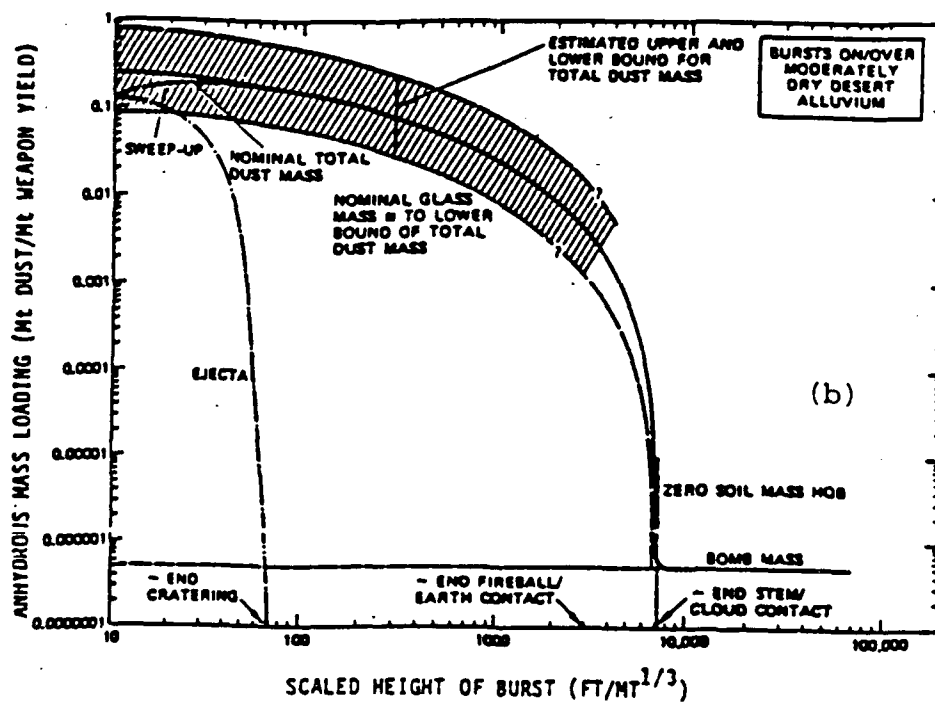
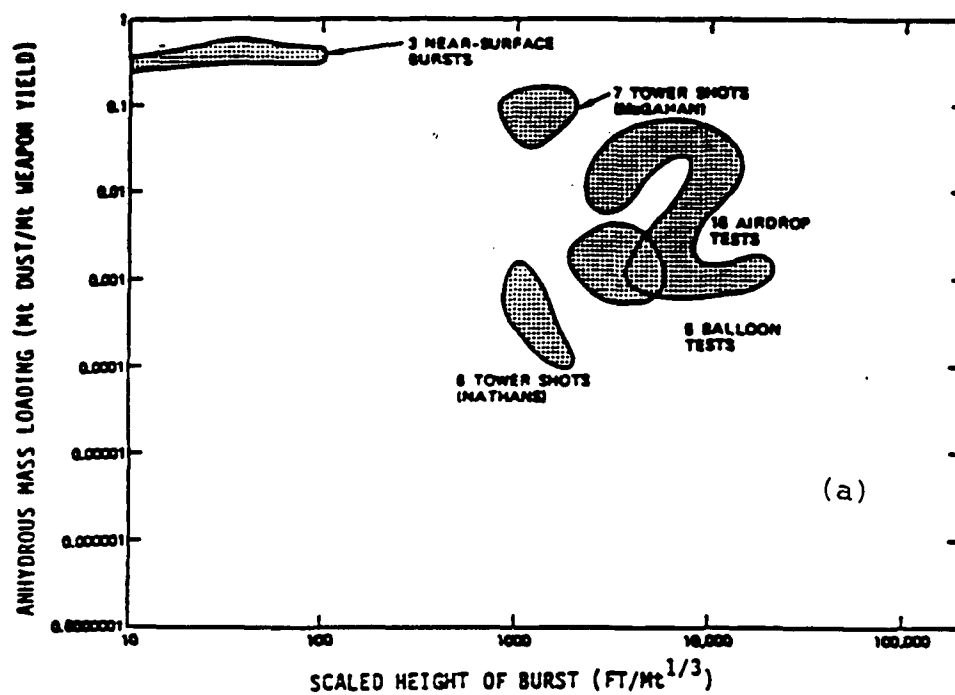


Figure 6.6. Dust Mass Lofted Into the Stabilized Cloud by a Near-Surface Nuclear Explosion. (Source: Rausch et al., 1988)
(a) Data Base, (b) Model.

and by neutron activation condenses on their surface. These large particles drift in the wind and are eventually deposited as radioactive fallout, which produces a serious long-term health hazard for people (see ENW, 1977, Ch. 9 and 12).

6.2.5 Damage Mechanisms in the Lower Atmosphere

In the lower atmosphere a nuclear explosion creates a fireball which produces both a strong blast wave that carries some 60-65 percent of the total energy of the detonation and is a major source of damage and also thermal radiation, which typically carries 30-35 percent of the energy of a near-surface burst. Nuclear radiation, principally neutrons and gamma-rays, both "prompt" and "delayed," produce some damage, while some long-term injuries to people are caused by radioactive fallout.

Some representative damage radii on the ground for a 1 Mt bomb detonated at an altitude of 1 km above the surface are the following:

- Fireball radius at thermal minimum³⁸ 0.44 km (ENW, 1977, p. 70)
- Fireball radius at breakaway³⁹ 0.53 km (ENW, 1977, p. 70)
- Peak dynamic pressure at the surface (ENW, 1977, p. 117):

100 lb/in ²	1.7 km
10 lb/in ²	2.4 km
1 lb/in ²	4.3 km
- Radiant energy (~ 35 percent of energy) (ENW, 1977, p. 291):

30 cal/cm ²	7 km
3 cal/cm ²	16 km
- Neutrons (prompt and delayed) (ENW, 1977, p. 347):

300 rad (tissue)	2.1 km
30 rad (tissue)	2.6 km
- Gammas (prompt and delayed) (ENW, 1977, p.334):

300 rad (tissue)	2.7 km
30 rad (tissue)	3.3 km

For more detail and an indication of damage levels,⁴⁰ see ENW, 1977, or EM-1.

³⁸ Defined in Section 6.2.2.

³⁹ Defined in Section 6.2.2.

⁴⁰ The rad is a unit of absorbed radiation, characterized by the absorbing material (tissue for biological effects, Si for electronics, etc.). 1 rad = 100 erg nuclear or ionizing radiation per gm absorbing material. See also footnote ** on Table 6.2.

6.2.6 Electromagnetic Pulse (EMP)

When a nuclear weapon is detonated, a large amount of ionization is produced very rapidly from the deposition of X-rays and γ -rays, in a time of order 10^{-8} sec. If the ionized region is not spherically symmetric, typically as a result of the effects of the ground or of the variation of atmospheric density with height (~ 7 km scale height), the electromagnetic field produced by this ionization produces a large RF radiated signal, the Electromagnetic Pulse.

The character of this field varies significantly, depending on the presence of the ground (conducting ground plane) and on the ambient atmospheric density. Thus, for surface and very low air bursts the maximum field strength is on the order of keV/m, extending out to some 10-20 km from the burst because most of the X-rays and γ -rays are absorbed in this region. For intermediate altitude air bursts (20-50 km height of burst) for which there is no ground effect, the field strength is much smaller, in the range of tens to hundreds of eV/m, and with an extent which may be slightly larger because of the lower ambient density. However, for high-altitude bursts, where the ambient air density is so low that no fireball is formed, the maximum field strength can again be in the range keV/m, but the geometrical extent can be very large. Thus, for a Mt-yield burst at 500 km altitude, where the ionization peaks at altitudes of 100-200 km, there will be large electromagnetic fields on the surface of the earth out to the geometrical tangent altitude range, which here would extend some 2500 km from the burst point.

These electromagnetic fields can have a very deleterious effect on unprotected electronics,⁴¹ but these effects can be minimized by proper design (screening).

For a discussion of EMP, see, e.g.,

- Ch.11 of ENW, 1977.
- *IEEE Transactions on Electromagnetic Compatibility*, Vol. EMC-20, No. 1, part 1, Feb. 1978 (also published as *IEEE Trans. on Antennas and Propagation*, Vol. AP-26, No. 1, Jan. 1978).
- Soper, 1985--for a Classified description.

A related phenomenon is *System-Generated Electromagnetic Pulse* (SGEMP), which refers to the transient electromagnetic pulse created by the electrons emitted from the

⁴¹ Or even on (long) power lines; note that following a high-altitude nuclear explosion in the South Pacific, several strings of street lights in Hawaii, some 1600 km from the burst, were affected. See Appendix H (J. Malik from Hoerlin, 1976).

surface of an electronic or other system when this is exposed to incident photons from a nuclear burst. SGEMP differs from "ordinary" EMP in that the source of electrons that produce the field is the system itself, rather than the intervening air. For a review, see Higgins et al., 1978.

6.3 HIGH-ALTITUDE NUCLEAR EXPLOSIONS

6.3.1 Phenomenology

6.3.1.1 Introduction

The low-altitude analysis of Section 6.2 applies generally for heights of burst below 30 km. At intermediate altitudes (30-60 km) the fireball is larger and more diffuse, but the effects are still quite confined. The discussion of Fig. 6.1 and Table 6.3 in Section 6.1 indicates that from the standpoint of initial absorption of energy (which is not necessarily the only factor) there will be a confined fireball at altitudes below approximately 60-80 km.

At higher altitudes things are quite different. Quoting from ENW, 1977, p.74:

For burst heights up to ~ 80 km the early fireball is approximately spherical (it later becomes toroidal), but at the higher altitudes it elongates vertically. Above 80 km the debris tends to be separate from the X-ray pancake. The debris can rise to great heights, unlike the X-ray pancake which is always at the same height (since it forms where downward-traveling X-rays run into the absorbing atmosphere).

For burst altitudes above 80 km there is virtually no absorption of X-rays emitted in upward directions. The downward directed X-rays are mostly absorbed in a layer of air, the "X-ray pancake" which becomes incandescent as a result of energy deposition. This pancake is more like the frustum of a cone pointing upward, 10 km thick at a mean altitude of 80 km; the radius at this height is approximately the HOB minus 80 km.

6.3.1.2 Description of W.W. White, 1989

The high-altitude regime (above, say, 100 km) is characterized by low air mass density.⁴² In this rarefied environment, the mean free paths of X-rays, UV photons and energized air particles (excluding ion-magnetic coupling) are large. Thus high-altitude nuclear explosion (HANE) disturbances cover large geographic areas. For example, the effects from a megaton-class explosion at 200 km altitude extend roughly 700 km

⁴² Air mass density at 100 km is more than a million times smaller than at the earth's surface.

horizontally out from the burst point--see, e.g., Fig.6.7.⁴³ In addition, the low electron-ion collisional radiative recombination rate in this low-density regime results in long-lasting (tens of hours), widespread regions of persistent ionization.⁴⁴

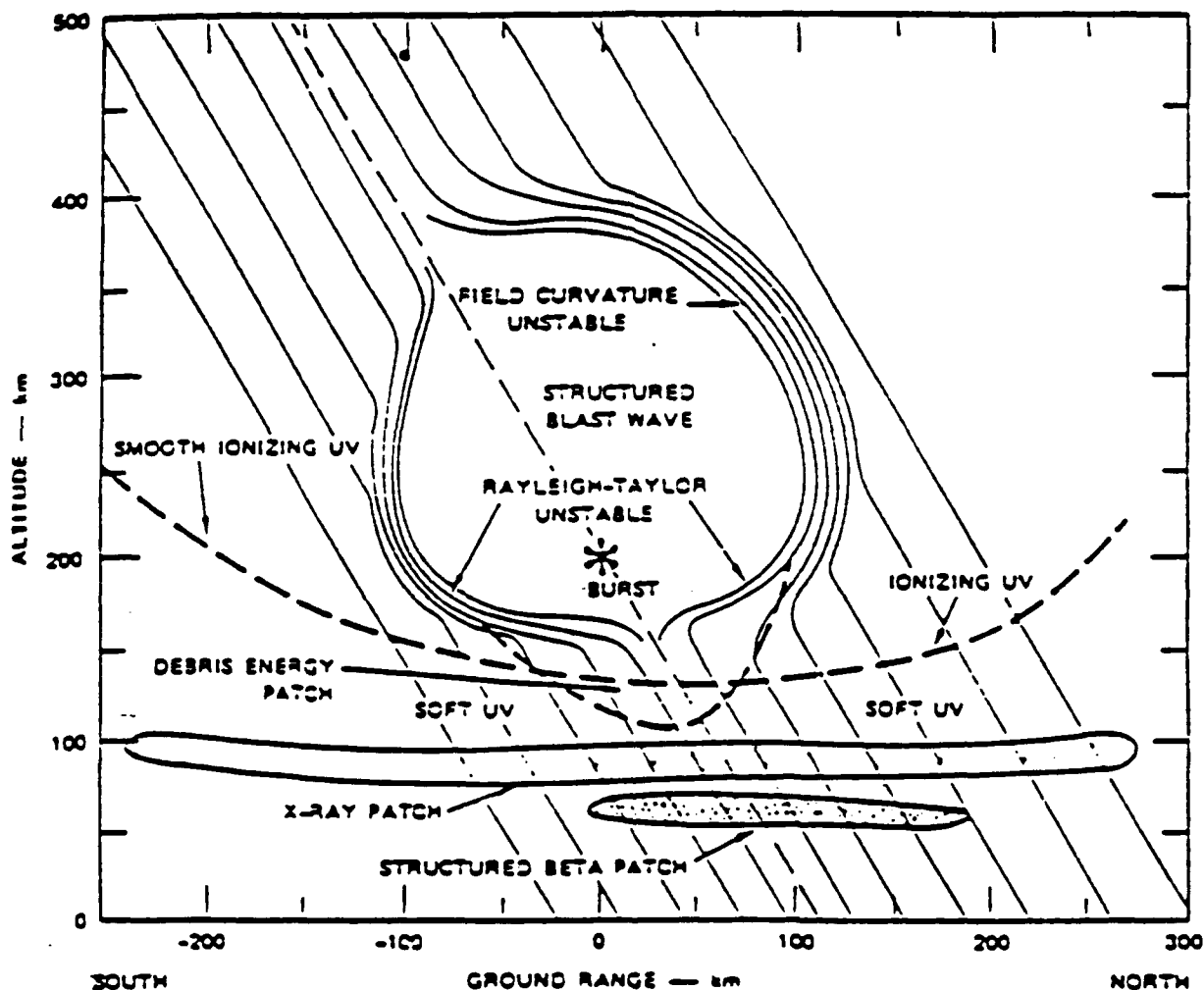


Figure 6.7. Phenomenology of High-Yield Burst at 200 km Altitude and Midlatitude. A detailed Discussion of this Figure is given in Section 6.3.1.3.

⁴³ The individual elements of Fig. 6.7 are discussed in the following Section 6.3.1.3.

⁴⁴ Dissociation due to burst energy deposition makes molecular deionization in these regions unimportant.

Evolution of the disturbed high-altitude atmosphere is usefully divided into early-time and late-time regimes, as described below.

Early-time Regime. This refers to the first minute or so following a burst. During this period, burst energy deposition and initial hydrodynamic expansion of the disturbed atmosphere occur.

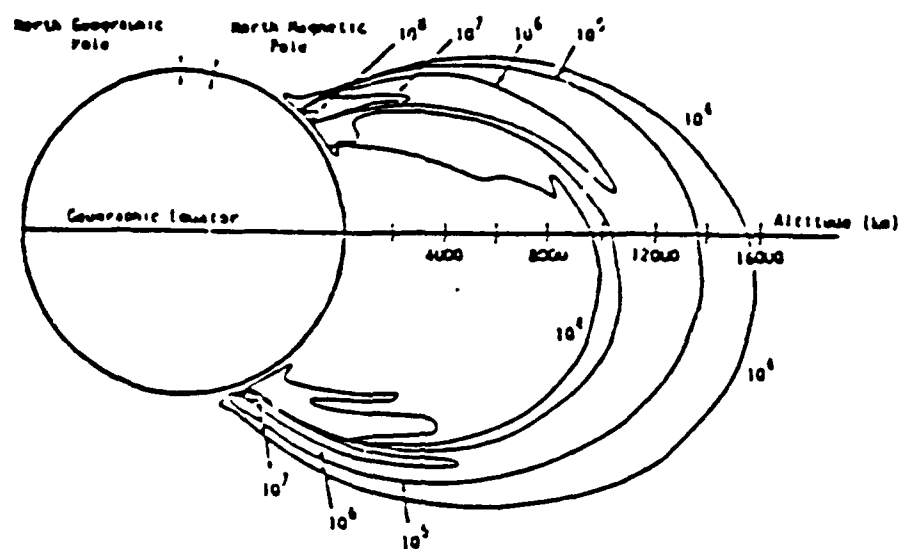
Energy Deposition. Roughly 25 percent of the energy released by a modern nuclear weapon appears as rapidly expanding weapon debris (kinetic yield), and 75 percent appears as X-rays. A small fraction of the burst energy is carried by neutrons, betas, and gammas--see Table 6.1. The kinetic yield is partitioned into a mix of UV radiation and energized air and debris ions; the relative proportion is mainly a function of burst point air density. The energized ions move up and down the (disturbed) geomagnetic field lines--see Fig. 6.8--and interact with the atmosphere to produce "patch" regions of enhanced ionization and temperature. For mid to low latitude bursts (outside the auroral oval) deposition occurs in both magnetic conjugates. For a megaton-range burst, most of the kinetic yield appears as UV radiation for burst point air densities above about 2×10^{-13} gm/cm³ (corresponding to approximately 200 km altitude in ambient air). The fraction of kinetic yield appearing as energized ions increases rapidly with decreasing burst point air density.

We distinguish three basic high-altitude nuclear burst deposition phenomenology regimes, according to how the weapon debris interacts with the atmosphere.

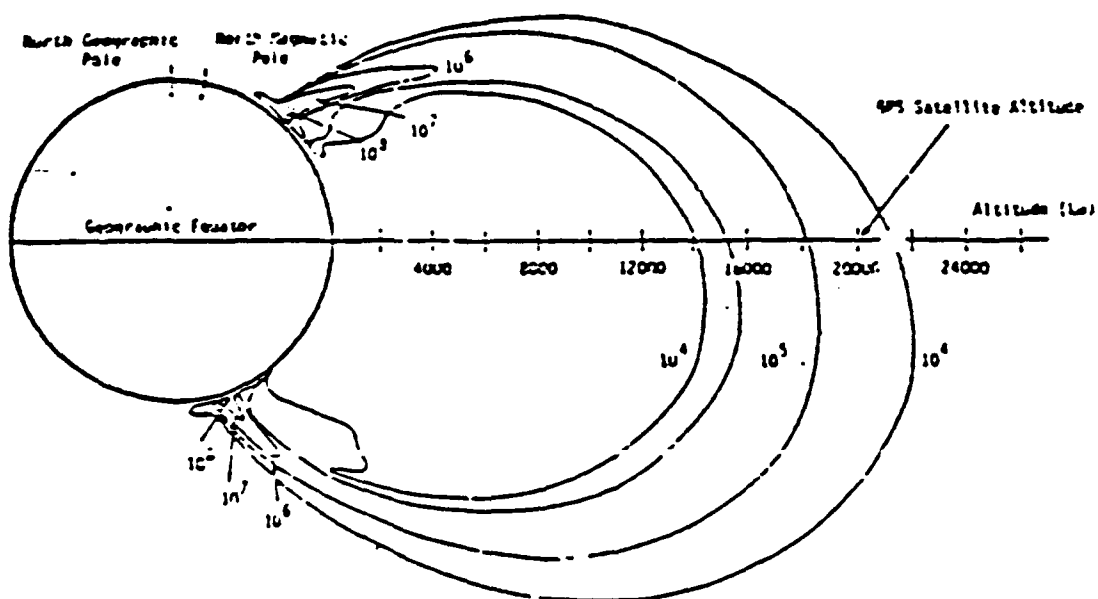
For burst point air densities above about 2×10^{-13} gm/cm³ (below about 200 km altitude in the ambient atmosphere), collisions between air and fast weapon debris ions form a debris-air "piston". The piston sweeps up air as it propagates outward, and through compression converts debris kinetic energy into thermal energy at the shock front. Excited ions emit UV photons, a significant fraction of which ionize the surrounding air, creating the UV fireball. Such bursts are in the UV REGIME.

At lower burst point air densities (e.g., 10^{-15} gm/cm³, corresponding to about 500 km altitude in ambient atmosphere), collision frequencies are too small to form a UV-radiating blast wave. Instead, debris kinetic energy is transferred to air ions by a collisionless process mediated by the geomagnetic field. As ionized weapon debris moves outward it carries along the frozen-in geomagnetic field. This compresses the field ahead of the debris and energizes the air. The debris kinetic yield is thus partitioned between energy of the air ions and the deformed geomagnetic field. Energized air ions move downward (and upward) along the geomagnetic field until they are stopped by collisions with air.⁴⁵ Bursts characterized by such energy deposition are in the KINETIC ENERGY PATCH (KEP) REGIME. For bursts at mid and low magnetic latitudes, patch formation is expected at both northern and southern magnetic conjugate regions.

⁴⁵ In the 100-200 km altitude range for a burst in ambient air.



Electron density contours (cm^{-3}) at 30 minutes.



Electron density contours (cm^{-3}) at 60 minutes.

Figure 6.8. Motion of the Plume Along the Geomagnetic Field Lines

At still lower burst point air densities (below 10^{-16} gm/cm³; the corresponding altitude in the ambient atmosphere varies from 500 to 800 km depending on solar activity), almost all the debris kinetic yield is converted to magnetic energy of the deformed geomagnetic field (the air density is too small to significantly drain energy from the collisionless blast wave). Current understanding in this area is somewhat provisional, however, and the physical processes likely to be operative are still subjects of active research. Furthermore, no nuclear tests were ever conducted in this density regime, so direct observational guidance is not available. Nevertheless, it is thought that perhaps half the debris kinetic energy will be contained and guided to the magnetic conjugates by the geomagnetic field. Formation of ionized regions similar to KEPs is anticipated. Depositions of this type are in the MAGNETIC CONTAINMENT REGIME (MCR).

Of the three energy deposition regimes, UV, KEP, and MCR, UV is best understood, and MCR least understood. In general, divisions between these regimes are not sharp; an explosion will generally be characterized by a mixture of phenomenologies.

Burst energy deposition takes place in a short but finite time ($\sim 10^{-7}$ - 10^{-6} sec). PROMPT CHEMISTRY also occurs concurrently with the deposition. Processes include photodissociation, photoionization, charge exchange, collisional excitation, and so on.

Hydrodynamic Expansion. In the high-altitude regime, the vertical extent of the initially heated region is much larger than the atmospheric density scale height. Thus the hydrodynamic response to the burst-induced pressure gradients results in predominantly upward expansion of the nuclear-disturbed air ("ATMOSPHERIC HEAVE"--see Section 6.3.3).

The relatively high temperatures and densities in the main deposition region lead to strong ion-neutral collisional coupling in the initial expansion. Thus the early-time expansion can be approximately described by single-fluid hydrodynamics. In addition, high gas kinetic pressures produce a high-beta plasma⁴⁶ in which the magnetic field is carried along with the hydrodynamic flow.

As the disturbed atmosphere expands and cools, ion-neutral collisional coupling weakens, plasma beta decreases, and the geomagnetic field relaxes towards its ambient configuration. After about one minute a TWO FLUID MHD description of the evolving atmosphere is required.

Also during this period DEIONIZATION CHEMISTRY acts to reduce the high level of initial ionization produced by the explosion. Where molecules are abundant, recombination proceeds rapidly by molecular dissociative

⁴⁶ Beta = (gas pressure)/(magnetic pressure, $B^2/8\pi$) > 1.

recombination.⁴⁷ Deionization also occurs by direct electron-ion collisional-radiative recombination.

Late-Time Regime. In the LATE-TIME PHASE, ions and electrons tend to move along the geomagnetic field (now relaxed to near-ambient) while the neutrals are not directly affected by the field. Plasma and ionized weapon debris stream along field lines to very high altitudes. A weak ion-neutral coupling permits the two fluid components to slip through one another, and a two fluid MHD approach is required to adequately treat the late-time physics.

Superposed on the primary parallel-to-B motion is an ExB drift of the plasma perpendicular to the field. The electrical field is generated by collisional coupling of the plasma with the neutral wind, the inertial force due to plasma motion along the curved geomagnetic field, gravitation, and other less important drivers. Because the parallel-to-B electrical conductivity is large, individual magnetic flux tubes are nearly equipotential. This produces an ExB drift which preserves field-aligned plasma structures and results in a nearly incompressible (actually, magnetic-flux-conserving) flow. For bursts in the northern hemisphere, overall ExB plasma drift is northward.

Fluid and kinetic instabilities in the nuclear-generated plasma cause density irregularities to develop. This spatial structure involves a broad spectrum of scale sizes covering many orders of magnitude. By late times these structures extend thousands of kilometers along magnetic field lines forming a system of FIELD-ALIGNED STRIATIONS. These field-aligned density irregularities can severely degrade radar and satellite communication link performance.

During the late-time phase the plasma plume rises to very high altitudes. Plasma density decreases largely through expansion; below 10^9 electrons/cm³, recombination proceeds slowly and large regions of substantial ionization persist to very late times.

The overall picture described here presents the large-scale structure at various times. Note that this picture is not uniform and static:

- (i) there are substantial winds and the plume rises quite rapidly
- (ii) there is a great deal of small-scale non-uniformity. Thus as the bomb comes apart there is small-scale turbulent structure, and then striations (on a transverse scale of 1-10 km) develop in the first 1-10 sec and last for long times, ~ 30-60 minutes or even longer.

⁴⁷ Ion-molecule reaction to produce molecular ions NO⁺ and O₂⁺ which have a lower ionization potential than the atomic ions N⁺ or O⁺, followed by the rapid dissociative recombination reactions NO⁺ + e⁻ => N' + O" and O₂⁺ + e⁻ => O' + O", where the primes denote possible electronic excitation of the resulting atoms.

It must be stressed that the details of this structure represent the result of 20 years of synthesis of rather limited data, and of computer modeling and analog experiments (Barium cloud releases, Auroral studies, etc.).

The debris clouds from high-altitude nuclear explosions rise by buoyancy and expand as they do so. They rise much more than do the fireballs from low-altitude air bursts because of the very much lower ambient density. High-altitude explosions send their ionized debris a very long way, typically along the geomagnetic field lines. The debris produces a large number of secondary electrons which can give rise to dramatic auroral displays, and some of which can also be trapped by the geomagnetic field to enhance the (Van Allen) radiation belts--see, e.g., Hoerlin, 1976.

6.3.1.3 Discussion of the Different Features of Fig. 6.7⁴⁸

Figure 6.7 shows the overall phenomenology regions according to current nuclear models. This figure (which applies to a Megaton-yield bomb detonated at around 200 km at mid-latitudes--results are typical for $t = 1-10$ sec after burst) is very instructive, and the individual features are discussed here.

- (a) *X-ray patch* at 70 km altitude with horizontal extent of up to 1000 km. This is produced by the absorption of X-rays emitted from the bomb in a generally downward direction where they are absorbed by the atmosphere; X-rays emitted in an upward direction are generally not absorbed in the very diffuse atmosphere at higher altitudes.
- (b) *Beta-patch* (somewhat smaller than the X-ray patch, but highly structured) produces ionization down to 65 km, of horizontal extent ~ 100 km. This is produced essentially from the fission β -particles in the delayed radiation.
- (c) Much of the *weapon debris* will be ionized, especially at these low densities, and thus it will tend to follow the geomagnetic field lines. Thus at different latitudes its behavior may be quite different. A conductive bubble is formed which expels the geomagnetic field lines. It creates a structured blast wave whose boundaries may be unstable due to a variety of mechanisms (Rayleigh-Taylor and Field Curvature instabilities are indicated at different regions of space). As a result of these instabilities, eventually the bubble will break up, giving rise to organized and irregular structures (striations and turbulence) which eventually lead to turbulent mixing.

⁴⁸ Sections 6.3.1.2 and 6.3.1.3 provide somewhat different perspectives to a very complex situation.

- (d) The general motion of the *debris* goes along the geomagnetic field lines: downward-moving debris will encounter the denser atmosphere and thus will be stopped and deposited as the *debris energy patch*, while the upward moving debris produces a *plume* which follows the geomagnetic field lines (see Fig. 6.8).
- (e) As the magnetic bubble expands, it generates *UV radiation* which produces ionization in a uniform way, but in addition *softer (non-ionizing) UV* is deposited in the dense lower atmosphere, leading to local heating.
- (f) Notice that some of these regions--those produced just by electromagnetic radiation--are relatively uniform, while those that are derived from charged particles show structure due to interactions with the geomagnetic field, including some instabilities.

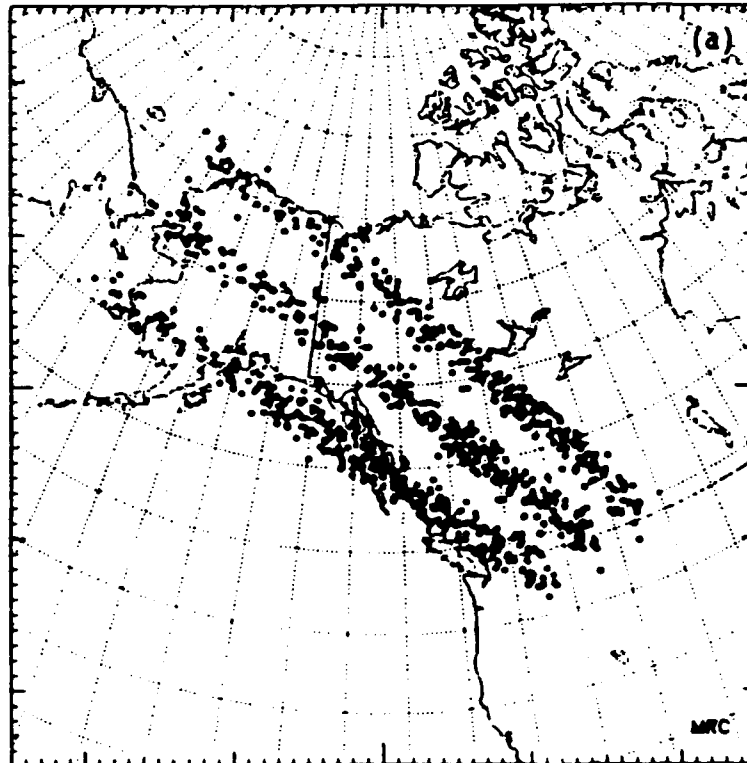
These are clearly very large-scale structures which survive for rather long times. The bubble of Fig. 6.7 is typical of conditions ~ 1-10 sec after burst, while the global scale processes of Fig. 6.8 last for minutes to hours.

6.3.2 Multiburst Phenomenology

At high altitudes where the density is low, the energy from a nuclear explosion travels a long distance before being absorbed in the atmosphere, and thus there is the possibility for interaction between neighboring bursts. In terms of current nuclear arsenals of both the US and USSR, the possibility of massive multiburst scenarios, involving some hundreds to thousands of nuclear explosions sufficiently close together (in space and time) so that interaction can occur, cannot be excluded. Thus we ask in what way such multiburst scenarios give rise to different phenomenology from that for the case of a single burst as discussed in Section 6.3.1.

Figure 6.9 gives the results of a "Massive Multiburst" computation which has been performed recently (1986-87) by MRC for DNA using the SCENARIO code. A total of 1000 one-Mt bursts are detonated at a rate of 10 every 10 sec along three ICBM trajectories, corresponding to minimum energy, lofted and elevated trajectories, and a spacing so close that there is significant interaction, and yet far enough away so that fratricide can be avoided. Figure 6.9a shows the horizontal spacing of the bursts, Figs. 6.9b and 6.9c show the total mass density and electron density 1 min into the laydown, i.e., after 60 bombs have been detonated, while Figs. 6.9d and 6.9e show the

total mass density and electron density after the last of the weapons have been detonated. The locations of the bursts are shown in all these figures.⁴⁹

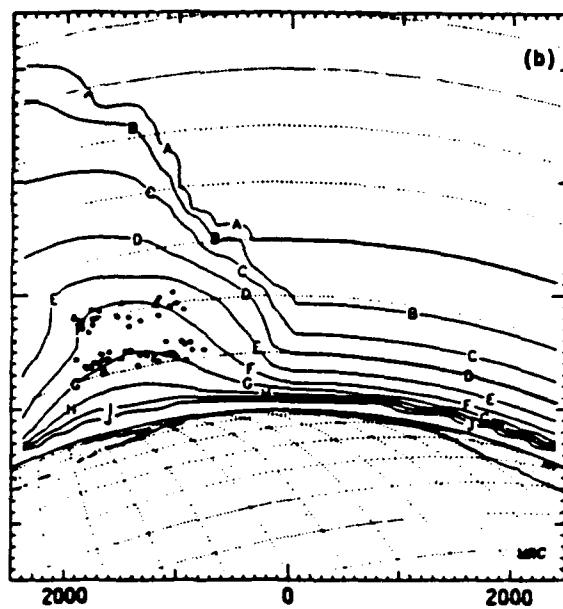


(continued)

Figure 6.9. Massive Multiburst, Case MS-1.1 (Source: White et al., 1987a).

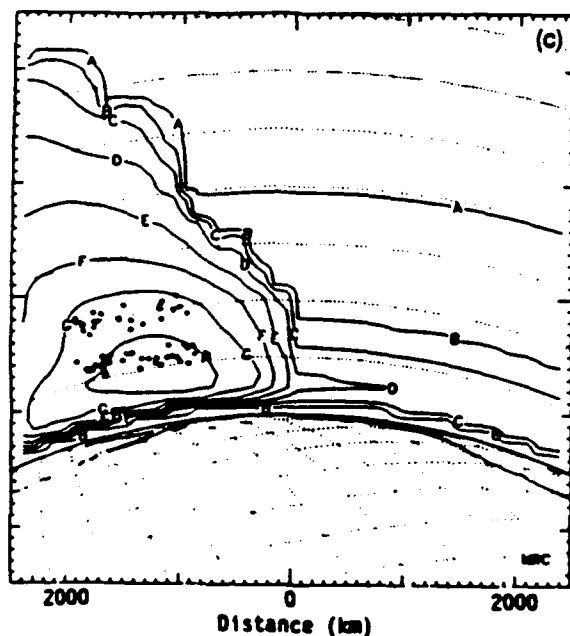
- (a) Vertical view showing the location of the bursts over the earth;
- (b) Total mass density at $t = 1$ minute (60 bursts);
- (c) Electron density at $t = 1$ minute;
- (d) Total mass density at $t = 16.7$ minutes (1000 bursts);
- (e) Electron density at $t = 16.7$ minutes.

⁴⁹ The quantitative results of this simulation are now (mid-1990) considered obsolete, although the general characteristics aren't changed. You should ask DNA/RAAE for up-to-date results.



Contour Values (gm/cm³):

A = 10 ⁻¹⁸	B = 10 ⁻¹⁷	C = 10 ⁻¹⁶	D = 10 ⁻¹⁵	E = 10 ⁻¹⁴
F = 10 ⁻¹³	G = 10 ⁻¹²	H = 10 ⁻¹¹	I = 10 ⁻¹⁰	J = 10 ⁻⁹



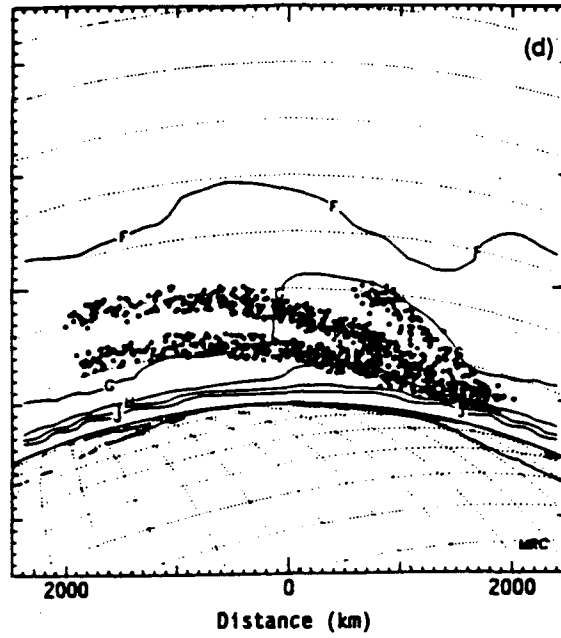
Distance (km)

Contour Values (electrons/cm³):

A = 10 ³	B = 10 ⁴	C = 10 ⁵	D = 10 ⁶	E = 10 ⁷
F = 10 ⁸	G = 10 ⁹	H = 10 ¹⁰	I = 10 ¹¹	J = 10 ¹²

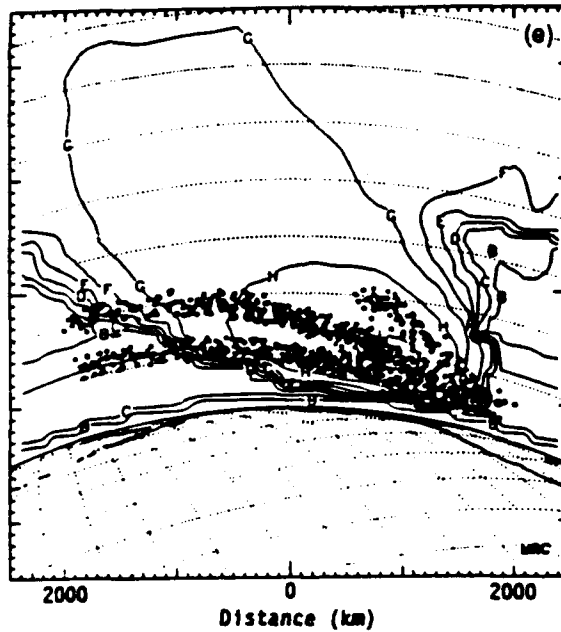
(continued)

Figure 6.9. (continued)



Contour Values (gm/cm^3):

A = 10^{-18}	B = 10^{-17}	C = 10^{-16}	D = 10^{-15}	E = 10^{-14}
F = 10^{-13}	G = 10^{-12}	H = 10^{-11}	I = 10^{-10}	J = 10^{-9}



Contour Values ($\text{electrons}/\text{cm}^3$):

A = 10^3	B = 10^4	C = 10^5	D = 10^6	E = 10^7
F = 10^8	G = 10^9	H = 10^{10}	I = 10^{11}	J = 10^{12}

Figure 6.9. (continued)

Note that the ambient ionosphere is modified drastically: the ionization is enhanced by a factor up to 10^6 and the neutral density is enhanced by a comparable or even larger factor at the higher altitudes. The enhanced ionization can be understood quite simply in terms of the ionization of ambient atoms and molecules by incident X-rays and UV radiation. The enhancement in neutral density is induced by the buoyant rise of air heated by the absorption of X-rays or debris kinetic energy. This phenomenon is called *Heave* and is discussed in Section 6.3.3. At the moment let us simply note that Fig. 6.10 shows the enhancement in total density--both mass density (kg/m^3) and number density (no./cm^3)--due to multiple nuclear explosions [cases P(60) and H(1000) of Fig. 6.9] and Fig. 6.11 shows the plasma temperature.⁵⁰ Both these figures are discussed in Section 6.3.3.

The detailed numbers should not be taken too literally: note that the enhancement in total and ionization density is very large but suggests saturation behavior, i.e., the electron density does not exceed 10^{10} - 10^{11} cm^{-3} over large regions of space while the density enhancement below $\sim 200 \text{ km}$ is very small. The heave phenomenon will be discussed next, in Section 6.3.3.

Applications for system performance are discussed in Section 6.4; the ionization (which affects electromagnetic signal propagation) is discussed in Section 6.4.2, and the enhancement in radiation ("Redout") is taken up in Section 6.4.3. Both these quantities are functions of the plasma temperature. Finally, the overall quality of the predictions and its implications on system performance are taken up in Section 6.5.

6.3.3 Heave

McNamara (1985) describes atmospheric heave as "the comparatively slow, generally adiabatic motion of large regions of the upper atmosphere following energy deposition by a high-altitude nuclear detonation." This definition needs some qualification and amplification because the upward speed increases greatly with altitude, and because the motion of a heated air parcel of radius R becomes *ballistic* rather than *buoyant* at altitudes above about 50 km --see, e.g., Sowle, 1977, pp. 480f and 505f.

⁵⁰ Above 100 km the atmosphere is significantly out of LTE (Local Thermodynamic Equilibrium) so that it is not meaningful to speak of a *Temperature*. However, one can define a *Plasma Temperature* in terms of the degree of ionization of the ambient atmosphere--cf., e.g., Part I of these Notes, Section 2.

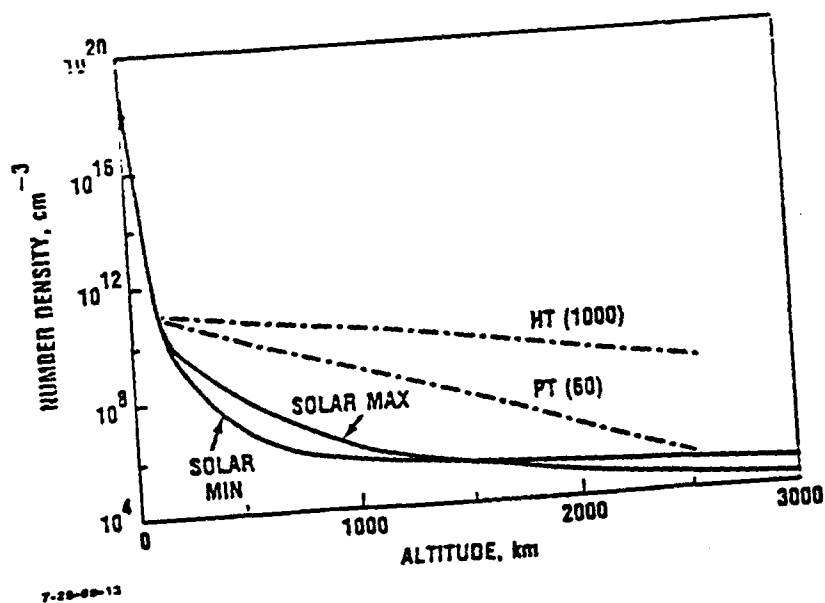
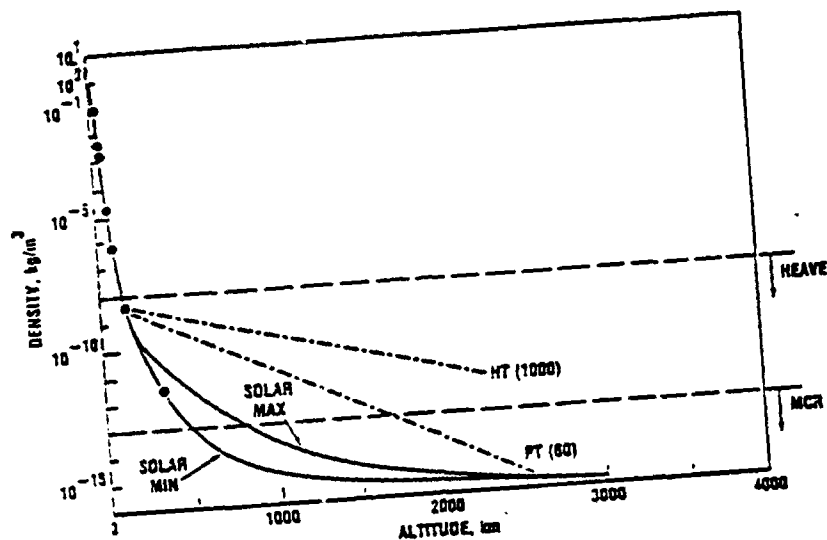
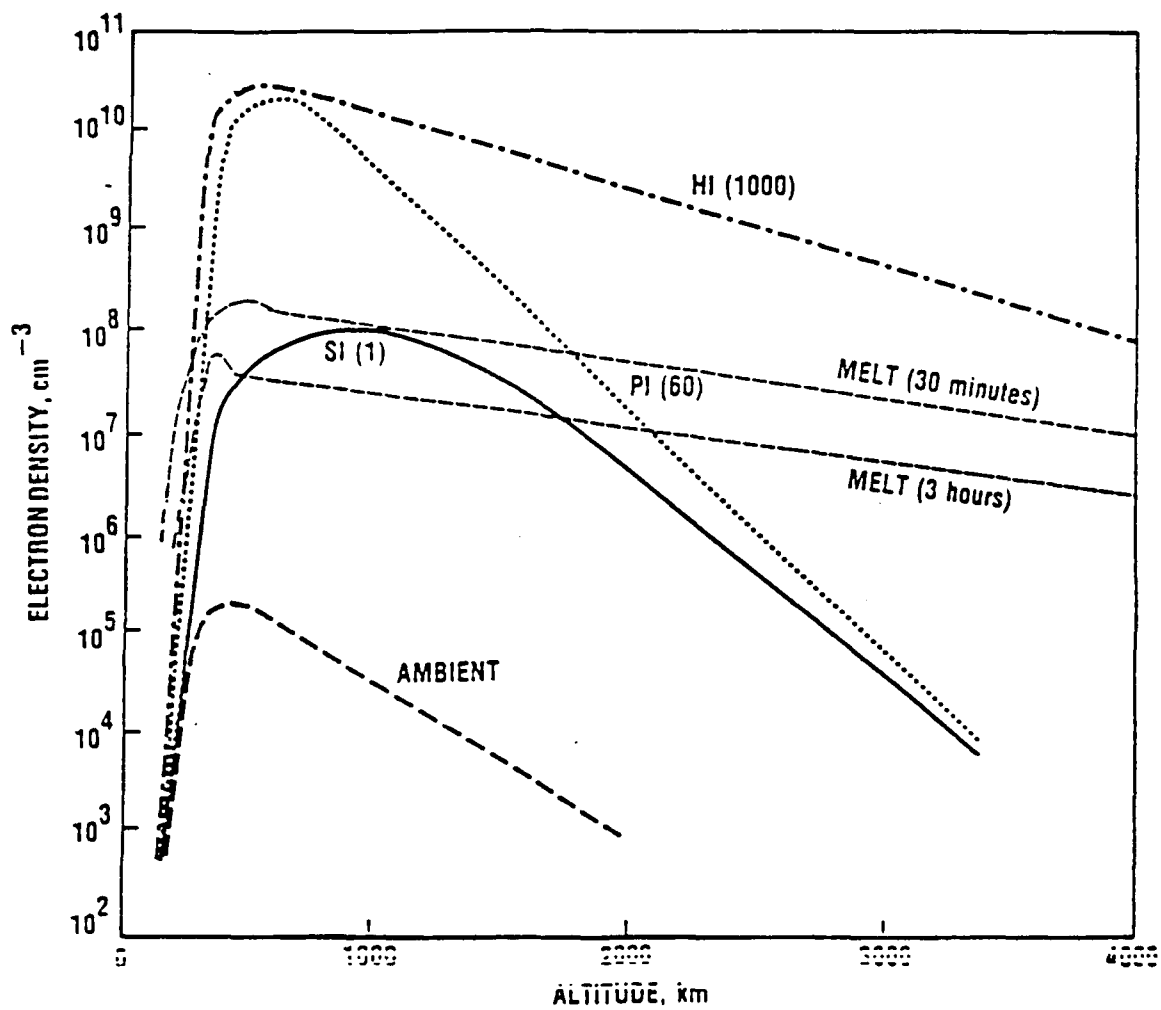
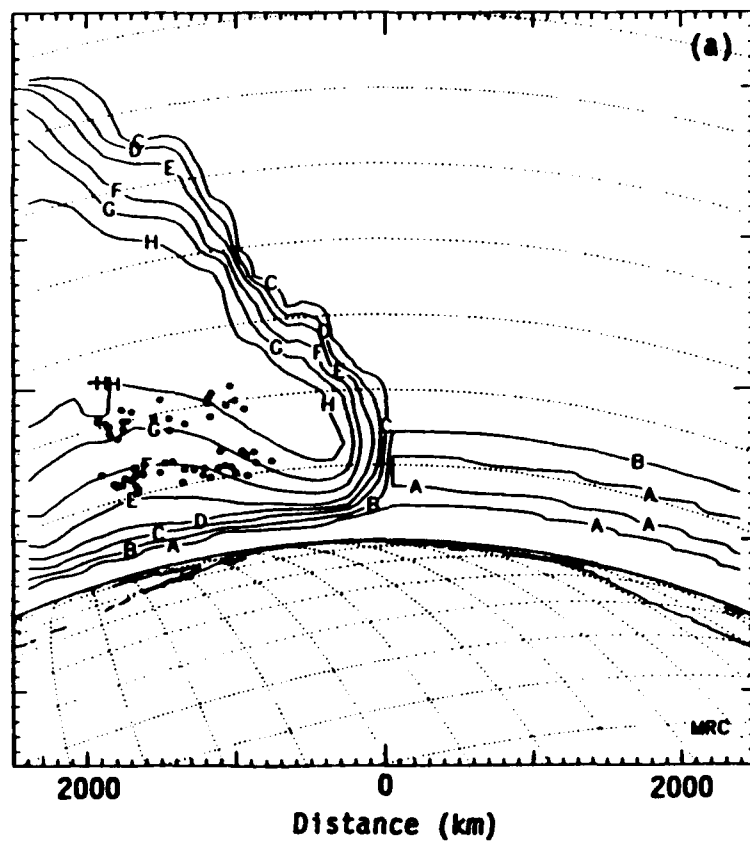


Figure 6.10. Enhanced Total Density due to Heave from Multiple Nuclear Explosions. (We show the ambient density corresponding to low and high solar activity, and the perturbed density P(60) along the plume corresponding to 60 one-Mt bursts, and the general heave H(1000) due to 1000 one-Mt bursts.) Both Mass and Number Density are Shown, in kg/m^3 and no./cm^3 respectively. High-altitude nuclear test data are indicated.



7-25-89-12

Figure 6.11. Enhanced Plasma Temperature due to Multiple Nuclear Explosions [Calculations for the 1000-burst case MS at (a) $t = 1$ min, (b) $t = 2$ min, and (c) $t = 16.4$ min]

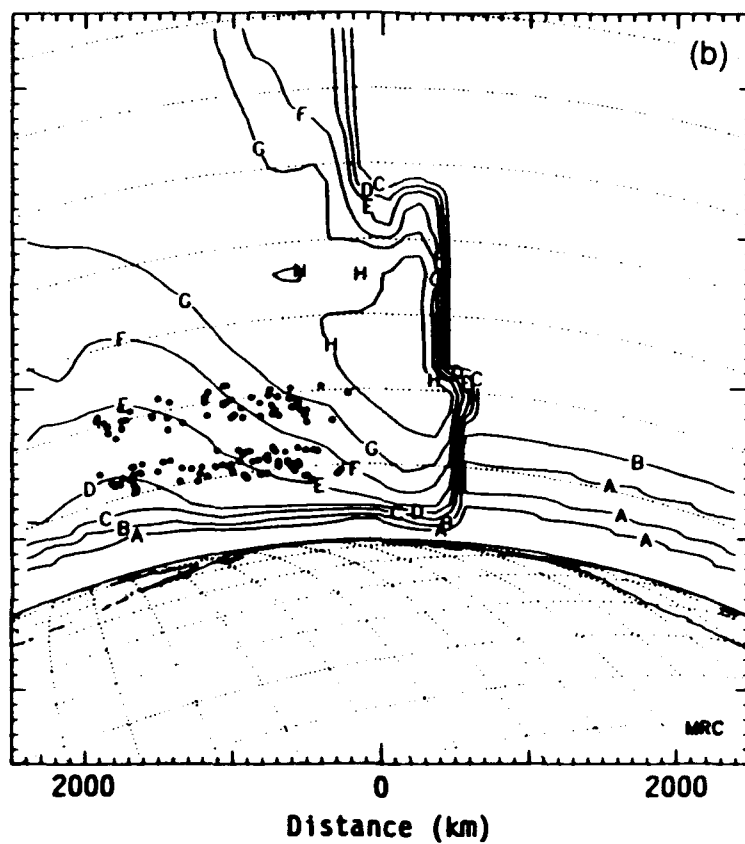


Contour Values ($^{\circ}\text{K}$):

$A = 1 \times 10^3$	$B = 2 \times 10^3$	$C = 5 \times 10^3$	$D = 1 \times 10^4$	$E = 2 \times 10^4$
$F = 5 \times 10^4$	$G = 1 \times 10^5$	$H = 2 \times 10^5$	$I = 5 \times 10^5$	$J = 1 \times 10^6$

(continued)

Figure 6.11. (continued)



Contour Values ($^{\circ}\text{K}$):

$A = 1 \times 10^3$	$B = 2 \times 10^3$	$C = 5 \times 10^3$	$D = 1 \times 10^4$	$E = 2 \times 10^4$
$F = 5 \times 10^4$	$G = 1 \times 10^5$	$H = 2 \times 10^5$	$I = 5 \times 10^5$	$J = 1 \times 10^6$

Figure 6.11. (continued)

In an atmosphere at constant temperature T , the density $\rho(z)$ falls off with increasing altitude z as follows:

$$\rho(z) = \rho(z_0) \exp - (z - z_0)/H \quad , \quad (6.6a)$$

where the scale height H is given by the expression

$$H = kT/Mg \quad . \quad (6.6b)$$

$H \sim 7$ km at altitudes below 100 km where the temperature is ~ 200 -250 K; above 200 km altitude, where $T \sim 700$ -1500 K and the atomic oxygen is dissociated so that the effective molecular weight is typically 18 (rather than 29), $H \sim 50$ km.

An air parcel of radius R is said to rise *buoyantly* if $R \ll H$, and *ballistically* if $R \gg H$. Buoyant rise, which occurs at relatively low altitudes, corresponds to relatively slow, adiabatic rise of the air parcel which maintains a uniform pressure, while ballistic rise, which takes place lower densities is relatively rapid with pressure varying in the parcel.

For definiteness, consider bursts above 300 km, and ask for the motion as a function of altitude. Most of the energy of a bomb comes out as X-rays (see Table 6.1) and downward-traveling keV X-rays are absorbed near 80 km - see Table 6.3- where the fractional energy deposition is so small that the atmospheric rise velocity is quite small. Some of the X-ray energy that is propagated obliquely, as well as UV energy emitted by the burst, are absorbed in the 100-200 km altitude region and can lead to substantial heave (i.e., a relatively large mass moving at relatively high velocity $u_H \sim 5$ -10 km/sec). Also, that part of the kinetic energy of the debris that moves down (mainly along the geomagnetic field lines), produces a shock in the atmosphere below ~ 250 km and is stopped at altitudes near 150-200 km, giving rise to a large energy deposition as compared to the ambient thermal energy and thus producing substantial heave over a large horizontal area.

Heave is particularly important for high-altitude multiple burst scenarios where there is a large fractional energy deposition at high altitudes and the effects of heave cannot necessarily be modeled in terms of single detonations. There now exist some computer codes which model this behavior. Heave is illustrated particularly dramatically by the SCENARIO calculations of Figs. 6.9b and 6.9d, which show how density contours are raised to altitudes very much above ambient. Consider, for instance, contour A, which corresponds to the ambient density at 477 km. In Fig. 6.9b (corresponding to the plume of 60 Mt detonations) and immediately above the detonations (shown by black points) this contour is raised to 3000 km; at other locations it is lifted to 1500 km. In Fig. 6.9d (which

shows the heaved atmosphere following 1000 Mt explosions) the A-contour is totally out of the picture (i.e., above 300 km). Again, contour G, which corresponds to 96 km ambient altitude, is lifted above 500 km in the 60-Mt plume of Fig. 6.9b and as high as 1000 km in the 1000 Mt example of Fig. 6.9d.

Figure 6.10 shows the overall character of heave, by demonstrating the ambient atmospheric density as a function of altitude for low and high solar activity. This makes quite a difference at altitudes in the range 300-1500 km, where the density is 10^{-13} to 10^{-10} times that at sea level. The lines P(60) and H(1000) show representative values of density as a function of height for the plume corresponding to the 60-burst case of Fig. 6.9c and to the total heaved atmosphere arising from the 1000-burst environment of Fig. 6.9f. In general, heave occurs for air above 150-200 km, where the density is so low that the energy absorption rate is large enough to move air up very rapidly.

Figure 6.10 demonstrates different regions of phenomenology; at densities below 10^{-8} kg/m³ (above 200 km in the ambient atmosphere) there is heave, while at densities below 10^{-13} kg/m³ (above 500-800 km in the ambient atmosphere) the phenomenology is characterized as the "Magnetic Confinement Regime" (MCR). The circles indicate U.S. high-altitude nuclear explosions for which there is a significant amount of data; note that only two lie in the density region between 10^{-13} and 10^{-8} kg/m³ in which heave is significant. If the initial bursts of a multi-burst scenario lie in the MCR, then provided some energy absorption and thus heave occurs here (which is most probably the case) the environment of greatest interest is likely to be in the density range of 10^{-13} to 10^{-8} kg/m³. However, we have no test data in the MCR.

Note that while the physics of heave is straightforward ("hot air rises"), there is no quantitative experimental evidence for it. There is qualitative information from three U.S. high-altitude nuclear tests, and apparently also some evidence from solar flares. The available data for the highest-altitude U.S. nuclear test (SF) have not provided a complete and quantitative accounting of where the debris went. We know that the atmospheric density above ~ 500 km in the ambient atmosphere is greater at 2 p.m. than at 2 a.m. (local time) by a factor 2-5, evidently as a result of buoyancy due to solar heating. However, this is clearly an example of buoyant rise, while the essential features of heave come from the rapid absorption of energy and the reflection of a downward-moving debris-induced shock wave.

A typical rise velocity of heaved air is in the range 5-10 km/sec, which is large compared with the ambient sound velocity but small compared to the hydromagnetic Alfvén velocity⁵¹

$$v_A = B/(4\pi n_i m_i)^{1/2} \quad , \quad (6.17)$$

(~ 100 km/s) which is the appropriate atmospheric velocity.

How long does the heaved air stay up? It moves up ballistically under gravity, at speeds $u_H \sim 5-10$ km/s, and expands horizontally to mix with the ambient very-low-density medium. Eventually it falls again under gravity. The fastest possible fall rate is equal to the rise rate, i.e., the fastest fall time

$$t_{\min} \sim u_H/g \sim 8-16 \text{ min} \quad , \quad (6.18)$$

where $g = 9.8 \text{ m/s}^2$ is the gravitational acceleration.

6.3.4 Damage Mechanisms due to High-Altitude Nuclear Bursts

At high altitudes where there are no fireballs, the damage is due directly to the weapon's radiative output, i.e., X-rays, γ -rays, and neutrons--see Tables 6.1 and 6.2.

There is one additional longer-time damage mechanism arising from the presence of electrons trapped in the radiation belts. A nuclear explosion in the upper atmosphere generates a very large number of free electrons,⁵² and at sufficiently high altitudes a significant fraction of these electrons can be trapped by the geomagnetic field, serving to enhance the (Van Allen) radiation belts for times of a few days to a year. The effects of this can be particularly serious for spacecraft in orbits of 1000-2000 km radius. For a discussion, see Cladis et al., 1971, and Leong et al., 1986.

6.4 SYSTEMS IMPLICATIONS OF HIGH ALTITUDE NUCLEAR EXPLOSIONS

6.4.1 Introduction

The detonation of nuclear weapons in the upper atmosphere can affect both *System Survivability* and *System Operability*. *System survivability* is a measure of the ability of

⁵¹ In a plasma there are longitudinal waves whose phase velocity is the normal sound speed. However, there are also purely transverse waves whose phase velocity is the Alfvén velocity--cf, e.g. Jackson, 1975, p. 486.

⁵² 1 Mt roughly doubles the total number of electrons in the global ionosphere.

system elements (spacecraft, air or ground components) to survive physically even after exposure to large fluxes of X-rays, γ -rays and neutrons. Tables 6.1 and 6.2 give the exposure, which scales as $\text{yield}/(\text{range})^2$; it is possible to harden many elements to withstand substantial exposure to radiation. *System Operability* is more subtle. Some major examples are the following:

- **Electronic Upset**

When an electronic component encounters a radiation level significantly less (by several orders of magnitude) than is needed to damage it, there may still be a false signal which affects the operation of the component and of a device made up of such components. Further, after a system has been exposed to a high level of radiation, by proper engineering design and hardening there may be an outage but the system can function again (though possibly at reduced capacity) once the radiation has reverted to a normal level.

- **Electromagnetic Pulse (EMP)**

The voltage or current set up in a transmission line or in an electronic device may interfere with the operation of electronic devices, in particular with current-driven low-voltage devices which are much more sensitive to EMP than are voltage-driven vacuum tubes. Section 6.2.5 refers to more detailed calculations.

- **Communication Interference ("Blackout")**

When an electromagnetic signal is transmitted through the nuclear-perturbed environment which has not only a significantly enhanced mean degree of ionization but also large fluctuations in electron density, its propagation may be degraded significantly. A simple discussion is given in Section 6.4.2.

- **Enhanced IR Atmospheric Signature ("Redout")**

An infrared sensor looks for a target by its thermal signature. The nuclear perturbed environment frequently radiates much more than the ambient atmosphere⁵³, and thus the target may not be detectable at the ranges that are expected. Section 6.4.3 gives a simple discussion of Redout.

⁵³ Note that the IR radiation level may also fluctuate significantly, producing "clutter" which can interfere seriously with target detection.

6.4.2 Ionization Effects on Radio and Radar Propagation

6.4.2.1 Electromagnetic Wave Propagation in an Ionized Medium

At high altitudes there is a large ionized region in the atmosphere which produces long-time "blackout" for signals of frequency f less than the plasma frequency

$$f_p = (n_e e^2 / \pi m)^{1/2} = 9.0 \times 10^3 \times n_e^{1/2} \text{ (Hz)} \quad , \quad (6.9)$$

where n_e = no. electrons/cm³; if $n_e = 10^8$, $f_p = 90$ MHz, so that HF and VHF are severely affected.⁵⁴ Note that even at much higher frequencies there will be a variety of different propagation effects. Table 6.6 describes many of the more important effects on propagation due both to (enhanced) ionization and also due to small-scale spatial/ temporal structure ("striations").

6.4.2.2 The Disturbed Ionosphere

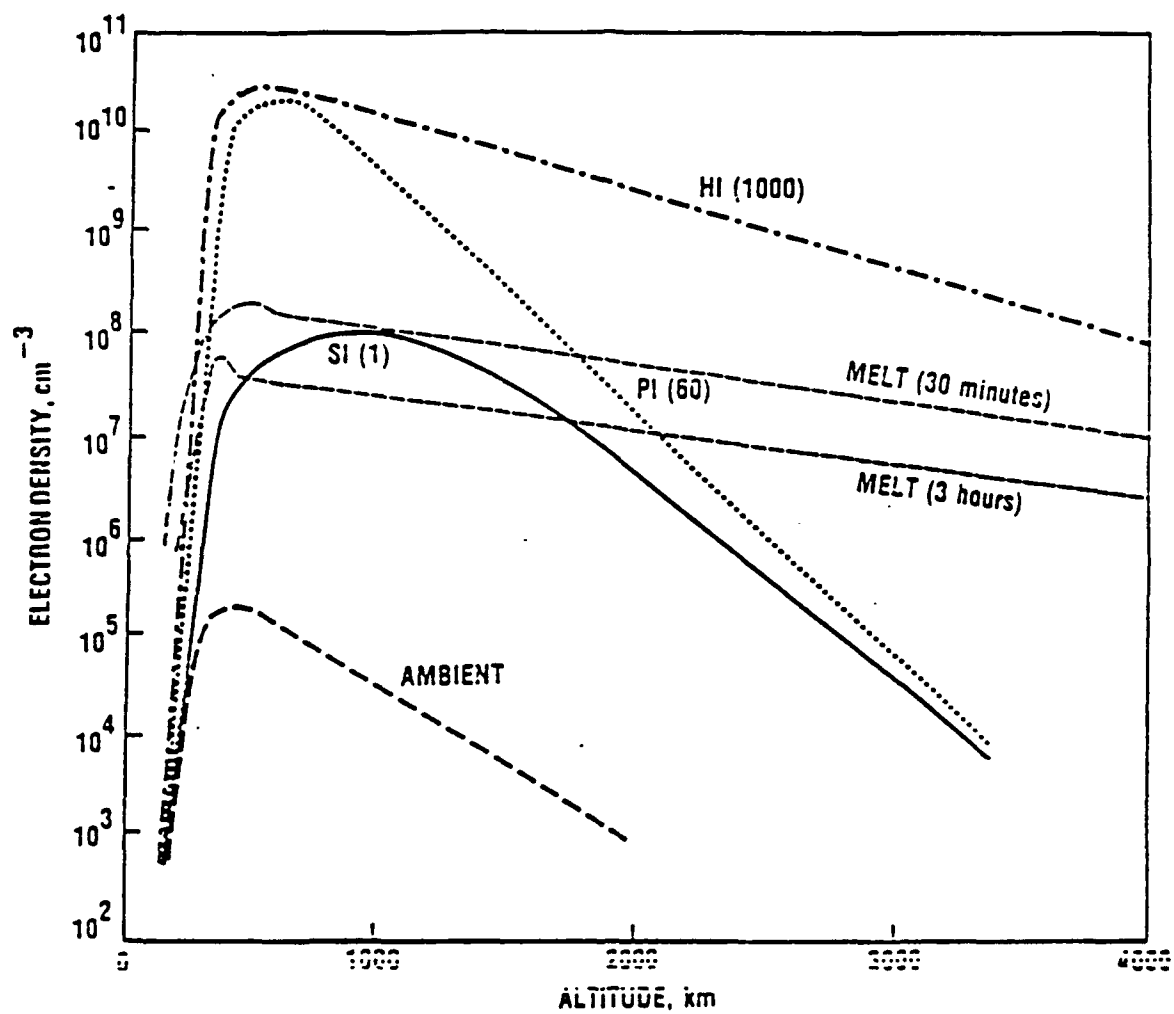
Figures 6.9c and 6.9e show the ionization in a highly nuclear disturbed (multi-burst) environment. If one sketches the mean ionization as a function of altitude under different conditions, one obtains the schematic results of Fig. 6.12, which shows the following as a function of altitude:

- Ambient ionization under representative mid-latitude conditions
- I(1) corresponds to the enhanced ionization due to a 1-Mt burst at 150-km altitude (from Keskinen and Fedder, 1988, from Hain et al., 1985).
- P(60) goes up the plume shown in Fig. 6.9c following the designated 60-burst laydown.
- H(1000) represents the total heaved environment of Fig. 6.9e following the designated 1000-burst laydown.
- We also show the results of a single burst MELT code run (from White et al, 1987b)--1 MT at 200 km--respectively at 30 minutes and 3 hours after the burst, which should be compared with the single-burst curve SI(1), both to indicate possible variabilities of different predictions and to remind the reader that the enhanced high-altitude ionization disappears very slowly.

⁵⁴ The notation for communication frequency bands is as follows: HF is 3-30 MHz; VHF is 30-300 MHz; UHF is 300-3000 MHz (3 GHz); SHF is 3-30 GHz; EHF is 30-300 GHz. For radar, L-band is 1-2 GHz; S-band is 2-4 GHz; C-band is 4-8 GHz; X-band is 8-12.5 GHz; K_u-band is 12.5-18 GHz; K-band is 18-26.5 GHz; and K_a-band is 26.5-40 GHz.

Table 6.6. Propagation Disturbances in a Structured Ionized Medium
(from Bogusch and Giugliano, 1982)

Propagation Disturbance	Effect on Propagated Signal	Effects on System Operation
Absorption	Loss of RF energy due to electron-ion and electron-neutral collisions in ionized regions causing signal attenuation.	Reduction in SNR below demodulation threshold causing data errors and possible loss of tracking functions.
Noise	Random RF energy emission from hot, ionized fireball regions.	Increased background noise levels causing reduction in SNR, increased data errors and track errors.
Phase and Doppler shift	Signal phase variation due to TEC (= Total Electron Content) changes along propagation path.	Possible loss of phase/frequency lock, and difficulty in carrier acquisition and tracking.
Time delay	Signal time-of-arrival variation due to changes in TEC along propagation path.	Possible loss of timing lock and difficulty in bit synchronization and tracking.
Dispersion	Signal energy/time dispersion due to spectral components propagating at different velocities in ionized regions.	Signal waveform distortion causing degraded demodulation and possibly inter-symbol interference at high data rates.
Faraday rotation	Rotation of signal plane of polarization due to increased magneto-ionic effects.	Severe amplitude fading with linear polarization; no effect with circular polarization.
Amplitude scintillation	Random fluctuations in signal amplitude due to scattering of signal energy by ionization irregularity structure.	Severe amplitude fading below demodulation threshold causing increased data error rates and possible loss of track.
Phase scintillation	Random fluctuations of signal phase and Doppler due to TEC variations and scattering of signal energy by ionization irregularity structure.	Possible loss of phase lock and loss of signal coherence leading to possible catastrophic demodulation failure.
Angular scattering	Random fluctuations of signal angle-of-arrival due to scattering of signal energy by ionization irregularities.	Reduction of SNR due to scattering loss in large antennas causing increased data and tracking errors.
Time delay jitter	Random fluctuations and dispersion of signal time delay due to TEC variation and frequency selective scattering.	Signal waveform distortion and timing jitter causing degraded demodulation and PN tracking, and possibly severe intersymbol interference at high data rates.



7-23-88-12

Figure 6.12. Enhanced Ionization due to Single and Multiple Nuclear Explosions as Function of Altitude

Note that:

- (i) The normal ionization shows a significant amount of variability in both mean level and in both spatial and temporal structure.
- (ii) A single, high-altitude nuclear burst produces several orders of magnitude in enhancement of mean ionization and also enhanced structure.
- (iii) In a multi-burst situation there is approximate saturation, with maximum mean ionization in the range of 10^{10} - 10^{11} electrons/cm³. This probably occurs for some tens of (appropriately located) bursts: the physical reason is that the first ionization potential of an air atom or molecule is 12-15 eV, while the second ionization potential is ~ 35 eV (cf Part I of these Notes, Chapter 2), so that as the air is heated there will generally be no more than one free electron per air atom or molecule. Reference to Fig. 6.10b shows that on account of heating the peak total number density is ~ 10^{11} /cm³, which leads to a comparable saturation value for the electron density.

6.4.2.3 Some Design Parameters for EHF Propagation in a Structured Ionized Medium

To provide a feeling for the magnitude of propagation effects, in Table 6.7 we show some propagation parameters for a 1000-km path in a medium of mean ionization 10^{10} electrons/cm³⁵⁵ and also with large fluctuations of RMS value $\Delta n_e^2 = 2.5 \times 10^{19}$ (electrons/cm³)². The results are obtained from the DNA/Wittwer code SIMPRP, version 2. We show the following parameters, as functions of signal frequency:

- Attenuation A (dB)
- Antenna noise temperature T_A (K)
- Signal decorrelation time τ_0 which corresponds to the average time fluctuation in signal strength
- Frequency-selective bandwidth f_0 which measures the frequency separation at which the fading histories of two different frequency components begin to become decorrelated from one another.

⁵⁵ At this electron density the plasma frequency f_p is 0.9 GHz.

Table 6.7A gives propagation results as a function of frequency, while Table 6.7B gives more results from SIMPRP for different values of ionization density and path length at a single frequency (60 GHz) to indicate the nature of the parametric variabilities.⁵⁶

Table 6.7. Electromagnetic Propagation Parameters in a Structured Ionized Medium

A. Frequency Dependence for 1000-km Path with $n_e = 10^{10} \text{ cm}^{-3}$					
f (GHz)	1	10	20	40	60
A (dB)	6.1E3	49	11.3	2.6	1.1
T_A (K)	10,000*	10,000	9300	4500	2200
τ_o (sec)	1.9 E-5	1.9 E-4	3.8 E-4	7.6 E-4	1.1 E-3
f_o (Hz)	1.1	1.1 E4	1.8 E5	2.8 E6	1.4 E7
B. Propagation at 60 GHz as Path Length and Electron Density are Varied					
Electron density (cm^{-3})	10^{10}	10^{10}	10^{11}	10^{11}	
Layer thickness (km)	500	1000	500	10000	
A (dB)	0.547	1.09	54.7	109	
T_A (K)	1200	2220	10,000	10,000	
τ_o (sec)	1.6 E-3	1.15 E-3	1.6 E-4	1.15 E-4	
f_o (Hz)	2.7 E7	1.4E7	2.7 E5	21.4 E5	

* 10,000 is default value for antenna temperature.

⁵⁶ The code can vary a number of parameters such as geomagnetic field, effective antenna size and shape, etc. Here we use the "default" values; typically there can be a variability of order 2 for many of the parameter choices.

6.4.3 Redout: Backgrounds for IR Sensors

The IR signature of high-altitude nuclear explosions has been studied for many years, beginning some eight years *after* the last U.S. Atmospheric Nuclear tests, as cryogenically cooled solid-state LWIR detectors became available.⁵⁷

The presently accepted physics is intricate:

- *In the normal atmosphere*

(1) Most IR radiance is due to the molecular minor species NO, CO, CO₂, H₂O, and O₃ because the major molecular species N₂ and O₂ are homonuclear diatomic molecules and thus have no allowed IR dipole transitions.

(2) Peak volume mixing ratios⁵⁸ of these molecules in the 20-60 km altitude range are :

• CO ₂	3×10^{-4}
• O ₃	1×10^{-5}
• H ₂ O	5×10^{-6}
• NO + NO ₂	1×10^{-9}
• CO	"small"

(3) Triatomic molecules are generally photodissociated by solar UV radiation at altitudes above 80-100 km, so that the only important molecular radiating species is NO, which is formed (to a few percent) when air is heated above 2000-2500 K, and which then does not disappear but rather "freezes-in" as the air cools (see, e.g., Part I of these Notes, Section 2.5).

- *In the nuclear-disturbed atmosphere (above 40-60 km, where non-equilibrium chemistry is important):*

(4) At very early times when the temperature is high and the electron density is very large, plasma radiation⁵⁹ predominates.

⁵⁷ During the atmospheric nuclear test series there were hardly any measurements with sensitive detectors beyond about 3 μ m, because the present generation of IR sensors did not exist. Further, it was not clear to the scientific advisors what could be learned from IR measurements. [Jack Carpenter (Visidyne), private communication.] For a review of IR data during the tests see Reed et al., 1980.

⁵⁸ Defined in standard way as the ratio of the volume (not mass) of CO₂, etc., to the volume of air.

⁵⁹ Electron-ion and electron-neutral free-free, free-bound, and bound-bound radiation (see, e.g., Part I of these Notes, Section 3.6).

(5) This is particularly true at high altitudes (> 150 km) where there are few radiating air molecules. However, current calculations suggest that there is significant radiation above 150 km due to CO_2 and possibly other molecules that are heaved up, as well as due to NO produced in air that is heated above 2000 K. Thus the assumption that plasma radiation predominates over molecular radiation may not be generally correct.

(6) There will be some radiation from debris species, arising from the nuclear weapon and its carrier vehicle, but this is not thought generally to be very important (except possibly in particular spectral regions) because there is so very little of this material present in comparison to the heated air.

Figure 6.13 gives a representative model for the IR radiance from a 1 Mt explosion at 200 km as viewed by a limb-viewing sensor looking through the atmosphere at 85-km and 120-km tangent height (reference to Fig. 6.7 indicates that at 85-km tangent height one views the X-ray and beta-patches⁶⁰, while at 120 km one sees mainly the debris patch and the ionized and excited air). At high altitudes and early times (when the ionization is large) there is a strong continuum due to plasma radiation, while at late times (when the ionization is relatively weak) the band radiation due to NO (at 2.7 and 5.4 μm), due to CO_2 (at 2.8, 4.3, and 15 μm) and due to O_3 (at 9.6 μm) predominates.

Note that at 85 km there is relatively little nuclear enhancement (factor 10^3 versus 10^8 at 140 km) because little of the nuclear-induced excitation penetrates down as low as 85 km.

At later times and lower altitudes the atmospheric absorption due to CO_2 becomes important. Note that the time variation of the radiance is much greater at 120 km than at 85 km. I show these figures here to urge the reader to refer to current Defense Nuclear Agency (DNA) literature for the most current model predictions, bearing in mind that, in the absence of nuclear test data, the predictions are based almost entirely on computer modeling and analogy with auroral and other simulation experiments.

⁶⁰ Which are shown in Fig. 6.7 and discussed in Section 6.3.1.3.

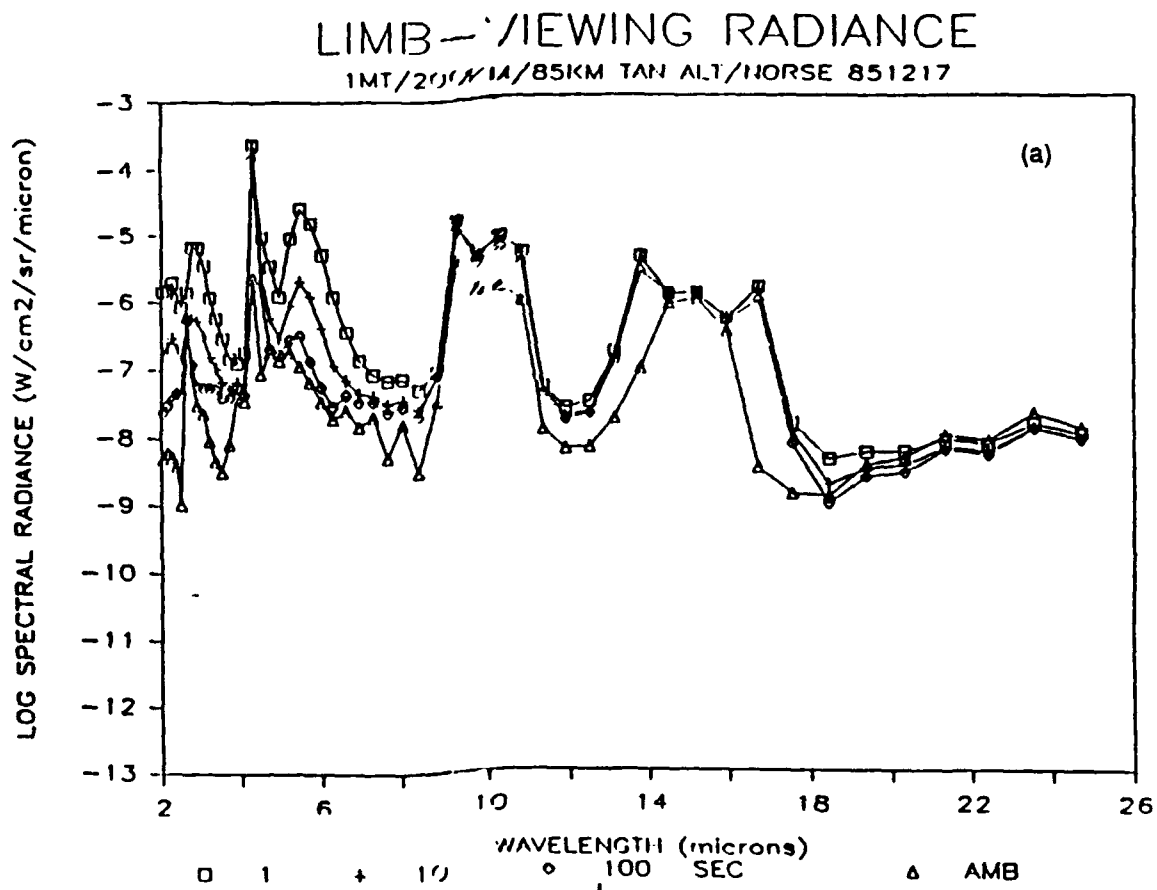


Figure 6.13. Limb-Viewing IR Radiance Following a 1-Mt Detonation at 200-km HOB. (a) 85-km Tangent Height, (b) 140-km Tangent Height.
[Source: NORSE Code--Stephens (1986)].

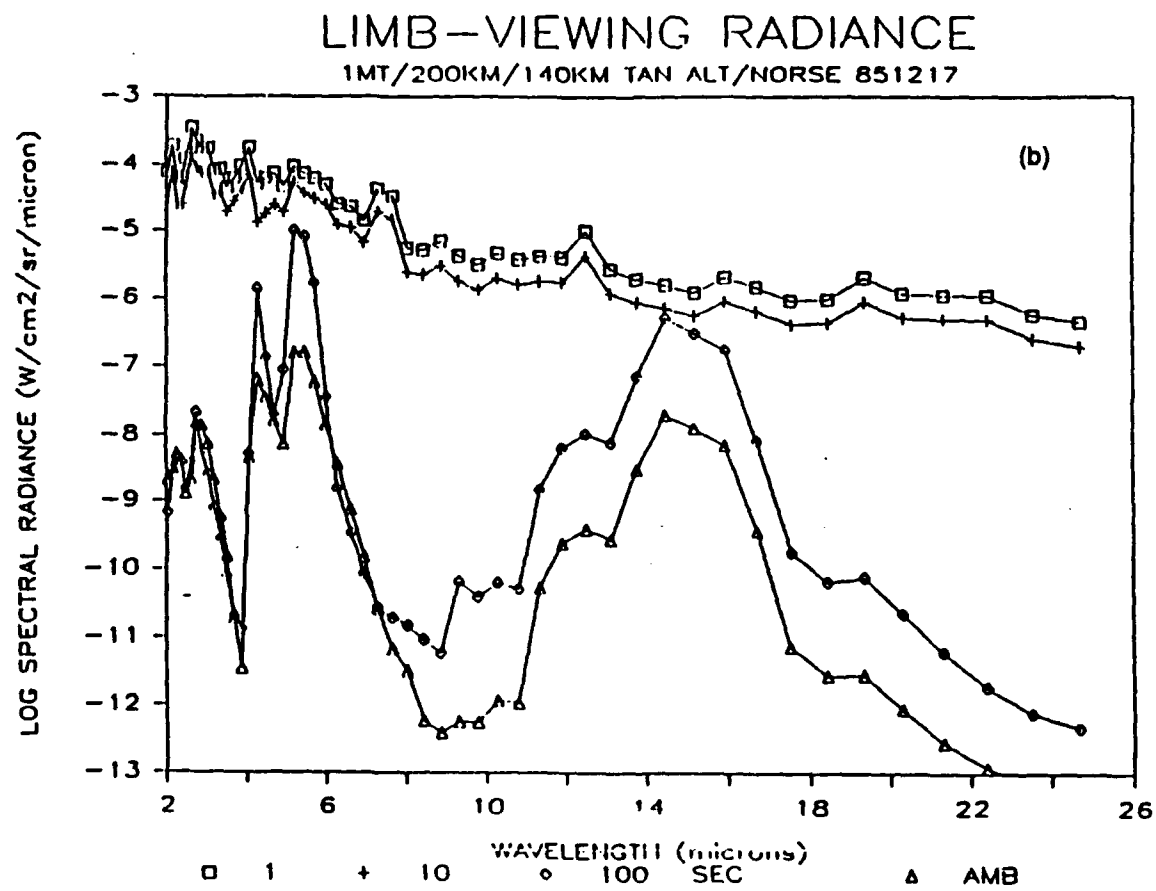


Fig. 6.13 (Continued)

6.5 QUALITY OF THE PREDICTIONS

This discussion emphasizes high-altitude backgrounds (ionization and infrared) for multiburst scenarios because this is the area of greatest uncertainty and importance for Strategic Defense applications. By contrast, for low-altitude nuclear explosions there is a relatively large amount of data and our understanding of the phenomenology and effects is relatively good (see ENW and EM-1 for results). Further, since fireballs are spatially confined at low altitudes because of the relatively high atmospheric density, for multiple bursts one simply superposes the single burst effects linearly at low altitudes.

At intermediate altitudes (30-90 km), non-equilibrium chemistry becomes very important. In the higher regions, where there is not a well-confined fireball because of the low ambient atmospheric density there is the possibility of multiburst IR signatures larger than at higher altitudes (Carpenter, 1989). Note that the data base is quite poor: there have been just three U.S. atmospheric nuclear explosions (indicated on Fig. 6.10) between 30- and 90-km burst height.

At high altitudes (> 90 km) the chemistry becomes simpler because there are relatively few chemically or radiatively interesting molecules,⁶¹ and again there is little data--just three well-instrumented and analyzed U.S. bursts (which are indicated in Fig. 6.10). At these high altitudes and correspondingly very low densities the bomb energy is distributed over very large regions of space, multiburst interactions will be important--and there are simply no data.

There is a particular problem in the infrared; while there are extensive radio/radar and visible optical data, and also data in the short-wave IR, there are essentially no observations beyond $3\text{-}5\text{ }\mu\text{m}$ ⁶². Thus, the predicted IR signatures come from computer simulations which are based on visible diagnostics during the 1962 and 1958 atmospheric test series.

Table 6.8 provides a tentative listing of the level of understanding of nuclear environment parameters, going from those instances in which the understanding is good

⁶¹ All molecules other than N_2 are essentially dissociated above 100 km; some 1-3% of nitric oxide (NO) is made when air is heated above 2500 K, and this tends to remain ("frozen-in") as the air cools. In addition, some air can be heaved up from below 100 km, so that there is the possibility of small amounts of the IR radiating species CO_2 and O_3 , as well as of CO produced by the dissociation of CO_2 (also smaller quantities of H_2O and OH from the 1-5 parts per million of H_2O).

⁶² See footnote 51.

(e.g., survivability, in particular X-ray hardness) to those cases where the understanding is poor (e.g., UV/VIS sensor operability).⁶³

Table 6.8. Levels of Understanding of Nuclear Environment

State of Knowledge	Examples	Effects of Uncertainty	
Good	Survivability:	X-ray hardness	Small
		β & γ Hardness	Small
Fair/Moderate	Communications:	Ionization	Moderate
		Structure	Can be large
Moderate/Poor	Sensor Operation:	Radar	See Comm
		IR	Mod/Large
		UV/VIS	Large?
		Structure	Can be large
Poor/Zero	(We could be missing some physics because there are no multiburst high-altitude data)		

In conclusion, the system architect and designer dealing with the nuclear-perturbed environment should recognize that he is faced with three independent sets of uncertainties, all of which may be quite large:

- (1) Uncertainties in weapon output for specified yield.
- (2) Uncertainties in threat scenarios.
- (3) Uncertainties in the nuclear effects codes.

⁶³ For a more extended discussion of these uncertainties, see Bauer, 1990b.

7.0 SOME TOPICS IN THE PROPAGATION OF ELECTROMAGNETIC RADIATION THROUGH THE ATMOSPHERE

7.1 INTRODUCTION

The propagation of electromagnetic radiation through the atmosphere is important for a variety of applications. Here we present the physics for a number of different situations. We begin by discussing the effects of molecular absorption, which is very strongly wavelength-dependent with transmission windows alternating with absorption bands. Figure 7.1 demonstrates the atmospheric transmittance through a 1 km (horizontal) path at heights $H_I = 0, 10 \text{ km}, 20 \text{ km},$ and 30 km , at wavelengths out to $5 \mu\text{m}$. Note the strong wavelength dependence and also how much better the transmittance becomes at the higher altitudes where the atmospheric density is lower, roughly by a factor 4 for each 10 km variation in altitude. The results shown here come from the USAF LOWTRAN and FASCODE computer models, which are appropriate, respectively, for low resolution (20 cm^{-1}) applications, and high resolution ($< 1 \text{ cm}^{-1}$), which is equivalent to a single spectral line and is thus appropriate for laser propagation and other applications calling for very high spectral resolution. Section 7.2 sketches the physics contained in the LOWTRAN and FASCODE atmospheric transmission codes--not how to run them. Section 7.3 discusses some characteristics of atmospheric aerosols, which are particles of dust and chemical pollutants as well as water or ice droplets. This section includes a discussion of the basics of atmospheric visibility and of Mie scattering calculations.

Clouds occur very frequently; optically thick clouds which block the transmission of visible or infrared radiation occur some 20-80 percent of the time, depending on location, altitude, season, and time of day. Table 7.1 gives mean values for high and total cloudiness for January and July at selected locations. Section 7.4 gives a very simple discussion of the physics of water/ice particle clouds. In Section 7.5 we discuss a very specific application, the analysis of Cloud-Free Lines of Sight (CFLOS).

For the propagation of High-Energy Laser Beams (or of other high-energy and/or high-resolution light beams) there is an additional series of problems. Section 7.6 treats

key characteristics of atmospheric turbulence which serves to broaden narrow beams, while Section 7.7 discusses some nonlinear processes related to the propagation of high-energy laser radiation, in particular thermal blooming and Stimulated Raman Scattering (SRS). The object of the present discussion is to present a very simple introduction to all these topics to enable the reader to go further on his own, starting with the reference material cited here.

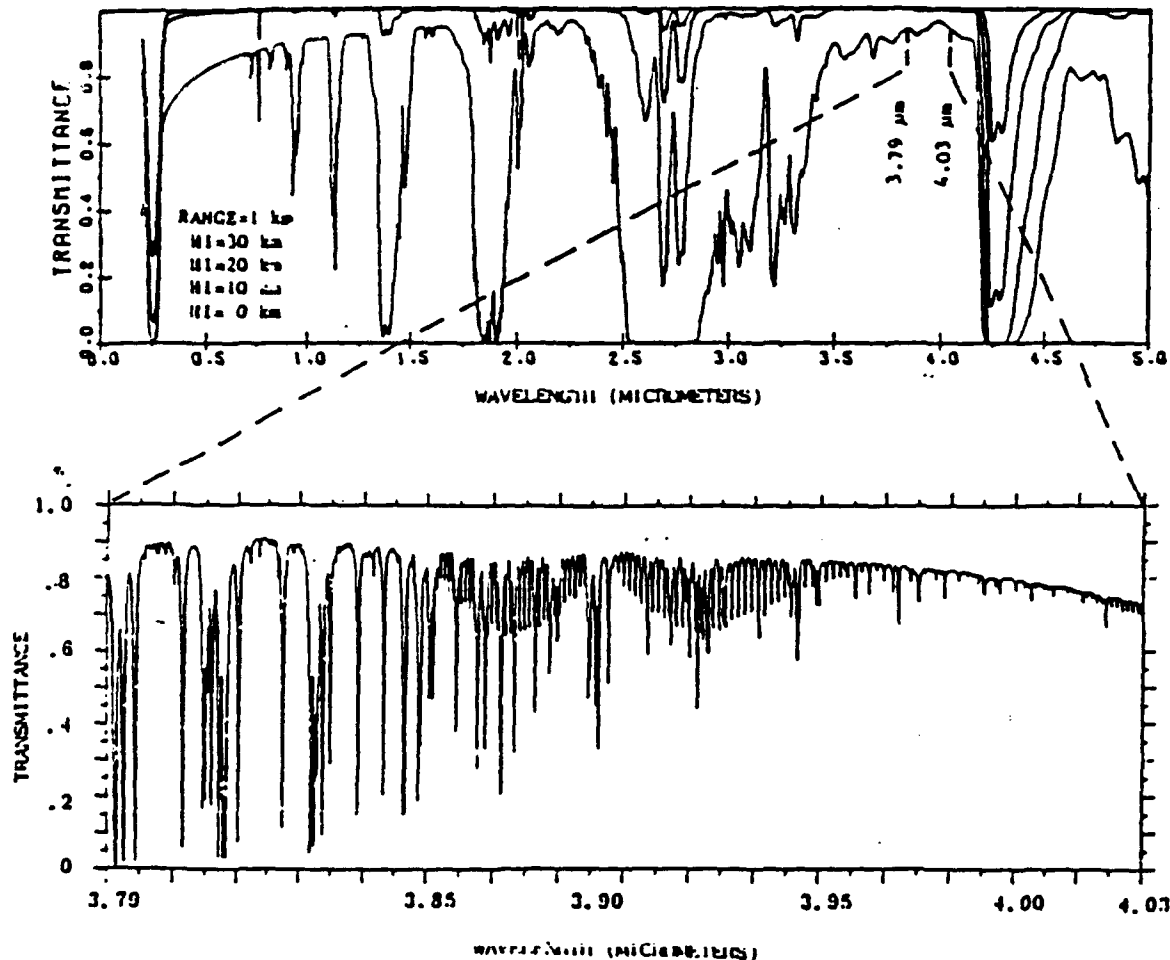


Figure 7.1. Atmospheric Transmittance Models: LOWTRAN and HITRAN (now FASCODE) Compared (Source: R.W. Fenn, AFGL, private communication, 1983)

Table 7.1. High and Total Cloudiness at Representative Locations in the Northern Hemisphere (Source: Mallick and Allen, 1978, 1979)

Location	Coordinates		High/Total Cloudiness	
	Longitude	Latitude	January	July
China Lake, CA	36°N	117°W	.17/.38	.12/.18
Grand Forks, ND	48°N	95°W	.39/.63	.31/.56
Maui, HI	21°N	156°W	.14/.40	.12/.50
Hudson Bay	60°N	88°W	.06/.36	.08/.29
N. Atlantic S	52°N	35°W	.24/.81	.13/.70
N. Atlantic N	62°N	30°W	.18/.76	.16/.72
Jan Mayen Is	71°N	10°W	.20/.81	.16/.85
Thule	76°N	68°W	.10/.35	.11/.73
Barrow, AK	71°N	156°W	.08/.34	.11/.64
Arabian Sea	8°N	65°E	.02/.23	.16/.55
Teheran	36°N	52°E	.14/.38	.02/.22
Ionian Sea	39°N	18°E	.07/.54	.01/.06
Moscow	56°N	39°E	.22/.61	.24/.46
Tyuratam	46°N	64°E	.16/.49	.13/.30
Lop Nor	40°N	91°E	.22/.48	.24/.57
Vladivostok	43°N	132°E	.11/.43	.22/.66
Japanese Trough	35°N	150°E	.16/.67	.12/.37
Anadyr	64°N	177°E	.28/.59	.21/.75
Murmansk	69°N	34°E	.22/.70	.16/.66
<p>Notes:</p> <p>a. High/total cloudiness means, for example, that at China Lake in January high clouds occur 0.17 of the time and total cloudiness occurs 0.38 of the time.</p> <p>b. These data come largely from downward viewing satellites such as NOAA-6 and DMSP, which tend to underreport optically thin clouds.</p> <p>c. Clouds are reported as present when at least 1/10 of the appropriate field of view is covered by clouds.</p> <p>d. High clouds are those above 7 km, with the altitude determined by the effective radiative temperature in the 10 to 12 μm infrared band as compared with the atmospheric temperature/altitude profile.</p> <p>e. High clouds are thus mainly moderately thick cirrus or cirro-stratus, plus some cumulonimbus (thunderclouds) at the lower latitudes ($\leq 30^\circ$).</p>				

7.2 TRANSMISSION THROUGH THE ATMOSPHERE: MOLECULAR ABSORPTION

7.2.1 Introduction

Transmission through the atmosphere is good in those spectral regions in which the molecular and atomic species present (which are listed, for instance, Table 2-1 of Part I) do not absorb (or emit, by Kirchoff's Law), the so-called "window regions", and bad where atmospheric species absorb. Atoms have electronic transitions, generally with excitation energies somewhat below the first ionization potential, which is generally in the range of 10-15 eV--see, e.g., Table 2-3 of Part I.⁶⁴ Molecules have electronic structure somewhat different from that of the atoms that make them up, but in addition they also have rotational and vibrational structure,⁶⁵ and they have dissociation energies in the range 1-10 eV--see, e.g., Table 2-3 of Part I.

Table 7-2 characterizes the different spectral ranges in terms of the energy of the transitions and in terms of the dominant transitions that are responsible for absorption in them. We specify wavelengths in nm ($1 \text{ nm} = 10^{-9} \text{ m}$), and μm ($1 \mu\text{m} = 10^{-6} \text{ m}$),⁶⁶ and energies in eV; for quantitative work it is customary to use energies in cm^{-1} ($1 \text{ eV} = 8067 \text{ cm}^{-1}$) instead of these two sets of units. The labeling of the spectral ranges is generic and not precise:

- The eye is sensitive to wavelengths in the Visible spectral range, 400-700 nm, and (not coincidentally) much of the solar irradiance is in this spectral range.
- Shorter wavelengths are called Ultraviolet (UV), which is sometimes divided into several regions:
- EUV, $\lambda < 100 \text{ nm}$, is actually not of great interest at present.

⁶⁴ But note that in general there are also much higher excited states, since an atom such as O with eight electrons has an ionization potential of 0.53 keV for the most strongly bound electron, as compared with the first ionization potential of 13.6 eV, and furthermore multiplets such as the $\text{O}(^3\text{P})$ ground state has transitions of much lower energy ($\sim .02 \text{ eV}$) between the three levels of the triplet.

⁶⁵ For a rotational quantum number J (defined in Part I, especially Appendices A and B), the energy is $hcB_e J(J+1)$; for O_2 , $J = 1$, this is 2.89 cm^{-1} or $.00036 \text{ eV}$. For vibrational quantum number v , the vibrational energy is $hc\omega_e(v+1/2)$; for O_2 , $v=1$ this is 2370 cm^{-1} or 0.29 eV .

⁶⁶ Note that wavelengths are often measured in $\text{\AA} = 10^{-8} \text{ cm} = 0.1 \text{ nm}$ - see, e.g., Fig. 3-6, p. 3-31.

- Far UV, $100 \text{ nm} < \lambda < 200 \text{ nm}$ includes some wavelengths where the atmosphere absorbs very strongly; the O_2 molecule has the very strong "Schumann-Runge" absorption in the 130-180 nm spectral range.
- Mid UV (MUV) is sometimes defined as $200 \text{ nm} < \lambda < 300 \text{ nm}$; ozone O_3 is a very strong absorber in the 230 - 270 nm spectral range.
- Near UV (NUV) may be defined as $300 \text{ nm} < \lambda < 400 \text{ nm}$.
- The division of the infrared (IR) is sometimes made into near IR or photographic IR; some special photographic films are sensitive out to $\sim 1000 \text{ nm}$ or $1 \mu\text{m}$. The SWIR ("short wavelength IR") corresponds to wavelengths less than about $3 \mu\text{m}$, the MWIR ("mid-wave IR") is traditionally taken as $3 \mu\text{m} < \lambda \leq 8 \mu\text{m}$, while the LWIR ("long wavelength IR") corresponds to wavelengths above $8\text{-}10 \mu\text{m}$.
- Beyond $\lambda = 100 \mu\text{m} = 0.1 \text{ mm}$ we enter the Millimeter Wave Region which is not discussed here--see, e.g., Kulpa and Brown, 1979.

Table 7-2. Listing of Different Spectral Regions

Name	Wavelength range(nm)	Energy range $hc/\lambda(\text{eV})$	Absorption mainly due to:
EUV	< 100	> 12.4	
FUV	100-200	12.4-6.2	electronic transitions (atomic)
MUV	200-300	6.2-4.13	electronic transitions (molecular)
NUV	300-400	4.13-3.1	electronic transitions (molecular)
VIS	400-700	3.1-1.8	a few molecular electronic transitions
NIR	700-1000	1.8-1.24	a few molecular electronic transitions
SWIR	$1\text{-}3 \mu\text{m}$	1.24-0.41	molecular vibrational transitions
MWIR	$3\text{-}8 \mu\text{m}$	0.41-0.155	molecular vibrational transitions
LWIR	$8\text{-}25+ \mu\text{m}$	$< 0.155 \text{ eV}$	vibrational transitions: H_2O rotation

7.2.2 The Nature of the Problem

Some excellent photographs of molecular electronic band spectra are given in Herzberg, *Spectra of Diatomic Molecules*, 1950, Ch. II. They show a great richness of phenomena, with continua as well as both coarse and fine spectral structure. The coarse,

banded structure ($\sim 10^2 \text{ cm}^{-1}$ to 10^4 cm^{-1} in total energy width) is due to molecular vibrations, while the fine structure due to molecular rotational lines has lines spaced 10^{-1} - 10^2 cm^{-1} apart. In general, the vibrational structure has sharp edges on one side with a gradual falloff on the back side (either toward higher or lower frequency). A typical electronic band system covers perhaps $10,000 \text{ cm}^{-1}$ to $20,000 \text{ cm}^{-1}$ ($\sim 100 \text{ nm}$ in visible), so that it may have $\sim 10^4$ individual lines, of varying spacing and strength. From the discussion of Section 3.4 of Part I of these Notes, we see that in the lower atmosphere (below 10 to 40 km) most spectral lines are collision broadened with a typical line width $\sim 0.1 \text{ cm}^{-1}$, although at higher altitudes Doppler broadening predominates (see Goody and Yung, 1989, p. 97f).

In the IR there are molecular vibration-rotation bands due to molecules such as NO, CO, CO₂, H₂O, O₃, etc. The radiating species are typically optically active molecules present in much smaller concentrations than the major species N₂ and O₂ which have such high molecular symmetry that they are not important radiators. Which species are important radiators depends strongly on the spectral region and temperature range.

The applications considered determine how the band structure should be treated. If one asks for the emission from high-temperature gases at low spectral resolution, very little detail is necessary. In particular, for an optically thin situation in which self-absorption and scattering are unimportant, the total integrated intensity is all that matters, and thus a Planck-type mean [see Eq. (3.23) of Section 3.3.3 of Part I] is adequate. Thus the description in terms of electronic system f-numbers with vibrational structure analyzed in terms of a Franck-Condon factor is satisfactory for determining the total radiation from air or combustion products at high temperatures.

However, if one asks for the atmospheric transmittance through 1- to 10-km path lengths (or through the whole atmosphere in vertical viewing), especially at high spectral resolution in the IR, where there are numerous absorption regions alternating with "windows," much more detail is needed. In particular, when one views not a gray⁶⁷ body through a long atmospheric path but rather a rocket plume or other array of hot CO, CO₂, and H₂O molecules viewed through the atmosphere containing cold H₂O and CO₂ molecules (see, for instance, Section 4.5.1 and Fig. 4.6 in Ch. IV of Part I), or for laser transmission at very high spectral resolution, very much detail is needed.

⁶⁷ A grey body is defined as one having an emissivity ϵ different from one, but not varying with wavelength λ . Thus a black body is the limit of a grey body having $\epsilon = 1$.

During the 1950s and 1960s a variety of very sensitive solid-state detectors of IR radiation as developed, and thus many specific questions regarding atmospheric transmission arose; and with the increase in computer power during this time frame a number of *Band Models* were devised and tested against experiment. These models tend to assume spectral lines of either equal or random spacing, of uniform or varying strength, sometimes with a configuration like the "Q-Branch" of a band (see, e.g., Herzberg, 1950, p. 48). Two limits are the *weak-* and *strong-line approximations*. In the weak-line limit the line is optically thin even at the line center, so that the emission (or absorption) is proportional to the number of molecules in the path [$A_{av} \sim (nfd)^{68}$]. By contrast, in the strong-line limit the line is optically thick at the center, so that increasing the number of molecules in the path simply increases the emission (or absorption) in the line wings, and of course this is different, depending on the line shape (Doppler, Lorentz, or Voigt--see, e.g., Fig. 3.5); the strong-line approximation traditionally corresponds to the Lorentz-line limit $A_{av} \sim (nfd)^{1/2}$.⁶⁹ For a review of band models, see, e.g., Goody & Yung, 1989, Ludwig et al., 1973.

During the 1970s the LOWTRAN transmittance computer code was developed at the U.S. Air Force Geophysical Laboratory (AFGL) for automating low-resolution IR transmittance calculations.⁷⁰ It was originally meant to apply to the lower atmosphere, as an empirical model of transmittance through perhaps a 1- to 10-km horizontal atmospheric path at altitudes up to 10-15 km, with Lorentz-broadened atomic spectral lines.⁷¹ As more sophisticated and detailed questions were asked simultaneously with a continued rapid growth in available computing power, line-by-line calculations became feasible and so the FASCODE computer program was developed at AFGL, based on an Atlas of Spectral Lines (the latest version of which is referenced by Rothman et al., 1987). By now this Atlas contains some 300,000 individual lines, and in the IR line-by-line calculations can be

⁶⁸ A_{av} is the absorption coefficient averaged over the relevant spectral interval, n is the number of absorbing molecules per unit volume, f is the oscillator strength of the relevant transition, and d is the geometrical path length under consideration. See Eq. (3.38a) or branch QA of Fig. 3.5.

⁶⁹ cf. Eq. (3.38c), or branch QC in Fig. 3.5.

⁷⁰ This code, which uses a very simple empirical band-type model, was first developed as a graphical procedure--see McClatchey et al., 1970, or *IR Handbook*, 1985, p. 5-46ff, which was then automated for digital computation.

⁷¹ Thus, at high altitudes, where Voigt or Doppler broadening applies for most spectral lines rather than Lorentz broadening, one has to check to be sure that the LOWTRAN results are correct for the particular problem under consideration--see Section 7.2.5.

carried through with the FASCODE computer program. This could not have been considered 20 years ago.

The point is the following. In an optically thin medium, if there are n absorbers per unit volume, each having absorption cross section σ_{abs} , then for a path length d one can define a dimensionless optical thickness

$$X = n \sigma_{\text{abs}} d \quad (7.1)$$

and the transmittance τ would be

$$\tau = e^{-X} = e^{-n \sigma_{\text{abs}} d} \quad (7.2)$$

In the context of atmospheric transmittance, Eq.(7.2) is known as "Beer's Law".

However, for a high-temperature molecular gas such as air, the absorption coefficient as averaged over a "reasonable" spectral interval does not follow a simple exponential law, so that Beer's Law of Eq.(7.2) is generally not obeyed. This arises because in a designated spectral range⁷² the spectral absorption varies drastically with frequency, so that the signal saturates in some portions of the spectral range and not in others. It is here that the LOWTRAN and FASCODE computer codes (or something equivalent) must be used.

It must be stressed that while the LOWTRAN and FASCODE programs enable a wide variety of atmospheric transmittance and radiance calculations to be carried out, they are not appropriate for "all conceivable" calculations. Thus for a sophisticated application it is important to check to be sure that the computer program used is appropriate.⁷³

7.2.3 The LOWTRAN Code

This section should be read after Sections 3.4 and 3.5 of Part I of these Notes, where the concepts and terms used here are explained. This material is presented here (from McClatchey et al., 1970, and Kneizys et al., 1980) to explain to the user what is actually in the code. This code works with $\Delta\nu = 20 \text{ cm}^{-1}$ spectral resolution (although a

⁷² Such as may be characterized by a particular filter.

⁷³ One current example is the following. For the earth's surface-atmosphere radiation budget, molecular absorption in the LWIR contributes significantly. Kratz and Cess, 1988, have compared line-by-line, narrow-band and broad-band models for the 9.6 and 14 μm bands of ozone, and find that the Malkmus narrow-band model can provide a good fit to a line-by-line description, which is not the case for methane.

5 cm⁻¹ version exists). It is basically a transmittance code, although the radiance can also be provided.

- (1) For a path length ΔS one defines an average transmittance

$$\tau(\Delta\nu, \Delta\nu; \nu) = (1/\Delta\nu) \int \tau(\nu) \delta\nu \quad (7.3)$$

and in general--because Beer's Law does not hold--there exists no function $K(\nu)$ such that

$$\tau(\Delta\nu, \Delta\nu; \nu) = \exp[-K(\nu) \Delta S] \quad (7.4)$$

because of the various saturation effects.

- (2) The average transmittance factor $\tau(\Delta\nu, \Delta\nu; \nu)$ for a given path length ΔS (which will now be written just as τ) is written as the product of a number of components:

$$\tau = \tau(\text{Molecular}) \cdot \tau(\text{Continuum}) \cdot \tau(\text{Rayleigh}) \cdot \tau(\text{Aerosol}) \quad (7.5)$$

$\tau(\text{Aerosol})$ is discussed in Section 7.3.2; $\tau(\text{Rayleigh})$ (scattering by atmospheric molecules at short wavelengths) is treated in Section 7.3.4; $\tau(\text{Continuum})$ (due principally to N₂ and H₂O molecules) is discussed in the LOWTRAN documents (e.g., Kneizys et al., 1980), while $\tau(\text{Molecular})$ is broken up into contributions from H₂O, O₃ and UMG = Uniformly Mixed Gases (CO₂, N₂O, CH₄, CO, O₂, etc).

$$\tau(\text{Molecular}) = \tau(\text{H}_2\text{O}) \cdot \tau(\text{O}_3) \cdot \tau(\text{UMG}) \quad (7.6)$$

- (3) To evaluate $\tau(\text{Molecular})$ one defines an Equivalent Optical Depth

$$\text{EOD} = C_\nu \cdot \omega^* \cdot \Delta S \quad (7.7)$$

where C_ν is a spectral absorption coefficient (an empirical expression is used in the code, see, e.g., *IR Handbook*, 1985, Fig. 5-14, p. 5-56), ΔS is the path length, and ω^* is an equivalent density along the path, characterized at altitude z by pressure $P(z)$ and temperature $T(z)$.

$$\omega^* = [\omega(P(z)/P_0)(T_0/T(z))^{1/2}]^n \quad (7.8)$$

where ω = concentration of the absorber and P_0 , T_0 refer to STP. The exponent n has the value $n = 0$ for the weak-line limit and $n = 1$ for the strong-line limit (which have been explained in the discussion of band models above (Section 7.2.1)--see also Goody, 1964, p. 127f). The LOWTRAN Code uses

$n = 0.9$ for H_2O

0.75 for UMG

0.4 for O_3 ,

and the function $\tau(EOD)$ as used in LOWTRAN is shown in Fig. 7.2. Note that it is very different from the simple Beer's Law form $\exp(-EOD)$ because of the effects of spectral saturation. In particular, at large optical thickness the holes in absorption coefficient between the individual spectral lines are still frequently optically thin so that the transmittance decreases much less rapidly with EOD than does the simple form $\exp(-EOD)$. The latest version of LOWTRAN (7, Kneizys et al., 1988) extends out to the UV. The electronic band systems that are important in the visible and UV range are treated in terms of band models, like the vibrational band systems.

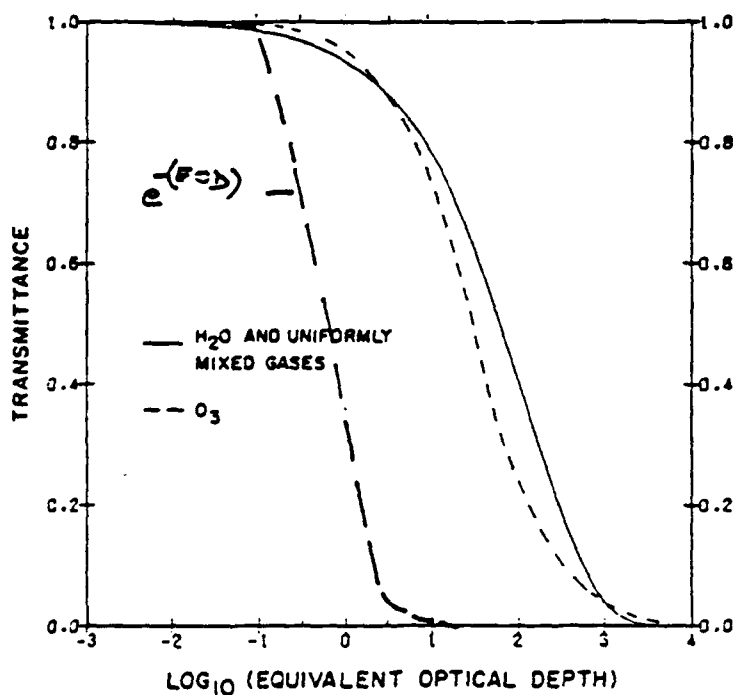


Figure 7.2. LOWTRAN Empirical Transmittance Function versus EOD
[$C_v \omega^* \Delta S$ of Eq. (7.5), from Kneizys et al., 1980],
as compared with the simple form $\exp(-EOD)$

7.2.4 FASCODE, a Line-by-Line Model

This code uses the same methodology for species concentrations and path geometry as does LOWTRAN, but the spectral information is treated differently, using the AFGL HITRAN Atlas of Spectral Lines (Rothman et al., 1987) which as of December 1987 contains some 300,000 lines of 28 different molecular species for wave numbers $\nu < 17,900 \text{ cm}^{-1}$ ($\lambda > 0.57 \text{ }\mu\text{m}$).⁷⁴ Where lines are available, the band systems are treated on a "Line-By-Line" basis using the full Voigt line shape. This applies mainly to the vibration-rotation band systems in the IR.

The current version is FASCODE 2, to be replaced in Summer 1990 by FASCODE-3; this goes out to $\nu < 50,000 \text{ cm}^{-1}$ ($0.2 \text{ }\mu\text{m}$), so that it contains also some electronic band systems which are treated by using band models the same as LOWTRAN.⁷⁵

At present LOWTRAN and FASCODE are coordinated so that species concentrations, geometry, aerosol models, continua, etc., are all treated similarly; the only difference is the treatment of molecular band systems for which lines exist in the AFGL line atlas. Figure 7.1 illustrates some different applications of these two codes.⁷⁶ LOWTRAN models apply to ambient atmospheric temperatures only, but FASCODE can in principle⁷⁷ treat such problems as the propagation of spectrally very narrow signals such as laser radiation through a designated region of the atmosphere, or the propagation of radiation from a rocket plume [which is largely hot (2000 K) H_2O and CO_2] through a long atmospheric path containing cold (250 K) air, including H_2O and CO_2 .

7.2.5 Atmospheric Transmittance/Radiance Above 50 km Altitude

The LOWTRAN/FASCODE series of models were originally designed for use below $\sim 10 \text{ km}$ altitude where the atmosphere is in local thermodynamic equilibrium and

⁷⁴ A 1990 HITRAN Tape is in course of preparation.

⁷⁵ See Clough et al., 1989; AFGL Users Manual for FASCODE-3 in preparation.

⁷⁶ Both codes can now be run on a PC-AT/286 or equivalent microcomputer; there is extensive documentation on how to run the code. Indeed, there are commercial versions for both LOWTRAN and FASCODE which can be run on personal computers.

⁷⁷ But note that the HITRAN atlas is intended for atmospheric applications, i.e., room temperature or below--say 600 K maximum. Accordingly, a high-temperature ($> 1000 \text{ K}$) gaseous source may have substantial contributions from spectral lines which are not contained in the HITRAN line atlas. Thus, FASCODE results may look reasonable but be incorrect. A new HITEMP line atlas is being prepared to supplement this deficiency for particular molecules in specific absorption bands. However, a very

where the assumption of Lorentz or collisional spectral line shape is generally good. At altitudes above 20-30 km both these assumptions tend to break down: as the density decreases, the spectral lines tend to be Doppler rather than Lorentz broadened⁷⁸ and the minor chemical species which are important optical radiators/absorbers are frequently not in Local Thermodynamic Equilibrium, so that they may be described as having different values for translational, rotational, vibrational and excitational/dissociative effective temperatures.

Thus at altitudes above 30-50 km one should consider both Doppler line shapes and the effects of NLTE (Non-Local Thermodynamic Equilibrium), rather than continue to apply LOWTRAN / FASCODE. One model which is currently becoming operational is the AFGL SHARC (= Strategic High Altitude Radiation Code), which calculates atmospheric radiation and transmittance for paths from 60 to 300 km altitude in the 2-40 μm spectral region. The initial version includes the five strongest IR radiators, NO, CO, H₂O, O₃, and CO₂ --see Sharma et al., 1989.

7.3 ATMOSPHERIC VISIBILITY AND AEROSOLS

7.3.1 Introduction: Visibility

In the visible spectral range, how far one can see is generally a function of the number density of small particles ("atmospheric aerosols") rather than of the gaseous air species, most of which are transparent in the visible.⁷⁹ If there are n particles per unit volume, each of mean extinction (= absorption + scattering) cross section σ , one defines the extinction coefficient k (length^{-1})

$$k = n \sigma \quad (7.9)$$

An effective visual range V_C is given by the "Koschmieder relation"

$$V_C = \ln(100/C)/n \sigma \quad (7.10)$$

large number of lines are needed in every particular spectral region with HITEMP, thus before attempting to use this code you should check to be sure the Atlas has been completed for this region.

⁷⁸ See Part I, Section 3.4: Doppler broadened lines have a gaussian profile which falls off rather rapidly away from the line center, by contrast to the slow ($1/\nu^2$) fall-off of Lorentz broadened lines, whose line wings can affect the absorption very far from the line centers.

⁷⁹ Note however that O₃ and NO₂, both of which are often present in small concentration in polluted air, do absorb in the visible.

where C is the (percent) contrast ratio

$$\text{contrast ratio} = [I(T+B) - I(B)] / [100 \times I(B)] , \quad (7.11)$$

at which the human observer can detect a target. Here $I(B)$ is the intensity of the background and $I(T+B)$ is the intensity of a target seen against the background. $C = 2$ to 5 (percent) are normal values for a human to perceive the target; traditionally, meteorological visibility is defined as V_2 for a contrast ratio of 2 percent so that $\ln(50) = 3.91$, but in fact an "average" observer will detect targets only at a contrast ratio of 5 percent or greater, so that $V_5 = \ln(20)/n\sigma = 3.00/n\sigma$, is a more representative visual range. Typical values of "good" visibility are in the range 10-100 km. For a discussion, see, e.g., List, 1951, p. 452f.

In Section 7.3.2 we discuss very briefly the different types of aerosols that occur in the atmosphere, while Section 7.3.3 discusses "Mie Scattering," i.e., expressions for the absorption and scattering cross section as a function of particle size, in particular of the Mie parameter

$$q = 2 \pi a / \lambda , \quad (7.12)$$

where a = particle radius and λ = wavelength of light, and of the complex refractive index of the medium, $m = N_1 - iN_2$. Section 7.3.4 discusses the particular problem of Rayleigh scattering by air molecules which is important in the near UV because if $q \ll 1$, the scattering cross section is proportional to q^4 .

For the problem of water droplets or ice crystals, there is additional physics due to the condensation and evaporation of the droplets. In this context it is customary to talk about clouds rather than aerosols; elements of cloud physics are discussed in Section 7.4.

7.3.2 Atmospheric Aerosols

Atmospheric aerosols are typically of 0.03 to 0.5 μm mean radius. They can be of quite different types, namely soot and other pollutants, mineral particles, water-soluble material such as sea salt, and biotic particles such as bacteria and fine plant debris, as well as water and ice particles. Table 7.3 gives values for the complex refractive index

$$m = N_1 - iN_2 \quad (7.13)$$

of some of these materials at different wavelengths; N_1 is the real part of the refractive index, while N_2 is the absorption coefficient. Note that water (and ice) absorbs very little in the visible while soot is a highly absorbing material at all wavelengths. Dust is

intermediate, and in general N_2 or the absorption coefficient increases with increasing wavelength in the IR. Figure 7.3 gives some typical values for the atmospheric extinction coefficient in the visible ($\lambda = 0.55 \mu\text{m}$) as function of altitude. Note that there is a great deal of extinction in the "Planetary Boundary Layer," roughly the lowest 1 km of the atmosphere, and a secondary maximum, the Junge Layer, in the 15 to 20 km altitude range. The Junge layer is largely of volcanic origin, is highly variable, and is made up mainly of $\text{H}_2\text{SO}_4/\text{H}_2\text{O}$ droplets of $\sim 1 \mu\text{m}$ mean size. For more information, see USAF, 1985, pp. 18-9ff.

Table 7.3. Complex Refractive Index $m = N_1 - i N_2$ for Different Materials.
(Source: USAF, 1985, pp. 18-16ff)

Wavelength	Water		Dust-Like		Soot	
(μm)	N_1	N_2	N_1	N_2	N_1	N_2
0.25	1.362	3.35E-8	1.530	3.00E-2	1.620	0.450
0.55	1.333	1.96E-9	1.530	8.00E-3	1.750	0.440
1.06	1.326	4.18E-6	1.520	8.00E-3	1.750	0.440
2.70	1.188	1.90E-2	1.180	1.30E-2	1.830	0.520
4.50	1.332	1.34E-2	1.260	1.40E-2	1.940	0.590
10.0	1.218	5.08E-2	1.750	0.162	2.210	0.720
20.0	1.480	0.393	1.680	0.220	2.450	0.850

7.3.3 Mie Scattering by Small (Spherical) Dielectric Particles⁸⁰

We examine the interaction of radiation of wavelength λ with spherical particles of radius a , and introduce the Mie parameter $q = 2\pi a/\lambda$ of Eq. (7.12). The particles are made up of a medium of complex refractive index $m = N_1 - i N_2$. The scattering cross section $\sigma(\text{sca})$ and the absorption cross section $\sigma(\text{abs})$ are expressible as functions of q and m ; it is possible to get useful results in a variety of limits that are presented here first. We also present the differential scattering cross section or angular distribution $P(\theta)$. We discuss three limits, first the "Rayleigh Limit" of small particles, $q = 2\pi a/\lambda \ll 1$, then the "Geometrical Optics" limit of large particles, $q \gg 1$, and then the limit of particles of various values of the size parameter q with refractive index close to one.

⁸⁰ The present results come mostly from Van de Hulst, 1957; they are presented here so that the reader can get a simple semi-quantitative model for scattering from small, spherical particles. The discussion emphasizes dielectric, i.e., scattering particles rather than particles (such as soot or metals) that are primarily absorptive.

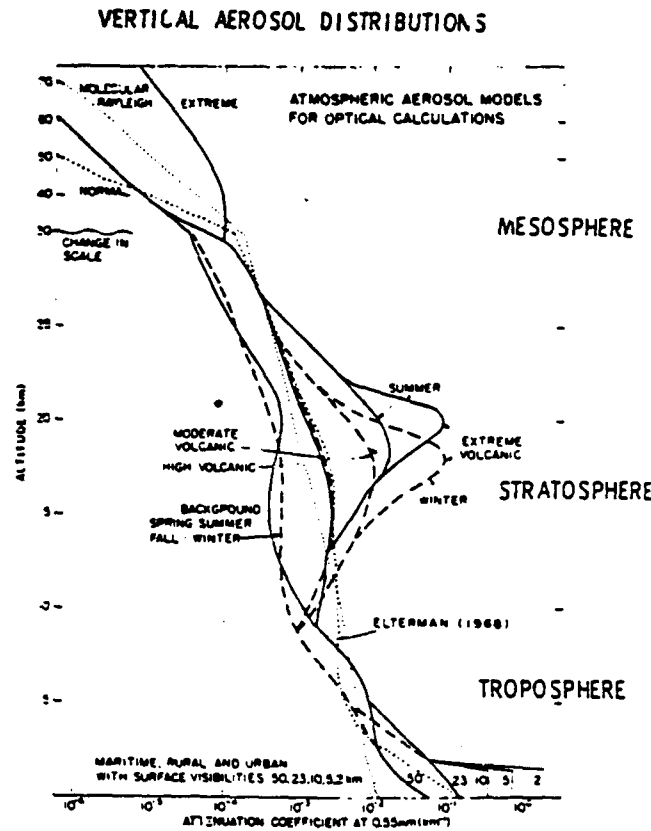


Figure 7.3. Representative Extinction Coefficients for Atmospheric Aerosols as Function of Altitude (USAF, 1985, p. 18-14)

7.3.3.1 Very Small Particles: $q \ll 1$ (Rayleigh Limit)

Here the scattering cross section is

$$\sigma(\text{sca})/\pi a^2 = (8/3)q^4 |(m^2 - 1)/(m^2 + 2)|^2, \quad (7.14)$$

and if m close to 1 and also N_2 small, so that there is very little absorption, Eq. (7.14) becomes

$$\sigma(\text{sca})/\pi a^2 = (32/27)q^4 (N_1 - 1)^2. \quad (7.15)$$

In this limit, provided m is close to 1, and $N_2/(N_1 - 1) \ll 1$ - we have

$$\sigma(\text{abs})/\pi a^2 = (8/3)q N_2. \quad (7.16)$$

Eq. (7.16) gives $\sigma(\text{abs}) \sim a^3$, so that in this limit the absorption cross section is proportional to the volume or mass of material. Thus, every individual atom or molecule contributes to absorption/emission if the particle is sufficiently small so that the outer molecules do not shield the inner ones. For large particles where this shielding is important, $\sigma(\text{abs}) \sim a^2$. Note that in the Rayleigh limit, $\sigma(\text{sca})/\pi a^2 \sim q^4$, so that there is very little scattering if $q \ll 1$.

7.3.3.2 Very Large Particles: $q \gg 1$ (Geometrical Optics Limit)

Here

$$\sigma(\text{sca})/\pi a^2 \Rightarrow 2 \text{ as } q \text{ becomes very large} \quad , \quad (7.17)$$

and

$$\sigma(\text{abs})/\pi a^2 \Rightarrow 1 \text{ as } N_2 q \text{ becomes very large} \quad . \quad (7.18)$$

The physical meaning of these two independent conditions is the following. The scattering cross section for large particles is twice the geometrical particle size because of diffraction or shadow scattering, while the absorption cross section can be as large as the geometrical particle size for the case in which all radiation falling on the particle is absorbed.⁸¹

For the case of m close to 1, and N_2 small, it is convenient to define

$$u = 2q |m-1| \sim 2q(N_2-1) \quad , \quad (7.19)$$

and now

$$\sigma(\text{sca})/\pi a^2 = 2 - (4/u) \sin u + (4/u^2) (1 - \cos u) \quad (7.20)$$

$$\sigma(\text{abs})/\pi a^2 = (8/3)qN_2 \quad . \quad (7.21)$$

7.3.3.3 Angular Distribution, $P(\theta)$ ⁸²

If $q \ll 1$, so that the particles are small compared to the wavelength of light, there is very little scattering because from Eq. (7.13) $\sigma(\text{sca}) \sim q^4$, and what scattering there is has the Rayleigh angular distribution

$$P(\theta) = (1 + \cos^2 \theta) \quad . \quad (7.20)$$

Here $P(0 \text{ deg}) = 2 = P(180 \text{ deg})$ and $P(90 \text{ deg}) = 1$, so that there is relatively little angular variation.

By contrast, if $q \gg 1$ (geometrical optics limit) and m is close to 1, there is little refraction and absorption, and most of the scattering is in a forward direction.⁸³ If $q > 1$,

⁸¹ For an example in which both limits (7.15) and (7.16) apply simultaneously, see, e.g., Van de Hulst, 1957, p. 181, Fig. 33.

⁸² We define $\theta = 0$ as forward scattering (i.e., direct transmission), and $\theta = 180 \text{ deg}$ as back scattering.

⁸³ As an example, note that a large glass bead (or cloud water droplet) does not scatter much incident radiation out of the direct beam, so that most of the radiation incident on the bead is transmitted, with just slight refraction.

different light rays going through the particle can have significant differences in optical path within the particle. These lead to interference between the different beams and thus the angular distribution has a series of maxima and minima--see, e.g., Fig. 7.4, which shows a polar plot of the scattering of linearly polarized light by a dielectric sphere of refractive index $N_1 = 1.25$. The quantities i_1 and i_2 correspond to orthogonal polarizations of scattered radiation. However, if instead of having a medium consisting of particles all of the same size as in Fig. 7.4, there is a smooth particle size distribution, then the violent fluctuations in angular distribution are smoothed out due to the distribution in particle sizes, and one gets the much smoother distribution shown in Fig. 7.5, which has actually been calculated for water droplets (cloud particles) at different wavelengths between visible and IR. Note that the shorter the wavelength, i.e., the larger the value of $q_a = 2\pi a_a/\lambda$, the more forward scattering, and the larger is the scattering cross section. (Here a_a and thus q_a refer to the average particle radius and thus average value of q). Thus for $\lambda = 20 \mu\text{m}$, we have $q_a = 1.26$, and the cross section approaches the Rayleigh form, although the ratio of forward to backward scattering cross section is still ~ 30 (versus 3000 for $\lambda = 2.7 \mu\text{m}$). At the shortest wavelengths there is some back (near- $\theta = 180$ deg) scattering.

Normally one cannot find a simple analytic fit to the various curves of Fig. 7.5, but the Henyey-Greenstein function

$$P_{HG}(\theta) = A (1 - g^2)/(1 + g^2 - 2g \cos\theta)^{3/2} \quad (7.23)$$

is frequently used for applications such as Monte Carlo calculations where a simple analytic form is needed. Here $g = (\cos\theta)_{av}$, and it and the scale factor A are chosen to fit the data. The Henyey-Greenstein function does not show the (small) enhanced back scattering shown in the visible in Fig. 7.5--that would require at least one more parameter.

7.3.4 Rayleigh Scattering by Air Molecules in the Visible and Near-UV

At wavelengths below about $0.4 \mu\text{m}$, atmospheric transmission is reduced due to scattering by air molecules which here behave like very small particles [with $q \ll 1$, so that $\sigma(\text{sca}) \sim 1/\lambda^4$ and is very small, from Eq. (7.15)]. This effect is responsible for the blue of the sky.⁸⁴ The effective extinction coefficient is

$$k_s(\lambda) = (2^9 \pi^2/3^3) (N_1 - 1)^2 n (\pi a_2)^3/\lambda^4, \quad (7.24)$$

⁸⁴ When we look away from the sun at the sky, we see scattered solar radiation. Because $\sigma(\text{sca}) \sim 1/\lambda^4$, there is much more short wavelength (blue) sunlight scattered than long wavelength (red) sunlight (by a factor $\sim 2^4 = 16$) and thus the sky looks blue.

where n = number of air molecules per unit volume, πa^2 = mean cross-sectional area of a particle, and N_1 is the real part of the mean refractive index of air, some typical values are

$$N_1 - 1 = 3.0 \times 10^{-4} \quad (0.25 \mu\text{m})$$

$$2.8 \times 10^{-4} \quad (0.5 \mu\text{m})$$

$$2.7 \times 10^{-4} \quad (2 \mu\text{m})$$

See USAF, 1985, p. 18-7 for more detail.

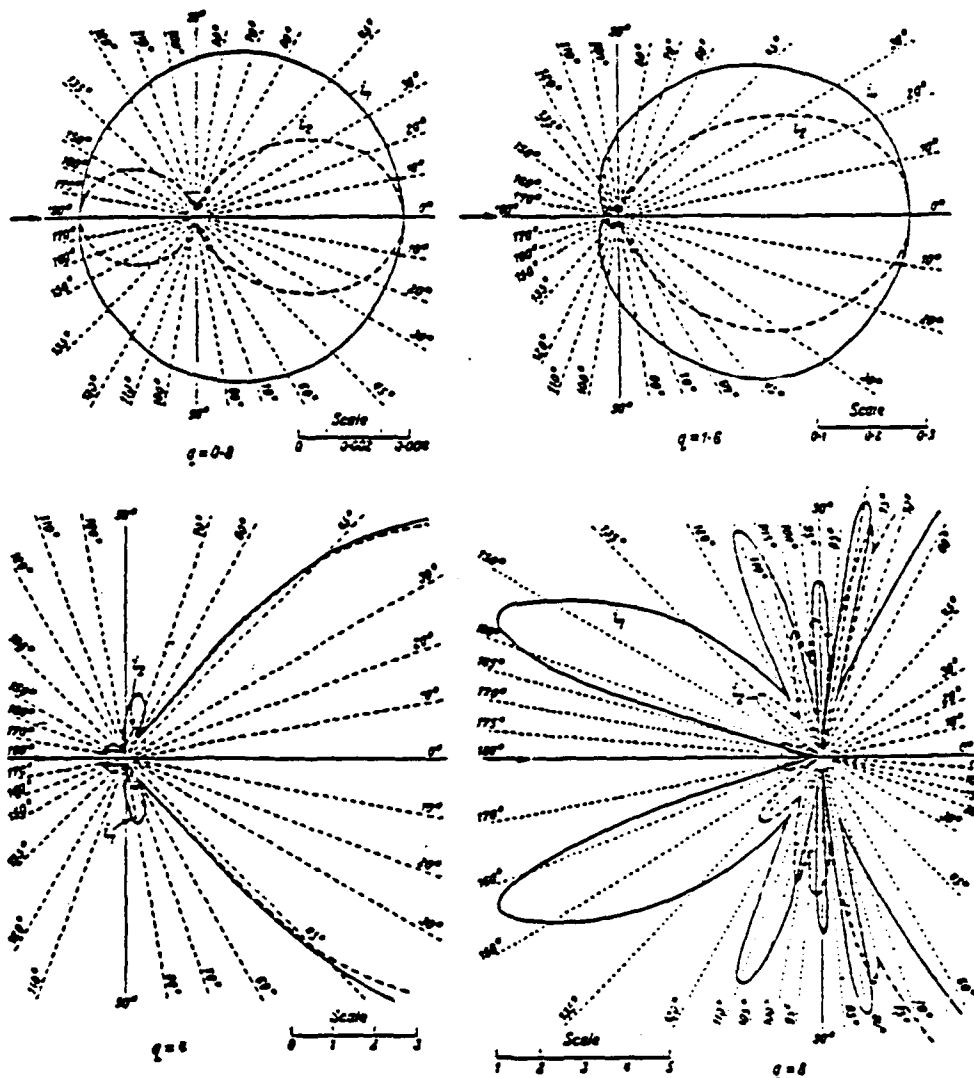


Figure 7.4. (Mie) Scattering by a Dielectric Sphere of Refractive Index $N_1 = 1.25$ at Different Wavelengths.
(after Blumer, 1925; $I_1 = q^2 I_{\text{parallel}}$; $I_2 = q^2 I_{\text{perp}}$)

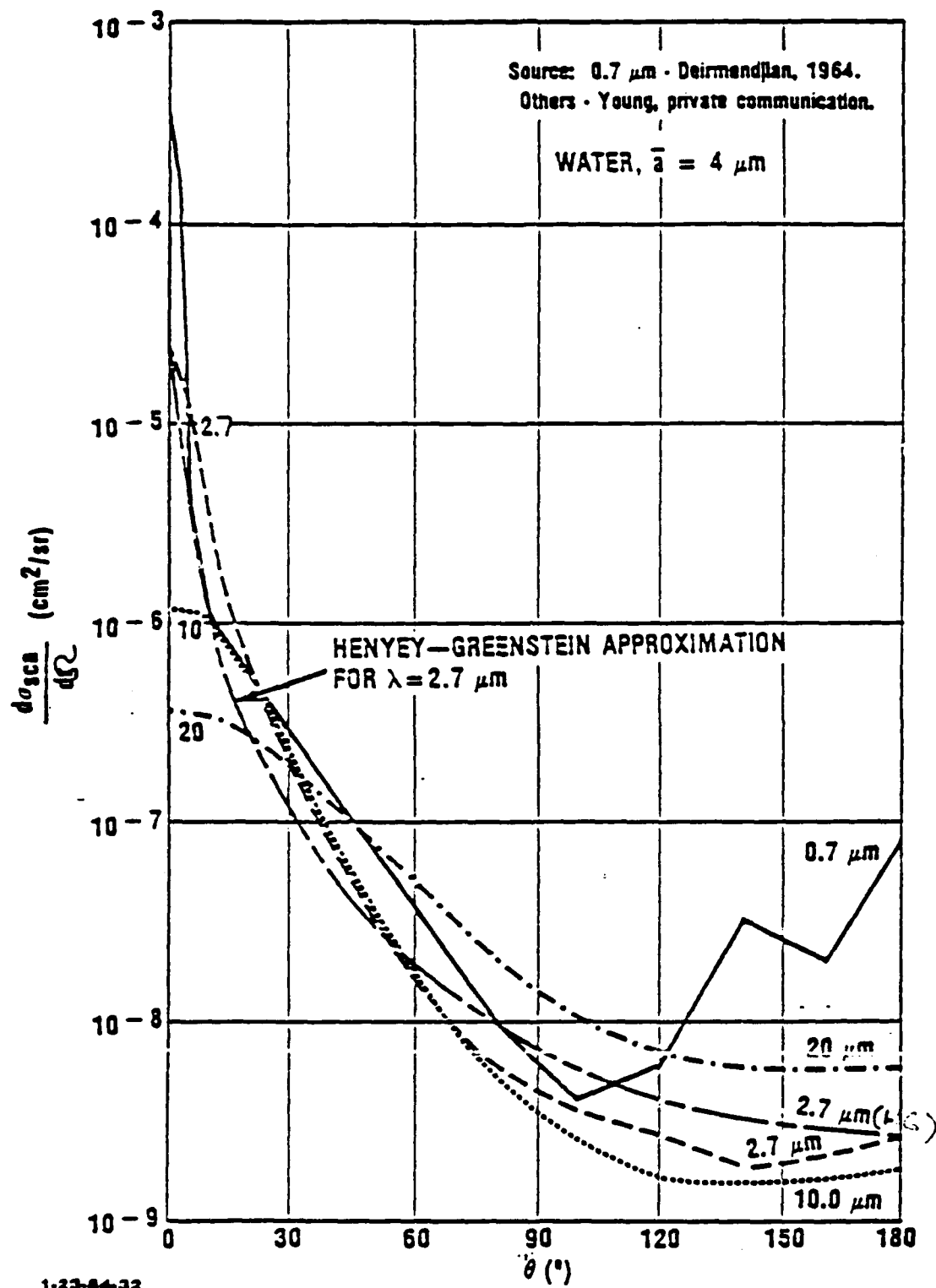


Figure 7.5. Scattering from Distributions of Water Droplets (of mean radius 4 μm) at Different Wavelengths. (Source: Bauer et al., 1984)

7.4 PHYSICS OF CLOUDS

The saturated vapor pressure (SVP) of water increases very strongly with increasing temperature, and at temperatures below freezing the SVP over ice is smaller than that over water--see Fig. 7.6. Thus, if we take an "air parcel" and cool it adiabatically (and without changing the water vapor mixing ratio), the relative humidity increases. If we cool the parcel further, eventually it saturates, and once the moisture content exceeds saturation at the parcel temperature, the excess of water condenses. Reference to Fig. 7.6 shows that at temperatures below 0°C the SVP over water is greater than that over ice, so that condensation over ice occurs at lower water vapor mixing ratios than over water. At air temperatures of 0°C to -20°C, condensation occurs either as water droplets or as ice crystals, but below -20°C ice generally predominates.

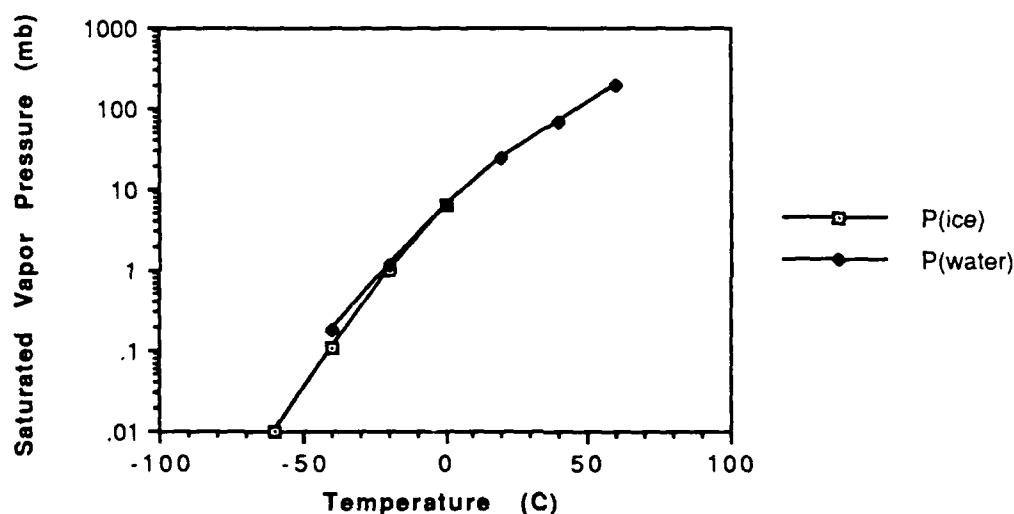


Figure 7.6. Saturated Vapor Pressure of Water Vapor Over Water and Over Ice as Function of Temperature (Source: List, 1951, p. 351f)

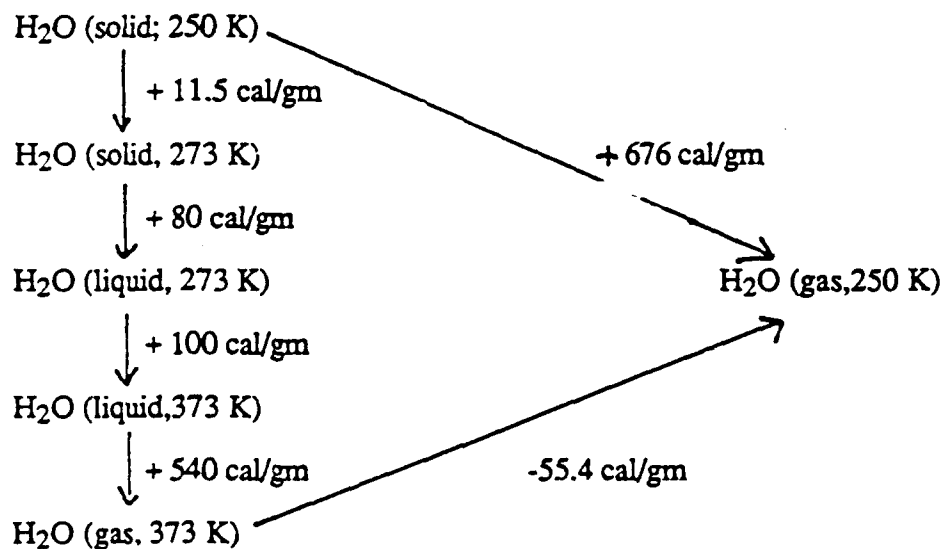
The latent heat of evaporation/condensation of water is of the order 2.8×10^6 Joule/kg--see Fig. 7.7--which is sufficiently large for the enthalpy of moist air (with a water vapor mixing ratio of order several times 10^{-3}) to be significantly larger than that of dry air.⁸⁵ Furthermore, the settling speed of small water droplets ($\sim 10 \mu\text{m}$ or less) shown in Fig. 7.8 is sufficiently small compared with vertical atmospheric convection

⁸⁵ This has considerable implications for the climatic difference between dry and moist regions, including such things as the day-night temperature difference which is much smaller over water than in a desert.

speeds, which are usually in the range 1-10 cm/sec, so that assemblies of air containing water droplets or ice crystals--i.e., clouds--are effectively (if not thermodynamically) stable.

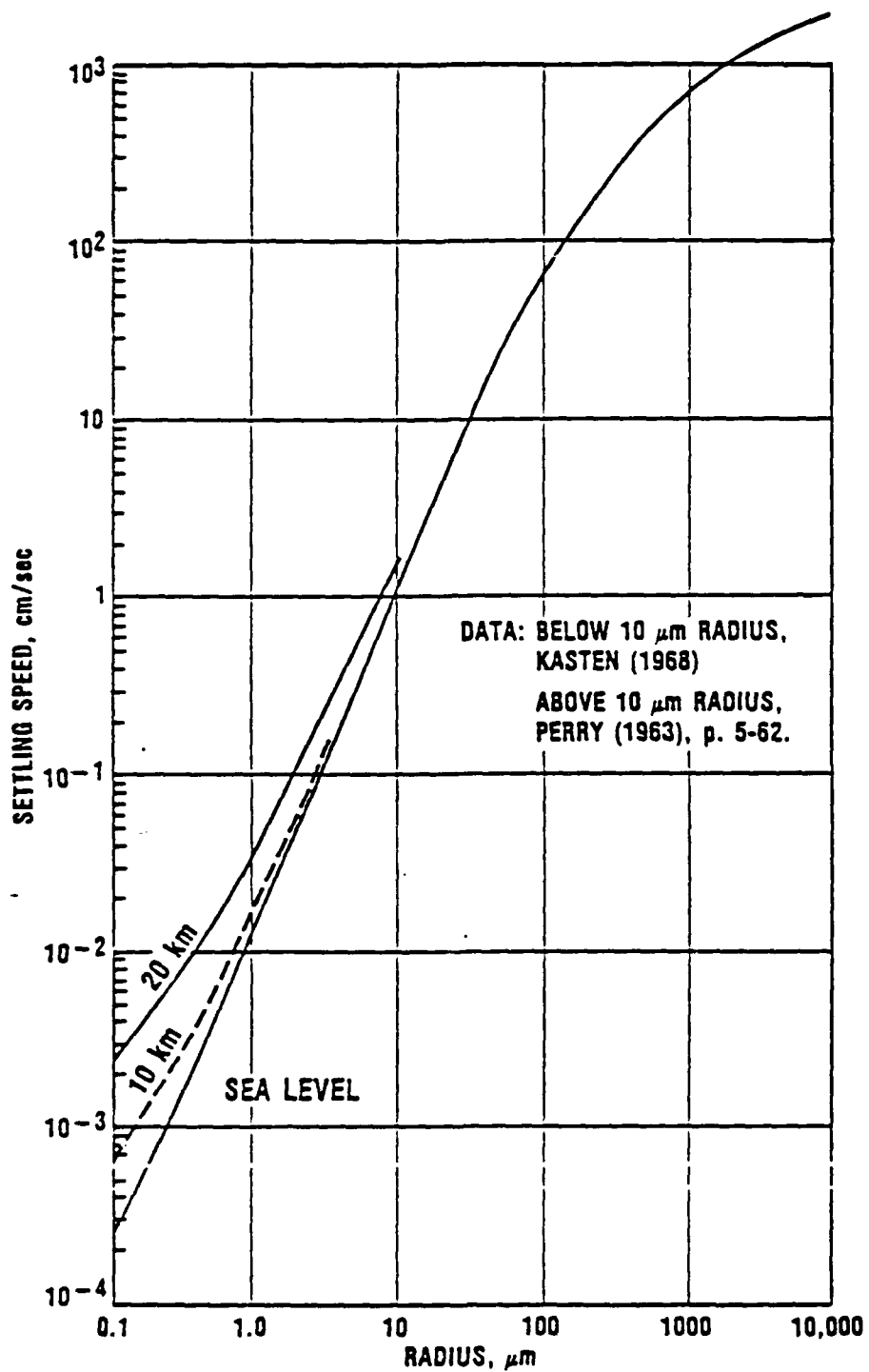
$$\begin{aligned}\text{Because } c_p(\text{ice}) &= 0.5 \text{ cal/gm K} \\ c_p(\text{water}) &= 1.0 \text{ cal/gm K} \\ c_p(\text{water vapor}) &= 0.45 \text{ cal/gm K}\end{aligned}$$

(cf: AIP Handbook, 2nd Ed., p.4-189; Hdbook of Chem. & Phys., 44th Ed., p.2436, Slater, Intro. to Chem. Physics, p.147) we have the following cycle:



Note that, because $c_p(\text{dry air}) = 0.24 \text{ cal/gm K}$, the enthalpy change corresponding to the evaporation of 1 gm ice is of the same order as the enthalpy required to raise the temperature of 1 kg dry air by 3 K.

Figure 7.7. Latent Heat of Evaporation/Condensation of Water



9-24-62-6

Figure 7.8. Sedimentation Speed of Water Droplets In the Atmosphere

Clouds are always produced by the adiabatic cooling of a (moist, warm) air mass. This process can take place under a variety of different conditions, and so it is appropriate to begin by identifying the concept of atmospheric stability. Figure 7.9 shows a generic atmospheric temperature profile which indicates three distinct altitude regions.

Below approximately 1 km there is the *Planetary Boundary Layer* (PBL),⁸⁶ a region in which the temperature-altitude profile changes dramatically between normal daytime and night time conditions. Above the PBL, and up to a temperature minimum near 11 km, is the *Free Troposphere*, a region in which the temperature normally decreases with height (although there may be additional temperature layers within this region). Above the temperature minimum near 11 km, the Tropopause, comes the *Stratosphere*, a region in which the temperature increases with height.

A region in which the temperature decreases strongly with increasing height is dynamically unstable in that if a parcel of air is displaced slightly from its initial position it moves further in the direction of its initial displacement, either up or down. The free troposphere is such an unstable region, and this is why convective or cumulus clouds are often found in this region. The night time PBL and the stratosphere are dynamically stable; thus generally there are no clouds in the stratosphere, and typically stable, layered clouds ("stratus") just at the inversion topping the PBL.

It can easily be shown that a parcel of air is stable if the vertical temperature gradient for an adiabatic displacement, $\partial T / \partial z|_{\text{adiab}}$, is sufficiently small:

$$\partial T / \partial z|_{\text{adiab}} < -g/c_p = \gamma_{\text{ad}} \quad (7.25)$$

where g = acceleration due to gravity and c_p = specific heat of air at constant pressure. Conversely, an air mass is unstable if

$$\partial T / \partial z|_{\text{adiab}} > \gamma_{\text{ad}} \quad (7.26)$$

⁸⁶ A good definition of the PBL (provided by R. Penndorf) is "a layer in which a noticeable influence of the earth's surface on wind occurs by friction. The upper boundary is determined by the altitude at which the wind vector is approximately equal to the geostrophic wind (i.e., the wind determined by the overall motion of the atmosphere). Within the PBL, the wind direction and speed are affected by friction near the ground in establishing a universal function, the "Ekman spiral." The upper boundary of the PBL is frequently, but not always, characterized by a temperature inversion. Clouds are generally missing in the PBL, but haze or mist may form. Only just below the upper boundary turbulent clouds may form. There is a lot of turbulence in the PBL due to heating of the ground, and adiabatic or even stronger temperature gradients may develop as a result of radiative processes involving the ground. If the temperature inversion at the top of the PBL is strong, it may block mixing of the air from above."

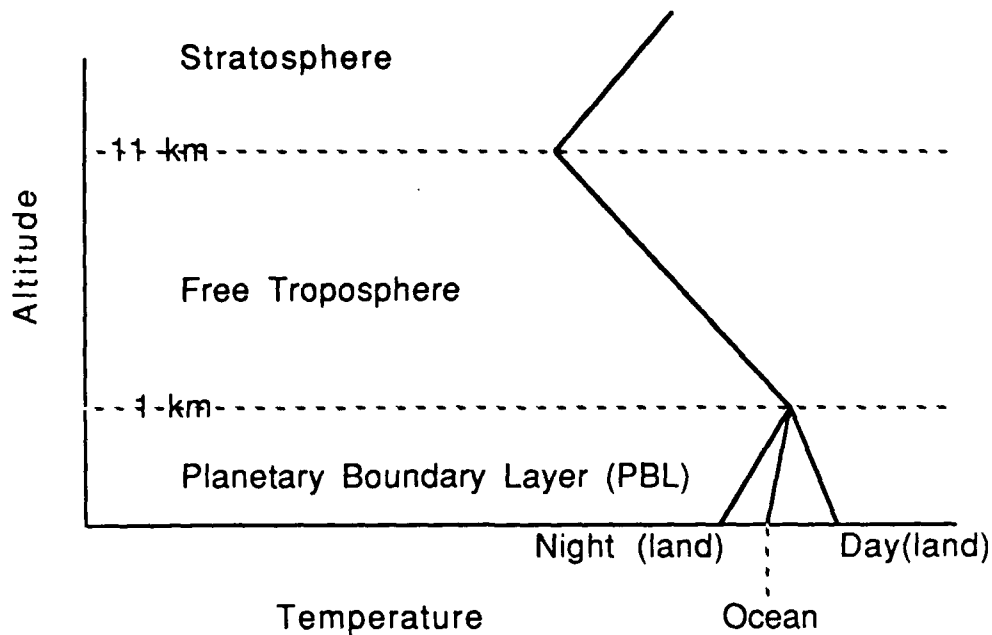


Figure 7.9. Generic Temperature Profile In the Atmosphere

Representative values for the *Adiabatic Lapse Rate* $\gamma_{ad} = -g/c_p$ are

$$\gamma_{ad} = -9.8 \text{ }^{\circ}\text{C/km for dry air (dry adiabatic lapse rate)} \quad (7.27a)$$

$$-6.5 \text{ }^{\circ}\text{C/km for moist air (moist adiabatic lapse rate)} \quad (7.27b)$$

In general there are three major types of clouds:

- *Cumulus (Cu)*: Convective clouds of extensive vertical development under unstable conditions. They occur generally in the free troposphere, although very strong thunderheads or cumulonimbus can rise to the tropopause or even into the lowest stratosphere.
- *Stratus (St)*: Layered clouds of uniform horizontal development, which are frequently found near the top of the PBL.
- *Cirrus (Ci)*: Thin, high-altitude clouds made up of ice crystals, which typically occur in the upper troposphere and may move into the low stratosphere. Cirrus form in a variety of ways, such as:
 - (a) by blowoff from cumulonimbus, or
 - (b) when a warm and therefore moist air mass approaches a cold air mass near a frontal zone.

There is evidently no unique characterization of these different morphological types of clouds. Figure 7.10 sketches different types of clouds, as viewed from above. Figures 7.10a, b, c show "representative" cumulus, stratus, and cirrus clouds, while Fig. 7.10d shows an actual cloud configuration observed one day over the U.S. Midwest from a NASA high-altitude research aircraft; notice that actual clouds tend to be a combination of the various idealized types. Lehr et al., 1965, present an excellent elementary discussion of meteorology, including good sketches of clouds and a discussion of different cloud types.⁸⁷

Table 7.4 gives some representative quantitative characteristics of different types of clouds. There are, of course, many other types of clouds, and generally low-altitude clouds occurring in the relatively warm and moist atmosphere have a higher condensed water content ($> 0.3 \text{ g/m}^3$ of condensed water) than do higher-altitude clouds that form in a colder and drier ambient atmosphere. Note that if a cloud is to form, the ambient air must be saturated with water vapor in addition to the condensed water in the droplets, and typically the water vapor accounts for most of the atmospheric moisture in the cloud, while the particles may make up 5 to 20 percent of total H_2O content.

The cloud particle size distribution is quite variable but is generally continuous, so that the mean particle scattering cross section has the character of Fig. 7.5, i.e., the violent oscillations as a function of $q = 2\pi a/\lambda$ shown in Fig. 7.4 are damped out because of the variation in particle size. One representative particle size distribution is that introduced by Deirmendjian, 1964:

$$dN(a)/da = N_d a^b e^{-ca} \quad , \quad (7.28a)$$

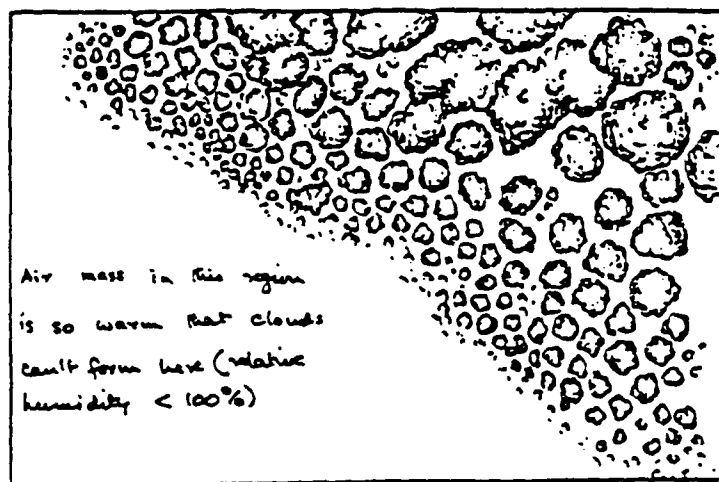
where a = particle radius, N_d is proportional to the number of particles per unit volume, and b and c are parameters. Thus, the mean radius a_{av} is

$$a_{av} = b/c \quad , \quad (7.28b)$$

and the mean number density is

$$n_{av} = N_d b! / c^{b+1} \quad . \quad (7.28c)$$

⁸⁷ An excellent description of clouds is given by Scorer, 1972. Note that there is also "subvisual cirrus" which occurs not infrequently at high altitudes. This is 10-100 times less dense than "regular" cirrus and cannot be seen with the unaided eye; it shows up on some lidars and can interfere with long-range near-horizontal viewing.

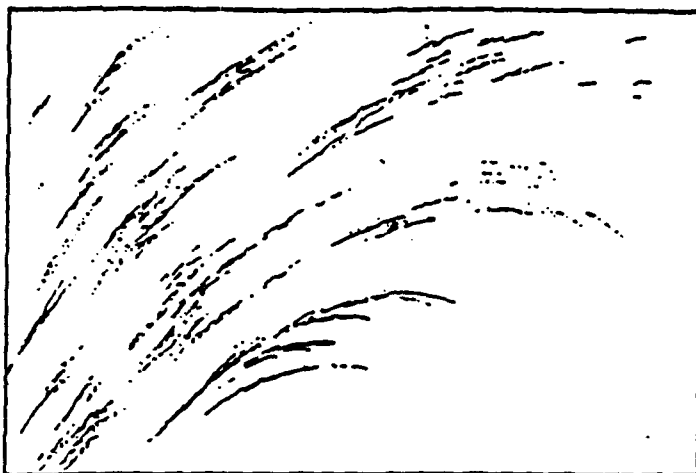


(a) Typical cumulus clouds

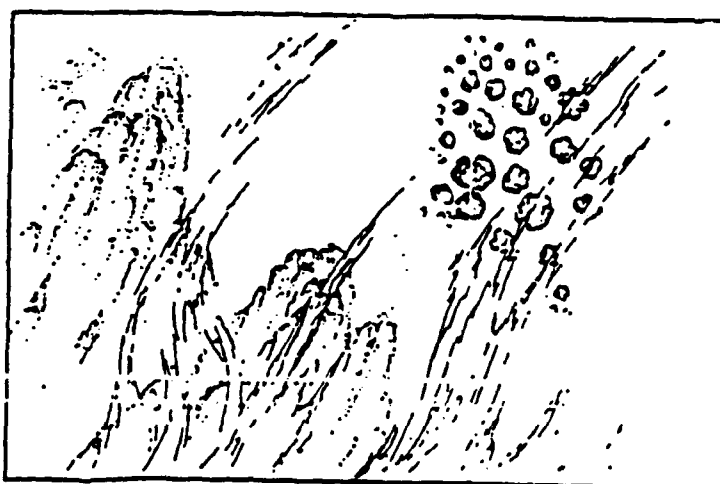


(b) Typical stratus clouds. Relatively smooth surface
producing benign background

Figure 7.10. Some "Representative" Cloud Types



(c) Typical cirrus clouds. "Fall streaks" of the relatively large ice crystals making up these clouds are typical.



(d) Sketch of an actual cloud configuration photographed by a WB-57 aircraft flying at 60,000 ft over the Midwest. Note cumulus, stratus, and cumuliiform edges, haze and cirriform clouds.

Figure 7.10. (continued)

Table 7.4. Some Representative Examples of Cloud Properties

Cloud Type	Altitude Range	Condensed Water Content (η/m)	Mean Particle Radius (μm)	Phase	Extinction Distance* (m)
Low (stratus [St]; cumulus [Cu]; strato-cumulus [SC]; nimbostratus [Ns], etc.)	< 2 km	0.3 (0.1-1)	4	water	13
Middle (altocumulus [ACu]; altostratus [AS])	2-6.5 km	0.1 (0.1-1)	4	water	40
High (cirrus [Ci]; cirrostratus [Cs], etc.)	> 6.5 km	0.01-0.1	32 (not spheres!)	ice	300-3000
<p>Mode of formation of different cloud types.</p> <p>Cumulus: Convection: a warm, moist parcel of air rises, typically as a result of solar-induced heating. Cu range from small regularly organized "popcorn cumulus" which serve as an important means of raising H_2O from the surface layer into the free troposphere, to large cumulonimbus (CB) which lead to thunderstorms and may extend above the tropopause, into the lower stratosphere.</p> <p>Stratus: Clouds of relatively large extent formed when warm, moist air is cooled by rising, e.g., at a frontal zone or by motion over a range of mountains.</p> <p>Cirrus: Clouds that are formed by a variety of mechanisms such as blow-off by wind from cumulonimbus or uplifting of air associated with frontal systems.</p> <p>*Extinction distance = $1/[(\text{extinction cross section}) \times (\text{number of particles/unit volume})]$ Extinction cross section = $2 \times \text{geometrical cross section}$ Meteorological visibility = $3.91 \times \text{extinction distance}$ ($3.91 = \ln 50$)</p>					

For water clouds, $a_{av} = 4 \mu\text{m}$, $b = 6$, $c = 1.5 \mu\text{m}^{-1}$ are plausible values, while for ice clouds, $a_{av} = 32 \mu\text{m}$, $b = 6$, $c = 0.1875 \mu\text{m}^{-1}$ may be used.

Note that clouds are highly variable but not random. Cumulus clouds will change as observed over a 10- to 30-min period, which is the typical lifetime of an individual cumulus convection cell. Cirrus change noticeably over times of 1 to 3 hours, while stratus clouds are relatively long-lived, with lifetimes are in the 3-10 hr range. The bottom surface of a cloud is normally fairly sharp as compared with the top, because its position is determined by the local condensation temperature in the atmosphere of the air parcel which gives rise to the particular cloud system; by contrast, the top of a convective cloud system shows the characteristic shape due to turbulent convection.

Table 7.5 gives the time-space scales of different types of meteorological phenomena which reflect on the underlying atmospheric motions. Atmospheric motions are often described as a combination of advection (= convection) and turbulent diffusion, but there is no very clear distinction between them, except perhaps time-space scales. Representative wind speeds are 10-100 m/sec horizontally, and 0.01-0.1 m/sec vertically; Fig. 7.11 shows "representative" horizontal winds, which vary strongly with altitude. Atmospheric diffusion is highly scale-dependent; Fig. 7.12 shows horizontal mean diffusive (i.e., non-convective) motions. Note:

- (a) The wide range of variability of data from the mean curve III to the lower and upper bounds I and IV respectively.
- (b) The scales of atmospheric motions from Table 7.4 correspond quite well with the bounds I and IV of the figure.
- (c) These data are mainly tropospheric (1-10 km altitude) but apply up to 20-25 km.
- (d) An older range of variability (Bauer, 1974) with mean curve II and bounds I and III should not be used, since it is based on older observations which in general are biased towards quiet atmospheric conditions. (The older observational techniques had limited sensitivity, so that under non-quiet conditions the tracer cloud would be dispersed so rapidly that no measurements could be made.)

Table 7.5. Representative Scales of Atmospheric Motions
(Source: Bauer, 1983)

Region on Fig. 7.12. Scale			Phenomena	Affected Scale (Approximate)	
				Horizontal Dimension	Time
From Hobbs (1981): Different Atmospheric Motions					
H1	Micro- γ	Plumes, Mechanical and Isotropic Turbulence	2 m to 20 m	1 sec to 1 min	
H2	Micro- δ	Dust Devils, Thermals, Mists	20 m to 200 m	0.5 min to 3 min	
H3	Micro- α	Tornadoes, Deep Convection, Short Gravity Waves	200 m to 2 km	2 min to 1 hr.	
H4	Meso- γ	Thunderstorms, Internal Gravity Waves, Clear Air Turbulence, Urban Effects	2 to 20 km	6 min to 3 hr.	
H5	Meso- δ	Nocturnal Low-Level Jet, Inertial Waves, Cloud Clusters, Mountain and Lake Disturbances, Rainbands, Squall Lines	20 to 200 km	2 hrs. to 1 day	
H6	Meso- α	Front Hurricanes	200 m to 2000 km	5 days to 1 month	
H7	Macro- δ	Baroclinic waves	2000 km to 5000 km	2 days to 1 month	
H8	Macro- α	Standing Waves, Ultra-long Waves, Tidal Waves	> 10,000 km	> 1 day	
From Ramage (1976): Turbulence Bursts on Different Scales					
R1	Convective	Hot Towers	2 km to 10 km	15 min to 2 hrs.	
R2	Mesoscale	Flash Floods	10 km to 100 km	2 hrs. to 6 hrs.	
R3	Sub-synoptic	Tornadoes, Clear Air Turbulence, etc.	100 km to 500 km	6 hrs. to 12 hrs.	
R4	Synoptic	Continuous Thunderstorms, Large Scale Convection	500 km to 2000 km	12 hrs. to 48 hrs.	
R5	Planetary	Hurricanes, etc.	> 2000 km	24 hrs. to 48 hrs.	

Altitude (km)	Wind Speed				
	Percentile (m/s)				
	50	75	90	95	99
1	8	13	16	19	24
6	23	31	39	44	52
11	43	55	66	73	88
12	45	57	68	75	92
13	43	56	67	74	86
20	7	12	17	20	25
23	7	12	17	20	25
40	43	57	70	78	88
50	75	83	91	95	104
58	85	96	106	112	123
60	85	96	106	112	123
75	15	22	28	30	37
80	15	22	28	30	37

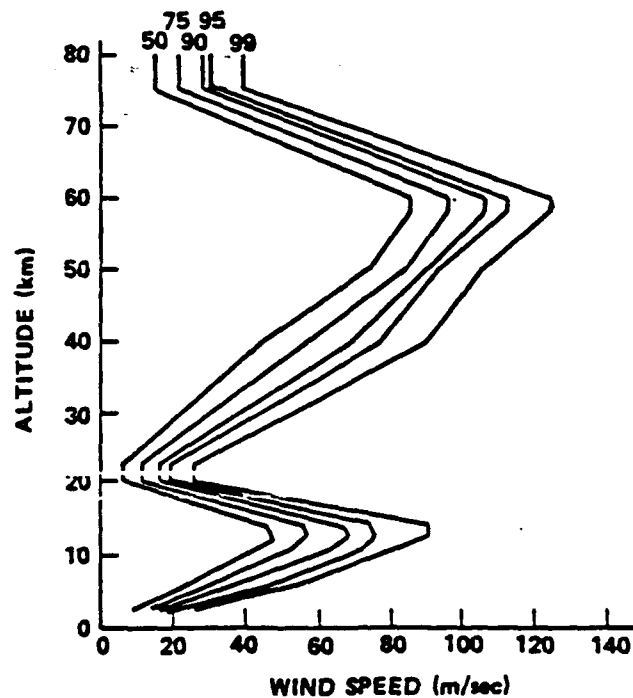


Figure 7.11. Steady-State Horizontal Cumulative Wind Speed Profiles (m/sec) for Cape Canaveral Space Center (Source: Turner and Hill, 1982) (At 1 km altitude, 99% of the time the wind speed is < 24 m/sec).

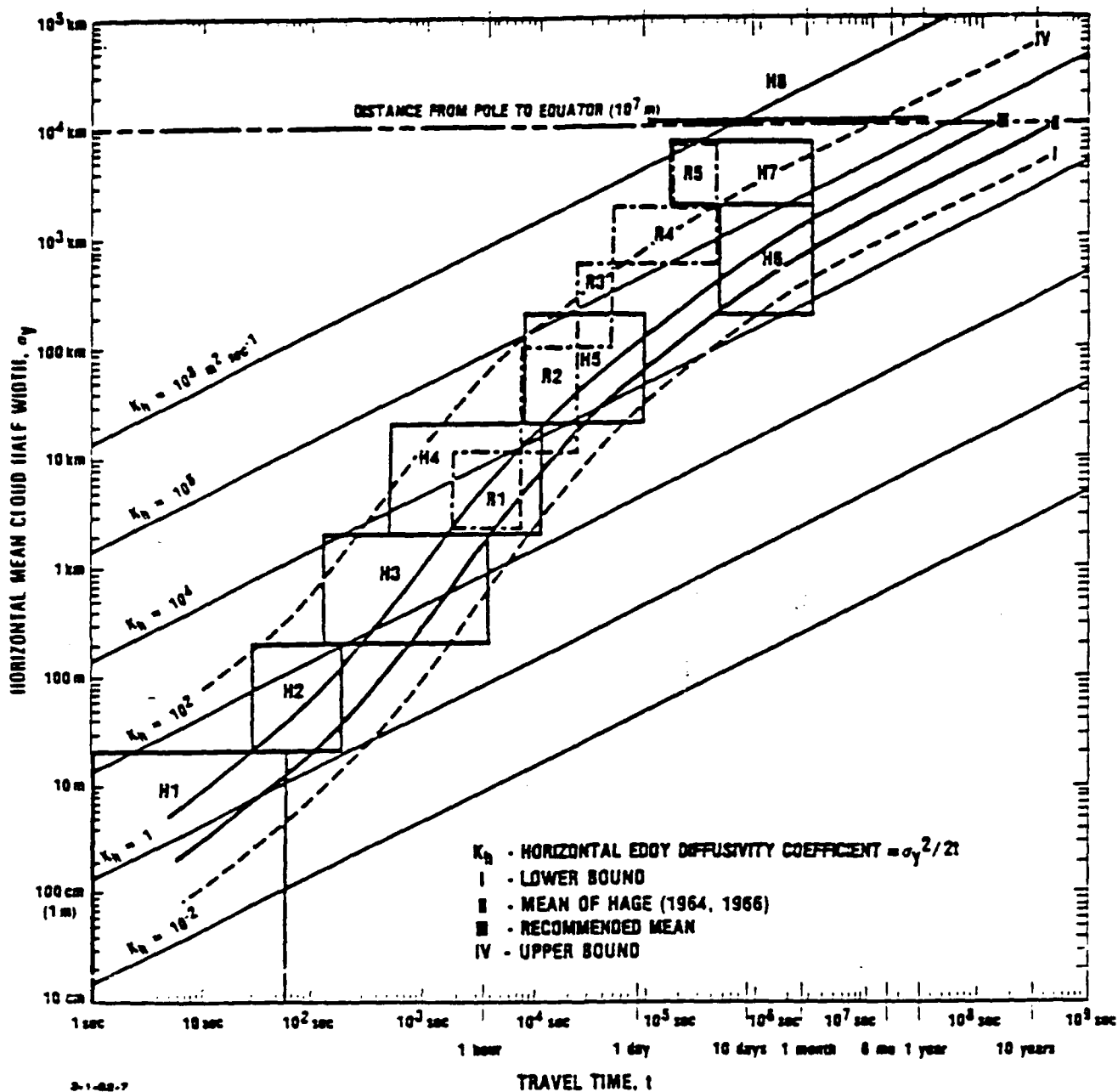


Figure 7.12. Horizontal Dispersion as Function of Travel Time. The Blocks H1, H2,...,R1, R2,... come from Table 7.5. (Source: Bauer, 1983)

7.5 CLOUD-FREE LINE-OF-SIGHT (CFLOS) ANALYSES

7.5.1 Introduction

We recognize that clouds occur very frequently--see, e.g., Table 7.1--and are highly variable--see, e.g., Fig. 7.10. Visible and infrared radiation cannot penetrate optically thick clouds directly, although the brightness of visual illumination under complete cloud cover is as much as $1/8$ to $1/4$ of the full solar illumination. For instance, to take a photograph under cloudy skies one increases the aperture by just 2-3 stops, but reference to Table 7.3 shows that water clouds are very much more absorptive in the infrared than in the visible.

A number of specific questions arise on how often there are clouds in the field of view of the human eye, or of a visible or infrared sensor, which interfere with its seeing a given object ("target"). This is normally treated as a probabilistic issue, but we shall begin by recalling what clouds look like in a little more detail than the generic model presented in the previous section, and how the clouds interfere with optical sensing of a target.

Table 7.6 is a "do-it-yourself" example of what clouds "actually" look like. I decided to look out of my office window or equivalent for 19 successive days (actually between 13 and 31 May 1988) at 10 a.m. and 3 p.m. and ask:

- (a) What fraction of the sky is covered?
- (b) What type of cloudiness is observed?

While the results are not quantitatively significant, yet they give the interested reader a good feeling for how much cloud cover there actually is and for the complexity and variability of real clouds, before he plunges into a probabilistic analysis of Cloud-Free Line-of-Sight (CFLOS).

One further remark should be made here. For surveillance from high altitude one is interested in local holes in cloud cover which enable one to observe a designated target from above. A "hole" in cloud cover is an inverse of the presence of a cloud only in a mathematical rather than a physical/meteorological sense. Cumulus clouds are ~ 1 -10 km in linear dimension, spaced a comparable distance apart, but stratus cloud decks rarely have cloud-free holes. Rather, a hole in cloud cover is often to be interpreted in terms of Fig. 7.10, as a gap between overlapping layers of low, middle, and high clouds of different types. Statistics of clear versus cloudy intervals under different levels of total

cloud cover are listed in Table 7.7. A somewhat different representation of Cloud-Free Intervals (CFIs) at different locations is given by Malick and Allen, 1978, 1979, and this is discussed in Section 7.5.3 below.

Having given this phenomenological introduction to what clouds actually look like, let us now address the probabilistic issue which has been addressed by a number of different data bases and methodologies. Here are listed some specific questions of interest, representative data bases used in answering them, and relevant analyses. The examples listed here are intended to be representative rather than complete.

Specific questions that are often addressed by the DOD community deal with the probability of the following:

- Clear and cloud-free conditions, including effects of haze or thin cirrus
- Cloud-Free Field of View (CFFOV)
- Cloud-Free Interval (CFI) on a given path
- Dynamic Cloud-Free Line-of-Sight (DCFLOS)--which considers the temporal motion of cloud, target, or sensor.⁸⁸

For current work in this field, the reader is referred to the annual reports of the CIDOS (= Cloud Impacts on DOD Operations and Systems) Conference.⁸⁹

7.5.2 Data Bases

- De Bary and Moeller, 1963, German Weather Service aircraft flights over Germany in the 1930s.
- Lund and Shanklin, 1972, AFGL, all-sky camera pictures at Columbia, MO. (This data base is being updated, beginning in 1988, by using six all-sky vidicon cameras at various locations in the USA.)
- Bertoni, 1977, AFGL, extensive pilot reports of clear and cloud-free lines of sight in the northern hemisphere (data should be used with great caution).
- Avaste et al., 1974--see also Ellingson, 1982--Soviet/East European data base.
- National Weather Service--a wide variety of NWS and USAF data are available from National Climatic Center, Asheville, NC.

⁸⁸ This problem is so complicated that analyses such as that of Nelson and Wetherbe, 1976 are not used extensively.

⁸⁹ Published by AFGL: contact Dr. Wm. Snow, 617-377-5952.

**Table 7.6. A Do-It-Yourself Actual Example of Cloudiness:
Cloudiness During 13-31 May 1988 in the Washington, DC, Area**

Date (May, 1988)		10 a.m.		3 p.m.	
		Type*	Cover** (tenths)	Type	Cover (tenths)
F	13	Cs	8	Cs	6
S	14	Sc	8	Sc	8
Su	15	Sc	6	Sc	8
M	16	St	10	As	5
Tu	17	Ac	5	Ac	7
W	18	Sc	10	Sc	9
Th	19	Cu	5	Cu	5
F	20	St	10	St	10
S	21	Sc	6	Cu	6
Su	22	Cu	2	Cu	3
M	23	Ci	1	Cu	3
Tu	24	Ci	1	Cu	6
W	25	Ns (rain)	10	St	4
Th	26	--	0	--	0
F	27	--	0	--	0
S	28	Cu	2	Cu	6
Su	29	--	0	Cu	2
M	30	Ci	2	Cu	3
Tu	31	--	0	Cu	2
Average Cloudiness:		10 a.m.: 0.45;		3 p.m.: 0.49	

- * Notation used is standard: Ci (cirrus), Cs (cirrostratus), Cc (cirrocumulus) are thin high clouds; As (altostratus), Ac (altocumulus) are thicker "middle" clouds (1-5 km altitude); Ns (nimbostratus) are rain clouds; Cu (cumulus) are convective clouds of relatively large vertical extent; Cb (cumulonimbus) are thunderheads; St (stratus) and Sc (stratocumulus) are low clouds, largely of horizontal extent.

- ** In general, stratiform clouds (St, Sc) are evaporated by solar radiation as the day passes, i.e., there is more stratus in the morning than in the afternoon. However, cumuliform clouds (Cu, Cb) are produced by solar-induced convection, so that they are more likely to occur during the afternoon/evening than in the morning.

Table 7.7 Cloud Cover: Mean Horizontal Sizes of Clouds and Spaces Between Them. [Source: Spiridonova (1976)--see Matveev, 1984, p. 253 ff]

- Analysis of TV cloud pictures from Cosmos and Meteor satellites between 1967 and 1971, over latitudes from the equator to 60 deg N, and longitudes between 160 deg E and 70 deg W (North America and Adjacent Pacific Ocean, approximately one-third of the area of the northern hemisphere). Daylight only, minimum resolution 4 km.
- Data are broken down by season (January or July), by land or sea, and by Scattered, Broken, Overcast, and Total Cloud cover, which correspond, respectively, to 2/10-5/10, 5/10-8/10, 8/10-10*/10, and 10/10 cloud cover, where 10*/10 is "total cloud cover with gaps." The figures are, respectively, cloud size and cloud spacing, all in km. (Thus, for scattered cloud cover over ocean in January, the mean cloud size is 13 km with 10 km standard deviation, and a mean cloud spacing of 40 km. Evidently, for 10/10 cloud cover over the ocean in January, the mean size of a solid cover is 190 km.)

Mean Cloud Size/Spacing

	Ocean		Land	
Cloud cover	January	July	January	July
Scattered(2-5/10)	13/40	8/78	16/47	10/64
Broken (5-8/10)	29/21	17/60	29/31	9/27
Overcast (8-10*/10)	46/19	49/13	140/60	21/21
Total(10/10)	190	76	410	63

Standard deviation of cloud sizes:

Scattered (2-5/10)	10	9	15	9
Broken (5-8/10)	27	29	26	19

- USAF 3DNEPH and RTNEPH--see Fye, 1978, and Kiess and Cox, 1988. These use mainly satellite imagery from DMSP and NOAA polar-orbiting satellites, supplemented by ground and pilot reports to provide global coverage (from 1975 on) on a spatial resolution of 26 nm (48 km) updated every six hours.

7.5.3 Some Representative Analyses

- Lund, 1965, 1966, AFGL, clear LOS from sunshine and cloud-cover observations.
- Lund and Shanklin, 1973, AFGL, use Lund and Shanklin, 1972 data base.
- Lund, Grantham, and Elam, 1975+, AFGL/ETAC, global atlas using Lund-Shanklin and other ground-based data.
- Rapp, Schutz, and Rodriguez, 1973 conducted an error analysis of various "early" CFLOS analyses, and concluded that the Lund-Shanklin model was the best available one.
- Malick and Allen, 1978, 1979, SRI/DARPA, combine 3DNEPH global data and the Lund-Shanklin analysis.
- De Violini, Shlanta, and Elam, 1980, USN, global marine atlas using 3DNEPH data.
- Katz, DeBold, and Perez-Esandi, 1980, NSWG, surface-to-air data using surface marine observations from NWS and Lund-Shanklin analysis.
- USAF-AWS provides a variety of outputs from RTNEPH.

Figure 7.13 shows the probability of a cloud-free line of sight (PCFLOS) as a function of elevation angle θ and sky cover S . This compares the modification by Malick and Allen, 1978, 1979, of the Lund and Shanklin, 1972, work which may be considered as the "U.S. Standard" model with the Soviet/Eastern European model of Avaste et al., 1974 (see also Ellingson, 1982). Note that for near-zenith viewing (θ large),

$$\text{PCFLOS} = 1 - S \quad , \quad (7.29)$$

but for oblique viewing ($\theta < 30$ -40 deg) the PCFLOS becomes very much smaller (all curves converge to zero at $\theta = 0$). The difference between the U.S. and Soviet models tends to reflect on the fact that the Soviet Union is a very cloudy and high-latitude country.

The analytic fit of Malick and Allen, 1978, postulates an average cloud thickness-to-width ratio b which depends on the fractional sky cover S through the relation

$$b = 0.55 - S/2 \quad . \quad (7.30)$$

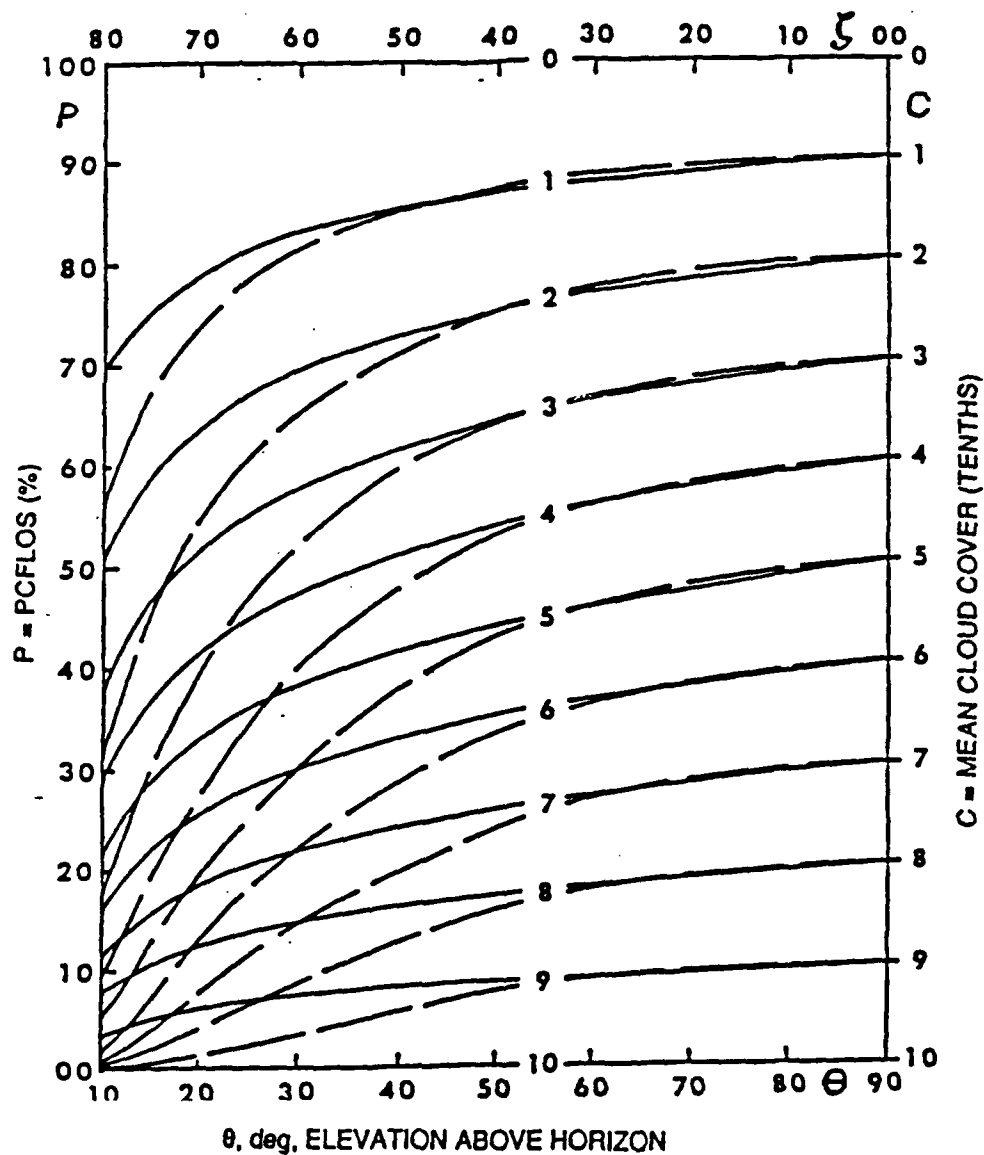


Figure 7.13. Probability of CFLOS as Function of Elevation Angle θ and Cloud Cover C , for both U.S. and Soviet/Eastern European Models (respectively, solid and dashed curves). ($\zeta = 90^\circ - \theta$)
(Figure kindly provided by J.W. Snow, AFGL)

The fractional sky cover S applies to visual observation over the hemisphere looking up from the ground, as contrasted to the fractional cloud cover Q as seen looking down from space. According to Malick and Allen, 1978, these two quantities are related by the empirical relation

$$Q = (S/4) (1 + 3 S) \quad (7.31)$$

Now Malick and Allen parameterize the Lund-Shanklin results as a function of elevation angle θ as follows:

$$PCFLOS = (1 - Q) (1 + b/\tan\theta) \quad (7.32)$$

The Malick and Allen model is attractive because it provides simple and generally usable results, but it clearly oversimplifies the real situation. However, where this kind of simple model is not adequate, it may be appropriate to use numerical results from the RTNEPH data base.

7.5.4 Horizontal Viewing

Most CFLOS analyses involve upward looking observers or sensors who measure sky cover, or else downward (nadir) viewing satellites that measure earth cover. This is satisfactory for viewing most of the sky dome, but it fails for (near)-horizontal viewing,⁹⁰ such as for an IRST (Infrared Search and Track) application. Here it is more appropriate to use results from the NASA SAGE (Stratospheric Aerosol and Gas Experiment) and SAM satellites which use near-visible sensors viewing the sun horizontally through the "earth limb", and thus provide direct experimental data on the probability of a cloud-free line of sight along a horizontal earth limb path as a function of tangent height.⁹¹

The SAGE and SAM limb-viewing solar photometers are flown on separate satellites to provide global coverage and are intended primarily to study stratospheric aerosols and gases (see McCormick et al., 1979). However, observations go down to tangent heights as low as 5 km and they show an enhanced extinction at the lower altitudes which is due to high-altitude clouds--see Figure 7.14. Livingston and Malick, 1983, have analyzed the initial 1.5 years of SAGE data to determine the PCFLOS as a function of tangent height. Figure 7.15 shows their results as a function of latitude and season.

⁹⁰ Thus note that Fig. 7.13 shows no results for elevation angles $\theta < 10$ deg above the horizon.

⁹¹ The effective path length in the atmosphere is of the order of 200 km.

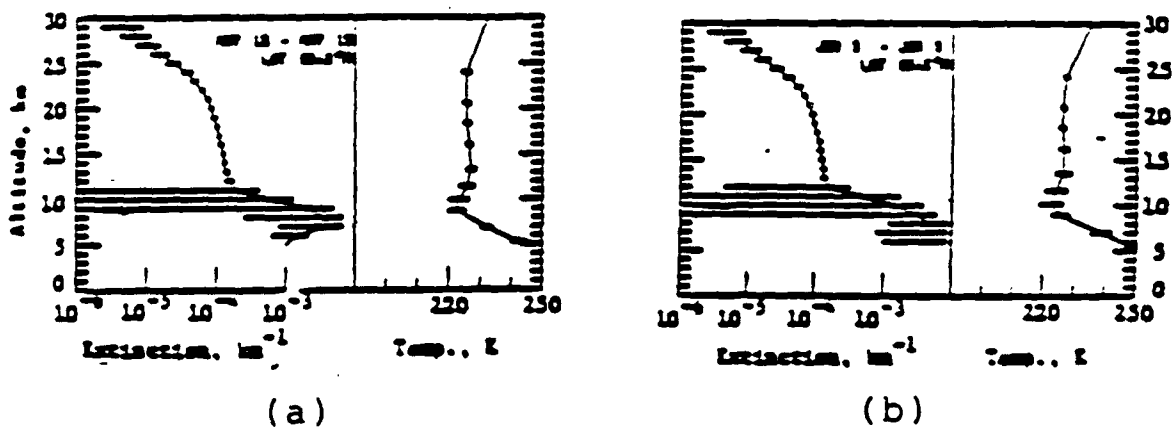


Figure 7.14. Limb-viewing observations of aerosol-cloud extinction from the NASA SAM-II sensor at $\lambda = 1 \mu\text{m}$ (SAGE is similar). The maximum in extinction in (a) at 7 km is presumably due to high-altitude clouds.
(Source: McCormick et al., 1982)

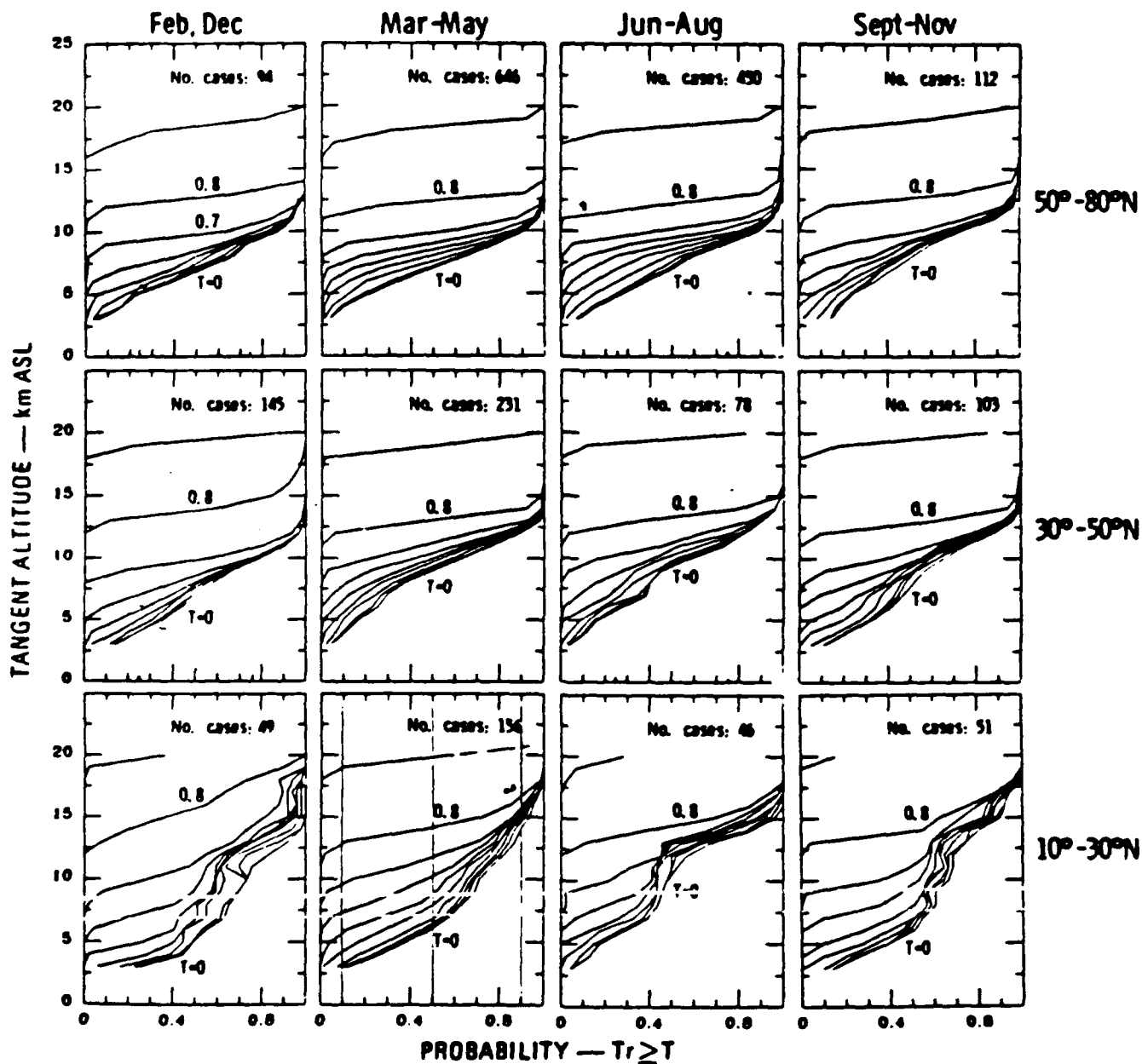


Figure 7.15. Seasonally Derived $1.0 \mu\text{m}$ Transmission Curves From SAGE Plotted as a Function of Tangent Altitude and Probability for Three Northern Hemisphere Latitude Bands.
(Source: Livingston and Mallick, 1983)

It is possible to extract information on the frequency of occurrence of a cloud-free line of sight in horizontal viewing as a function of tangent height on the assumption that the low-altitude extinction shown in Fig. 7.14 is due to high-altitude clouds located near the tangent region, i.e., that the frequency of cloudiness decreases monotonically with increasing altitude. Some results for summer and winter at latitudes of 30-50 deg N are given in Fig. 7.16. As an example of how to use these data, consider winter conditions, and a transmittance of 0.5. Then the minimum tangent height z_{tan} which can be achieved 10 percent, 50 percent, and 90 percent of the time is, respectively, 4.4 km, 8.0 km, and 11.0 km, and for a sensor at height z_0 viewing a target at the same altitude, the range achievable s , is related to z_0 , z_{tan} , and the radius of the earth, $R_0 = 6400$ km by the simple geometrical relation

$$s = 2 \sqrt{[2 R_0 (z_0 - z_{tan})]} \quad (7.33)$$

Thus we see that under the listed conditions, the maximum range achievable 10 percent, 50 percent, and 90 percent of the time is, respectively, 620 km, 450 km, and 230 km for both target and sensor at height $z_0 = 12$ km (39,000 kft.).

7.6 ATMOSPHERIC TURBULENCE

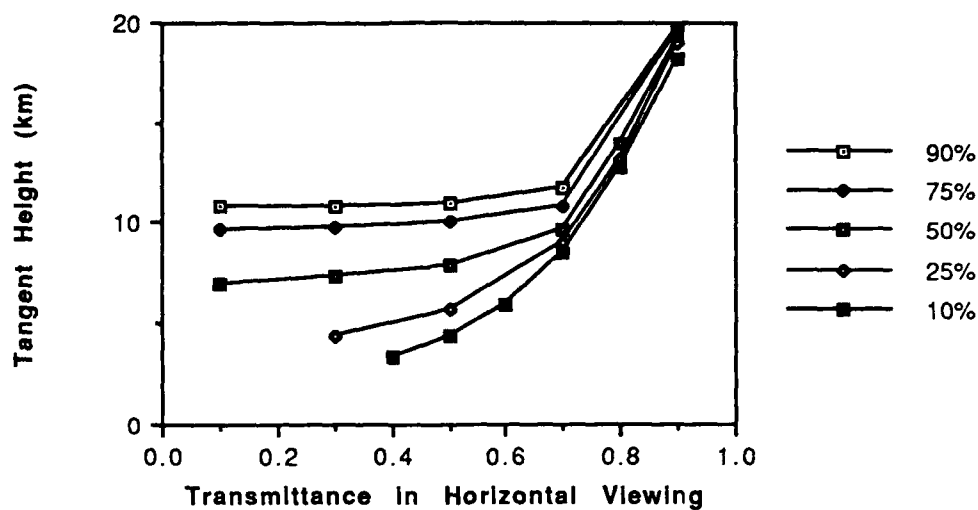
The atmosphere is not a homogeneous optical medium. The temperature, pressure, and humidity are not spatially or temporally uniform, and this leads to random variations in the index of refraction $n(\underline{r}, t)$ seen by a propagating electromagnetic wave. In the atmosphere, the refractive index n differs only very slightly from unity: a typical value at sea level is 1.0003, but fluctuations on the order of one percent in the 3×10^{-4} residual are sufficient to produce beam wander, beam spread and intensity fluctuations in a laser beam, and also limit astronomical and other "seeing" through the atmosphere. These phenomena arise because of fluctuations in the residual, $(n-1)$, due to atmospheric turbulence, which accumulate along an optical path through the atmosphere.

The refractive residual $(n-1)$ is proportional to the density, and thus

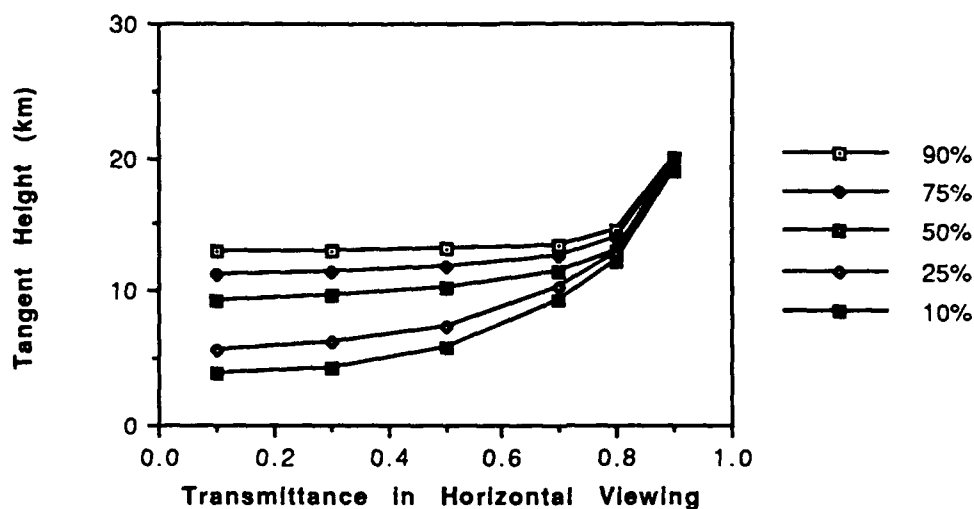
$$(n-1) = A P/T \quad (7.34)$$

where $A \sim 7.9 \times 10^{-5}$ (K/millibar) for red light (cf., HELPH-I, p. 5-3). It is appropriate to express changes δn in terms of changes $\delta \theta$ in potential temperature

$$\theta = T - \gamma_{ad} z \quad (7.35)$$



(a) Winter



(b) Summer

Figure 7.16. Probability of Attaining a Given Tangent Height in Horizontal Viewing as a Function of Horizontal Atmospheric Transmittance. Results for Winter and Summer, 30 deg to 50 deg N latitude Bands Computed from the Results of Fig. 7.15.

where z = altitude and γ_{ad} = adiabatic lapse rate- see Eq.(7.27)--because (unlike the temperature T), the potential temperature θ is conserved in the atmosphere. Thus

$$\delta n = - A(P/T^2) \delta \theta \quad , \quad (7.36)$$

while at constant altitude z :

$$\delta \theta = \delta T \quad . \quad (7.37)$$

In a turbulent atmosphere, the local temperature is a random variable, and it is customary to introduce a structure function

$$D_T(r_2 - r_1) = \langle [T(r_2) - T(r_1)]^2 \rangle \quad (7.38)$$

where the brackets $\langle \rangle$ imply an ensemble average in which all possible point pairs r_1, r_2 are averaged. By imposing the condition of isotropy of turbulence, we remove dependence on the vector coordinates r_1 and r_2 and only need to consider the magnitude $r = |r_2 - r_1|$ of the difference between the two coordinates. Kolmogorov, 1972, demonstrated by the use of dimensional analysis that as long as r is restricted to the "inertial subrange," Eq. (7.38) has a $r^{2/3}$ power law dependence

$$D_T(r) = C_T^2 r^{2/3} \quad . \quad (7.39)$$

Likewise, from Eqs. (7.36) and (7.37) the index of refraction structure function $D_n(r)$ is

$$D_n(r) = C_n^2 r^{2/3} = C_T^2 r^{2/3} (AP/T^2)^2 \quad . \quad (7.40)$$

The parameter C_n^2 is frequently used to describe atmospheric turbulence.

Figure 7.17 is a sample profile of the variation of C_n^2 from the ground to 30 km altitude. It also shows the simultaneously measured wind speed profile. This profile was taken during a jet stream passage and is thus an instructive example of some of the characteristics of atmospheric turbulence. A typical feature shown is the occurrence of the largest values of C_n^2 at the surface with a rapid falloff. In addition to the jet stream enhancements, the other significant characteristic of atmospheric optical turbulence demonstrated here is the stratification. Turbulence always occurs in layers in which C_n^2 can exceed the "background" value by more than 100. In some applications of vertical

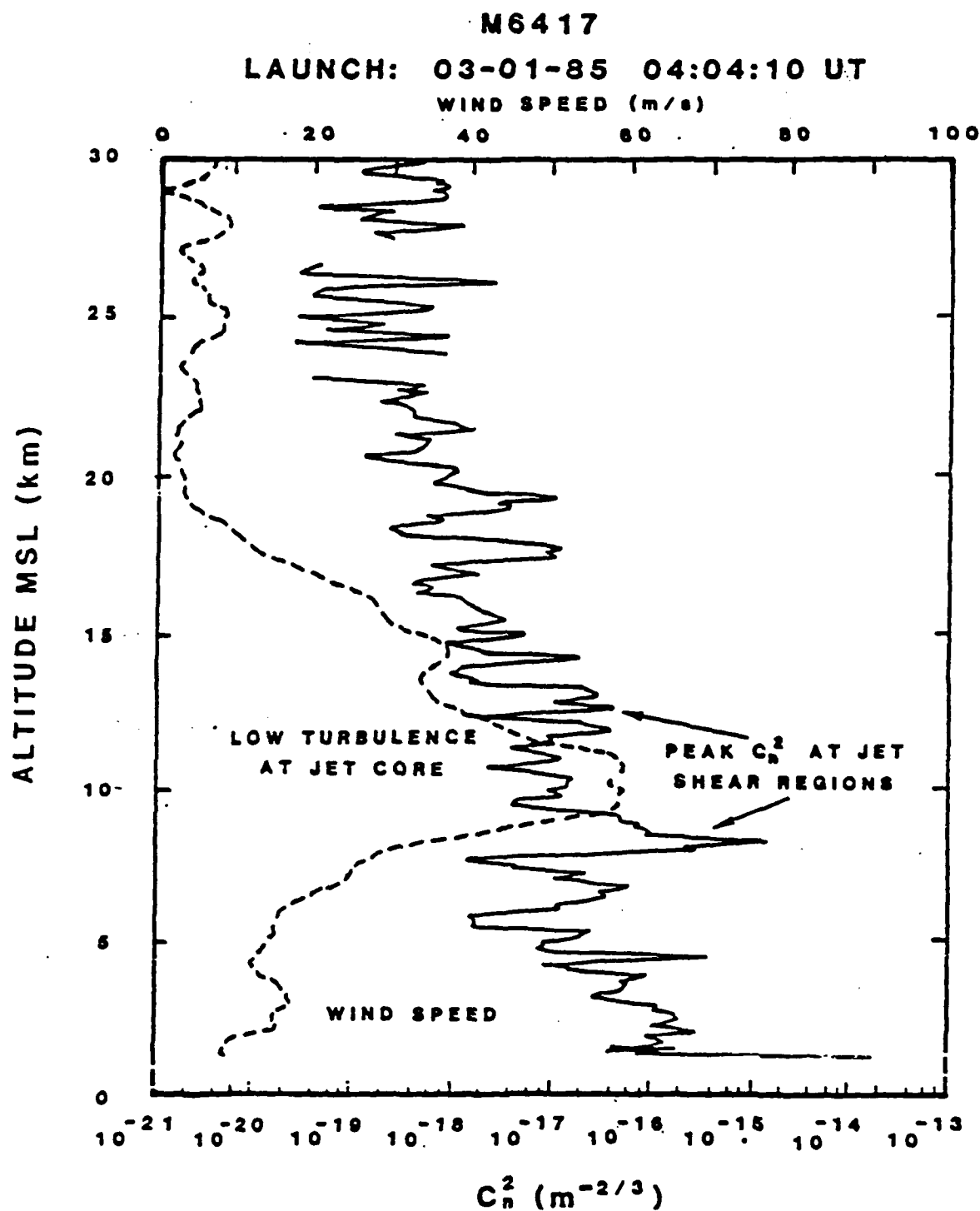


Figure 7.17. Optical Turbulence in the Atmosphere: a Sample of the Parameter C_n^2 as Function of Altitude. (Data Provided by R.R. Beland, AFGL)

propagation this layering is not important, but in others, particularly for horizontal propagation, the layering may be very significant.⁹²

The discrete layers of atmospheric turbulence shown in Fig. 7.17 are characterized by the Richardson's number Ri --see Section 5.6.4--rather than by the Reynolds' number Re of Section 5.6.3--which characterizes aerodynamic rather than atmospheric turbulence. For a simple discussion of atmospheric turbulence, see USAF, 1985, p. 19-6ff.

7.7 NON-LINEAR EFFECTS FOR HIGH-INTENSITY LIGHT BEAMS

7.7.1 Introduction

When a high-intensity beam of radiation passes through a medium, even a small fractional absorption can lead to significant effects on propagation. For instance, consider a 10-MW laser beam propagated from a 3-m diameter mirror in the sea level atmosphere. Even if we assume an absorption coefficient as low as 0.01 m^{-1} , which corresponds to a mean molecular absorption cross section of $4 \times 10^{-24} \text{ cm}^2$ or 10^{-9} times gas kinetic, the heating rate is 170 K/sec because $c_p = 1.0 \text{ J/g K}$. It is thus clear that the propagation of a high-intensity beam of radiation, such as from a high-energy laser, deposits a large amount of energy in the atmosphere that can lead to significant changes in the ambient medium which in turn affects beam propagation.

To some extent it is possible to correct adaptively for these changes in the propagation medium. These corrections will not be discussed here (see, e.g., APS, 1987) but I introduce the relevant atmospheric concepts for adaptive correction for turbulence and other disturbances of the propagating atmosphere. These are the (phase) *coherence distance* r_0 and the *isoplanatic angle* θ_0 . In the absence of turbulence or other disturbances of the medium, the phase variation $\phi(\underline{r})$ across the aperture of a beam is determined uniquely by its initial distribution across the launching aperture; explicitly, if a coherent laser beam of wavelength λ is launched from an aperture of diameter D , after traveling a path length L its area at the target will be

$$A_{\text{ideal}} = (\lambda L/D)^2, \quad (7.41)$$

but in a turbulent medium of coherence distance r_0 , the effective beam area will be

⁹² Note that frequently used models of C_n^2 are smoothed fits to averaged data and thus do not exhibit this layering.

$$A \sim A_{\text{ideal}} [1 + (D/r_0)^2] \quad (7.42)$$

A typical value for r_0 in the visible is 5 to 10 cm, and it scales as $\lambda^{6/5}$. The isoplanatic angle defines a cone in the atmosphere where the wavefront is coherent in an angular sense.⁹³ To correct for perturbations in the propagating medium by adaptive optics techniques, it is necessary to define a reference wavefront which cannot be displaced from the outgoing wavefront by more than θ_0 . Typical values of θ_0 are 3-10 μrad in the visible, and it scales as $\lambda^{6/5}$. It is to be compared with the point-ahead angle θ_{pa} required to track and point at fast-moving objects. At geostationary satellite altitudes, $\theta_{\text{pa}} \sim 15\text{-}20 \mu\text{rad}$.

Here we give a brief discussion of thermal blooming; another process which become significant at flux levels in excess of $1\text{MW}/\text{cm}^2$ is stimulated Raman scattering, in particular rotational Raman scattering in N_2 . For a discussion, see, e.g. APS, 1987, p.S108f.

7.7.2 Thermal Blooming

The numerical example at the beginning of the previous subsection points out that intense laser beams propagating through the atmosphere produce significant heating of the medium due to absorption of the radiation by molecules and aerosols. This heating will cause the density and thus the refractive index to decrease in the region of the beam, according to the relation

$$(n - 1) = k_{\text{GD}} \rho \quad (7.43)$$

where the Gladstone-Dale constant $k_{\text{GD}} \sim 0.22 \text{ cm}^3/\text{g}$ throughout the IR or roughly twice that large in the visible (cf., *IR Handbook*, 1985, p. 24-16). The effect of this change in refractive index is to produce an aberrated negative lens whose profile is related to the beam profile. This produces a deflection and defocusing of the beam in a complex fashion which is called "thermal blooming." Laser wavelengths for atmospheric propagation are chosen where absorption is weak, but the numerical example cited above demonstrates that residual absorption, together with the intense radiation, can lead to blooming. The absorbed energy per unit volume is the product of the beam intensity, the absorption coefficient, and a time which can depend on beam motion through the air and heat transport due to wind and/or slewing of the beam.

⁹³ For turbulence-degraded phase fronts measured in two directions θ and $(\theta + \theta_0)$ the correlation coefficient between the two will be e^{-1} .

The physics of blooming is reasonably well understood, if complex. There are two limits of time dependence, namely a steady-state behavior, which is generally important for continuous wave laser propagation, and a transient or t^3 behavior, which frequently dominates in the case of pulsed laser propagation. For a discussion of CW blooming, see APS, 1987, p. S105f; a complementary discussion is given in HELPH-I, Ch. 6.

8. BIBLIOGRAPHY

H.J. Allen and A.J. Eggers, Jr., "A Study of the Motion and Aerodynamic Heating of Ballistic Missiles Entering the Earth's Atmosphere at High Supersonic Speeds," NACA Report 1381, Washington, DC, 1958.

J.D. Anderson, Jr., *Modern Compressible Flow: With Historical Perspective*, McGraw-Hill, NY, 1982.

J.D. Anderson, Jr., "A Survey of Modern Research in Hypersonic Aerodynamics," AIAA Paper 84-1578, June 1984.

J.D. Anderson, Jr., *Fundamentals of Aerodynamics*, McGraw-Hill, NY, 1984.

J.D. Anderson, Jr., "Hypersonic Aerodynamics," Short Course, May 1986.

APS = American Physical Society Study on the Science and Technology of Directed Energy Weapons, *Rev. Mod. Phys.* 59 (No. 3, Part II), July 1987.

O.A. Avaste et al., "On the Coverage of the Sky by Clouds," in *Heat Transfer in the Atmosphere*, Feygelson and Tavang, Eds., NASA Technical Translation TT-F-790, pp. 173-181 (NTIS N74-30841/2GI), 1974.

G.E. Barasch, "Light Flash Produced by an Atmospheric Nuclear Explosion," *Los Alamos National Laboratory Mini-Review* 79-84, November 1979.

E. Bauer, "Scattering of IR Radiation from Clouds: Interpretation of the Baird-Atomic Experimental Data (U)," *Proc. IRIS* 8, #4, 43L, 1963 (SECRET).

E. Bauer, "The Scattering of IR Radiation from Clouds," *Appl. Opt.* 3, 197, 1964.

E. Bauer, "Energy Transfer Mechanisms in Hypersonic Shocks," *JQSRT* 2, 499, 1969.

E. Bauer, "Physics of the Upper Atmosphere: Lecture Notes," IDA P-811 (DTIC: AD-736 257), January 1972.

E. Bauer, "Dispersion of Tracers in the Atmosphere and Ocean: Survey and Comparison of Experimental Data," *J. Geophys. Res.*, 79, 789, 1974.

E. Bauer, "A Catalog of Perturbing Influences on Stratospheric Ozone, 1955-75," *J. Geophys. Res.*, 84 (C11), 6929, November 1979.

E. Bauer, "The Growth and Disappearance of Tracer Clouds in the Atmosphere," IDA N-890, June 1983.

E. Bauer, L.S. Bernstein, and G.M. Weyl, "Cirrus Clouds, Some Properties and Effects on Optical Systems: A Preliminary Examination," IDA P-1743 (AD-B082556), January 1984.

E. Bauer, "Physics of High-Temperature Air-I, Basics," IDA D-487, in publication, 1990.

E. Bauer, "Uncertainties in the Prediction of High-Altitude Nuclear Effects, IDA D-721, in publication, 1990.

E.A. Bertoni, "Clear and Cloud-Free Lines-of-Sight from Aircraft," AFGL-TR-77-0141 (AD A-046352), June 1977.

R.L. Bogusch and F.W. Giugliano, "Nuclear Survivability Criteria for Satellite Links (U)," AFWL-TR-82-18 (AD C-009 854L), October 1982 (SECRET/RESTRICTED DATA).

M. Born and E. Wolf, *Principles of Optics*, Pergamon, NY; 6th Ed., 1986.

H.L. Brode, "Review of Nuclear Weapons Effects," *Annu. Rev. Nucl. Sci.* 18, 153, 1968.

J. Carpenter, "Examination of Nuclear Effects," Briefing at POET, February 1989.

S. Chapman and T.G. Cowling, *The Mathematical Theory of Non-Uniform Gases*, Cambridge University Press, 2nd Ed., 1952.

CIRA-72 (COSPAR International Reference Atmosphere, 1972), Akademie Verlag, Berlin, 1972.

J.B. Cladis et al., "Trapped Radiation Handbook," DNA-2524H, revised, November 1973.

S.A. Clough et al., "FASCODE-3 for Spectral Simulation," presented at IRS-88, *Current Problems in Atmospheric Radiation*, J. Lenoble and J. Jelyn, Eds., Deepak Publications, VA, 1989. AFGL manual for the Code is in preparation.

R.N. Colwell, Ed., "Manual of Remote Sensing," Vol. I, American Society for Photogrammetry, Falls Church, VA, 1983.

R. Courant and K.O. Friedrichs, *Supersonic Flow and Shock Waves*, Interscience, NY, 1948.

E. de Bary and F. Moeller, "The Vertical Distribution of Clouds," *J. Appl. Meteorology* 2, 806, 1963.

D. Deirmendjian, "Scattering and Polarization Properties of Water, Clouds, and Hazes in the Visible and Infrared," *Appl. Opt.* 3, 187, 1964.

R. DeViolini, A. Shlanta and C.B. Elam, Jr., "Seasonal Cloud Amount and CFLOS Data for Selected Ocean Regions," OCAMO Project, Pacific Missile Test Center, 30+ reports, 1980-1982.

DNA 6500 H "Nuclear Warhead Modeling Handbook (U)," prepared by LANL and LLNL, December 1981 (SECRET/RESTRICTED DATA/CRITICAL NUCLEAR WEAPON DESIGN INFORMATION).

R.G. Ellingson, "On the Effects of Cumulus Dimensions on Longwave Irradiance and Heating Rate Calculations," *J. Atmos. Sci.* 39, 886, 1982.

W.G. Elliott, "Measurement of IR Earth Background from High Altitudes (U)," *Proc. IRIS* 6, #3, 1, 1961, SECRET.

EM-1, *DNA Effects Manual Number 1* "Capabilities of Nuclear Weapons (U)," (First edition July 1972) (AD 526125 and AD 526126)--revision in progress (SECRET/RESTRICTED DATA).

ENW 64,77, *The Effects of Nuclear Weapons* (DOD and DOE, S. Glasstone and P. Dolan, Eds., 1964 and 1977, respectively).

R.P. Espinola, "Spatial and Spectral Properties of Cloud Backgrounds from 2.65 to 2.95 μm ," SRI Report for USAF/SAMSO (AD-869403), January 1970 (U/LIMITED).

L.E. Ewing and T.J. Barrett, "Simplified Models of Weapon Effects," MRC-N-795 (Revised), July 1989.

S. Feldman, "Hypersonic Gas Dynamic Charts for Equilibrium Air," AVCO-Everett RR-40 (Everett, MA) 1957.

F.K. Fye, "The AFGWC Automated Cloud Analysis Model," USAF Global Weather Center, Offutt AFB, NE, Tech. Memo 78-002, June 1978.

C. Gazley, "Atmospheric Entry," Ch. 10 in *Handbook of Astronautical Engineering*, H.H. Koelle, Ed., McGraw-Hill, NY, 1961.

F.R. Gilmore, "Equilibrium Composition and Thermodynamic Properties of Air to 24,000 K," RAND Report RM-1543 (AD-84052), 1955.

R.M. Goody and Y.L. Yung, *Atmospheric Radiation- Theoretical Basis*, Oxford U. Press, 2nd Ed., 1989. (First Ed.-Goody, 1964).

K.D. Hage et al., "Particle Fallout and Dispersion in the Atmosphere," Travelers Research Center Report SC-CR-66-2031, prepared for Sandia Corp., available from NTIS, 1966.

K.D. Hage, "Particle Fallout and Dispersion below 30 km in the Atmosphere," Travelers Research Center Report SC-DC-64-1463, prepared for Sandia Corp., available from NTIS, 1964.

W.D. Hayes and R.F. Probstein, *Hypersonic Flow Theory, Vol. I, Inviscid Flows*, Academic Press, NY, 2nd Ed., 1966.

HELPH-I = *High-Energy Laser Propagation Handbook--I. Phenomenological Basis*, OptiMetrics for ASL, ASL-TR-0148 (AD-B106 243), February 1984.

G. Herzberg, *Molecular Spectra and Molecular Structure--I, Spectra of Diatomic Molecules*, Van Nostrand, NJ, 1950.

D.F. Higgins, K.S.H. Lee, and L. Marin, "System-Generated EMP," *IEEE Trans. on Antennas and Propagation*, Vol. AP-26 (#1), 14, January 1978.

J.O. Hirschfelder, C.F. Curtiss, and R.B. Bird, *Molecular Theory of Gases and Liquids*, J. Wiley, NY, 1954, 1964.

P.V. Hobbs, "Scales Involved in the Formation and Organization of Clouds and Precipitation," in P.V. Hobbs and A. Deepak, Eds., *Clouds--Their Formation, Optical Properties, and Effects*, Academic Press, 1981.

H. Hoerlin, "United States High-Altitude Test Experiences," LANL Monograph LA-6405, October 1976.

D.H. Holland, Ed., "Physics of High-Altitude Nuclear Bursts," DNA Report 4501 F, December 1977.

C.H. Humphrey, "Cloud Scattering Backgrounds in the MWIR--Vol. II, Specular Scattering (U)," Visidyne Inc., Report AFGL-TR-84-0223, August 1984, SECRET.

IR Handbook, Wolfe and Zissis, Eds., ERIM for ONR, Rev. Ed., 1985.

Jane's Armor & Artillery, 1986-87 Edition.

J.D. Jackson, *Classical Electrodynamics*, Wiley, 2nd Ed., 1975.

J.H. Jeans, *Introduction to the Kinetic Theory of Gases*, Cambridge University Press, 1982.

J.H. Jeans, *Dynamical Theory of Gases*, Cambridge University Press, 4th Ed., 1925.

F. Kasten, "Falling Speeds of Aerosol Particles," *J. Appl. Meteorol.* 7, 944, 1968.

B.S. Katz, F.C. DeBold, and J.J. Perez-Esandi, "Estimates for the Probabilities of Surface-to-Air Cloud-Free Lines of Sight and Low Cloud Statistics from Ship Observations, Part 1, 15 Marine Locations," Naval Surface Weapons Center, Silver Spring, MD, Report NSWC-TR-78-143, November 1980.

R.B. Kiess and W.M. Cox, "The AFGWC Automated Real-Time Cloud Analysis Model (RTNEPH)," AFGWC-TN-88/001 (AB-B121 615), March 1988.

P.P. Kisliuk, "Backgrounds and the Defense Support Program (U)," Aerospace Corporation Report TOR-7709(4409-01)-1, June 1979, SECRET.

F. Kneizys et al., "Atmospheric Transmittance/Radiance: Computer Code LOWTRAN-5," AFGL-TR-80-0067 (AD-A088 215), 1980.

F. Kneizys et al., "Users Guide to LOWTRAN-7", AFGL-TR-88-0177, Aug. 1988.

A.N. Kolmogorov, "The Local Structure of Turbulence in Incompressible Viscous Fluids for Very Large Reynolds Numbers," *Dokl. Akad. Nauk SSSR*, 30, 301, 1972.

D.P. Kratz and R.D. Cess, "IR Radiance Models for Atmospheric Ozone," *J. Geophys. Res.* 93, 7047, 1988.

H. Kruger, "Nuclear Hardening of Optical Sensors," LLNL Report CD-88-0078, June 1988.

J.D. Kuethe, *Foundations of Aerodynamics*, Wiley (2nd Ed. 1950, with J.D. Schetzer, 4th Ed. 1988, with C.Y. Chow).

S.M. Kulpa and E.A. Brown, "Near-Millimeter Wave Technology Base Study, Vol. I Propagation and Target/ Background Characteristics," Harry Diamond Labs., Report HDL-SR-79-8, November 1979.

P.E. Lehr, R.W. Burnett, H.S. Zim, *Weather*, Golden Press, NY, 1965.

R. Leong et al., "AFWL Exoatmospheric Nuclear Radiation Environment Prediction and Shielding Codes Applicable to the Strategic Defense Initiative (SDI)," Draft Report, Air Force Weapons Laboratory, Air Force Systems Command, Kirtland Air Force Base, NM, May 1986.

R.J. List, Ed., "Smithsonian Meteorological Tables," 6th Revised Ed., Smithsonian Institution, Washington, DC, 1951.

J.M. Livingston and J.D. Malick, "Analysis of SAGE Limb-Path Transmission and Particulate Extinction Data for 1979," SRI International Report, Project 4578, for Naval Air Development Center, February 1983.

J.G. Logan and C.E. Treanor, "Tables of Thermodynamic Properties of Air from 3000 K to 10,000 K," Report No. BE-1007-A-3, CALSPAN Corporation, Buffalo, NY, 1957.

C.B. Ludwig et al., *Handbook of IR Radiation from Combustion Gases*, NASA SP-3080, NASA/Marshall SFC, 1973.

I.A. Lund, "Methods for Estimating the Probability of Clear Lines of Sight, or Sunshine, through the Atmosphere," *J. Appl. Meteorol.*, 5, 625, 1966.

I.A. Lund, "Estimating the Probability of a Clear Line-of-Sight from Sunshine and Cloud Cover Observations," *J. Appl. Meteorol.* 4, 714, 1965.

I.A. Lund, "Universal Methods for Estimating Probabilities of Cloud-Free Lines of Sight through the Atmosphere," *J. Appl. Meteorol.* 12, 28, Feb. 1973.

I.A. Lund and M.D. Shanklin, "Photogrammetrically Determined Cloud-Free Lines of Sight through the Atmosphere," *J. Appl. Meteorol.* 11, 773, August 1972.

I.A. Lund, D.D. Grantham, and C.B. Elam, Jr., "Atlas of Cloud-Free Line-of-Sight Probabilities, Part 1, Germany," AFCRL-TR-75-0261, May 1975.

J.D. Malick and J.H. Allen, "Impact of Cloud Cover on Electro-Optical Systems, System Design Handbook (U)," SRI International Technical Reports to DARPA, 1978-1979, SECRET.

J.J. Martin, *Atmospheric Reentry: an Introduction to its Science and Engineering*, Prentice-Hall, 1966.

L.T. Matveev, "Cloud Dynamics," D. Reidel, Boston, 1984.

R.A. McClatchey et al., "Optical Properties of the Atmosphere (3rd Ed.)," AFCRL-72-0497 (AD-753075), 1972.

R.A. McClatchey et al., "Optical Properties of the Atmosphere," AFCRL-70-0527, 1970.

M.P. McCormick et al., "Satellite Studies of the Stratospheric Aerosol," *Bull. Am. Meteorol. Soc.* 60, 1038, September 1979.

M.P. McCormick et al., "SAM II Measurements of the Polar Stratospheric Aerosols, Vol. II," *NASA Ref. Publication* 1088, March 1982.

W. McNamara, "Analytic Heave Model Review and Documentation," DNA-TR-85-144, February 1985.

R.W. Middlestead, R.E. LeLevier, and M.D. Smith, "Satellite crosslink communications vulnerability in a nuclear environment," *IEEE J. on Sel. Areas Commun.*, Vol. SAC-5, No.2, 138, February 1987.⁹⁴

S.R. Murty, "Endo Heating Theory: Code RVTEMP," unpublished notes, Teledyne Brown Engineering, Huntsville, AL, August 1987.

R.J. Nelson and M.B. Wetherbe, "Some Aspects of Estimating the Probability of Cloud-Free Line-of-Sight in Dynamic Situations," USAF ETAC (Scott AFB, IL), TN-76-2, March 1976.

Chul Park, *Nonequilibrium Hypersonic Aerothermodynamics*, Wiley, NY, 1990

Perry, Ed., *Chemical Engineer's Handbook*, 4th Ed., McGraw-Hill, NY, 1963.

C.S. Ramage, "Prospects for Weather Forecasting," *Bull. Am. Meteorol. Soc.* 57, 4, 1976.

R.E. Rapp, C. Schutz, and E. Rodriguez, "Cloud-Free Line-of-Sight Calculations," *J. Appl. Meteor.* 12, 484, 1973.

P.J. Rausch et al., RDA, "Characterization of Dust Environments for the F-107, TF-33, and J-57 Engine Tests (U)," DNA-TR-87-106, March 1988 (SECRET/FORMERLY RESTRICTED DATA).

⁹⁴ This very nice article has a number of misprints. R_b in Eq. (5) is measured in bits/s, while in Table 5 R_b is measured in Mbits/s. Also the abscissa in Fig. 3 is not correct.

J.W. Reed et al., Visidyne, "Nuclear IR Data Review (U)," AFGL-TR-80-0184 (3 vols.), May 1980 (SECRET/RESTRICTED DATA).

L.S. Rothman et al., "The HITRAN Data Base: 1986 Edition," *Appl. Opt.* 26, 4058, 1987.

H. Schlichting, *Boundary Layer Theory*, McGraw-Hill, NY, 7th Ed., 1979.

R. Scorer, *Clouds of the World*, Lothian Publishing Co., Melbourne, Australia, 1972.

R.D. Sharma et al, "Description of SHARC, the Strategic High-Altitude Radiance Code", AFGL-TR-89-0229, Aug. 1989.

G.K. Soper, Jr., Ed., "The Nuclear Electromagnetic Pulse (EMP) (U)," *J. Defense Research Special Issues* 84-1, May 1985 (SECRET/RESTRICTED DATA).

D.H. Sowle, "Analytic Fluid Dynamics," Ch. 10 in PHANB, 1977.

Yu. V. Spiridonova, "Scales of Cloud Formations and the Classification of Cloudiness Fields on the Basis of Satellite Data," *Trudy VNIIGMI-MTsD*, No. 2, 63, 1976.

T.L. Stephens, "The NORSE Manual, Vol. 5-3: Handbook of NORSE Predictions," Draft prepared by PRi for DNA, June 1986, Rev. February 1987.

E. Storm and H.I. Israel, "Photon Cross Sections from 1 KeV to 100 MeV for Elements Z=1 to Z=100," *Nuclear Data Tables A7*, 565, 1970.

G.W. Sutton, "The Initial Development of Ablation Heat Protection, an Historical Perspective," *J. Spacecr. Rockets*, 19, 3, 1982.

R.E. Turner and C.K. Hill, Eds., "Terrestrial Environment (Climatic) Criteria Guidelines for Use in Aerospace Vehicle Development, 1982 Revision," NASA Technical Memorandum 82473, 1982.

USAF 65 = "USAF Handbook of Geophysics and the Space Environment," S.L. Valley, Ed., 1965.

USAF 85 = "USAF Handbook of Geophysics and the Space Environment," A.S. Jursa, Ed., 1985.

H.C. Van de Hulst, *Light Scattering by Small Particles*, J. Wiley, NY, 1957.

W.W. White et al., "A SCENARIO Code Simulation of 1000 High-Altitude Nuclear Explosions (U)," DNA-TR-87-172, June 1987a (CONFIDENTIAL/RESTRICTED DATA).

W.W. White et al, "1986 DNA Atmospheric Effects Summer Study (U), Vol. I, High-Altitude Phenomenology (U)", DNA-TR-87-181-V1, Sept. 1987, p. 56 (CONFIDENTIAL/ FORMERLY RESTRICTED DATA).

W.W. White, in "User Manual for SCENARIO, Version 4.0", D.A. Landman and P.J. Ricchiazzi, DNA-TR-89-204, December 1989.

W.L. Wolfe and G.J. Zissis, Eds., *IR Handbook*, ERIM for ONR, Rev. Ed., 1985.

K.L. Wray, "Chemical Kinetics of High Temperature Air," p. 181 f in F. Riddell, Ed., *Hypersonic Flow Research*, Academic Press, NY, 1962.

S.J. Young, "Scattering of Solar Radiation by Clouds," Aerospace Report SAMSO-TR-78-178, December 1978. See also "Diffuse Reflection of Clouds: A Semiempirical Model," *Appl. Opt.* 18, 1881, June 1979.

Ya. B. Zeldovich and Yu. P. Raizer, *Physics of Shock Waves and High-Temperature Hydrodynamic Phenomena*, Academic Press, NY, 2 Vols., 1966, 1967.

APPENDIX E

**FORMAL ASPECTS OF THE EQUATIONS OF
GAS DYNAMICS**

APPENDIX E

FORMAL ASPECTS OF THE EQUATIONS OF GAS DYNAMICS

This Appendix sketches how one can derive the equations of gas dynamics-which express conservation of mass, momentum, and energy- from the Boltzmann Equation.^{E-1} Solutions in successive powers of the ratio of the gas-kinetic mean free path, l_{gk} , to a characteristic dimension of the flow, L , give first the Euler equations $\{O(l_{gk}/L)^0\}$ which have no explicit collisional terms, then the Navier-Stokes Equations $\{O(l_{gk}/L)^1\}$ which introduce the transport coefficients of viscosity, diffusivity, and thermal conductivity, which are proportional to the first power in l_{gk} .^{E-2}

The distribution function $f = f(\underline{x}, \underline{v}, t)$ is a solution of the Boltzmann equation:

$$\partial f / \partial t + (\underline{v} \cdot \text{grad}) f + (\underline{X} \cdot \text{grad}_{\underline{v}}) f = D_c f \quad , \quad (\text{E.1})$$

where \underline{X} = force per unit mass (which is here put equal to zero) and D_c is the usual collision term. If there are n particles (of mass m) per unit volume, then the density ρ , the flow velocity \underline{u} , and the temperature T are defined by the standard expressions:

$$\rho = m \int f d^3 \underline{v} = m \cdot n \quad (\text{E.2})$$

$$\underline{u} = (1/n) \int f \underline{v} d^3 \underline{v} \quad (\text{E.3})$$

$$T = (1/nR) \int V^2 f d^3 \underline{v} = p / R \rho \quad , \quad (\text{E.4})$$

where the V is the velocity relative to the mean flow:

$$\underline{V} = \underline{v} - \underline{u} \quad . \quad (\text{E.5})$$

The pressure tensor P_{ij} ($i, j = 1, 2, 3$) and the heat flux vector \underline{q} are given by the expressions:

E-1 See, e.g. Chapman & Cowling, 1952, or Hirschfelder, Curtiss, and Bird, 1954, 1964, for a discussion of this fundamental equation.

E-2 The next iteration, with terms $O(l_{gk}/L)^2$ gives the Burnett and Grad-Maxwell 13 moment approximations, but this is rarely attempted.

$$P_{ij} = m \int V_i V_j f d^3 \underline{v} = p \delta_{ij} - \tau_{ij} \quad (E.6)$$

$$\underline{q} = (m/2) \int \underline{v} V^2 f d^3 \underline{v} , \quad (E.7)$$

where τ_{ij} is the (symmetric) stress tensor, and conventionally

$$\delta_{ij} = 1 \text{ if } i = j ; 0 \text{ if } i \neq j . \quad (E.8)$$

To obtain the macroscopic flow equations, one takes the Boltzmann equation (E.1), multiplies by

$$\psi^{(c)} = m ; \psi^{(m)} = m \underline{v} ; \psi^{(e)} = (m/2) V^2 + \text{internal energy} , \quad (E.9)$$

and integrates over 3-dimensional velocity space, $\int d^3 \underline{v}$. On account of the conservation laws for mass (c), momentum (m), and energy (e) before and after collisions, the collision term vanishes:

$$\int \psi^{(a)} D_c f d^3 \underline{v} = 0 ; a = c, m, e , \quad (E.10)$$

and thus one gets the result

$$0 = \partial(n\psi^{(a)})/\partial t + \text{div } n \langle \psi^{(a)} \underline{v} \rangle_{av} - n \langle \partial \psi^{(a)} / \partial t \rangle_{av} - n \langle (\underline{v} \cdot \text{grad}) \psi^{(a)} \rangle_{av} - n \langle \underline{X} \cdot \text{grad} \psi^{(a)} \rangle_{av} ; a = c, m, e , \quad (E.11)$$

where

$$\langle K \rangle_{av} = (1/n) \int K f d^3 \underline{v} . \quad (E.12)$$

If one now substitutes Eq. (E.7) in (E.9), then one gets the macroscopic flow equations:

$$\text{Continuity (c): } \partial \rho / \partial t + \sum_{i=1}^3 \partial(r u_i) / \partial x_i = 0 \quad (E.13)$$

$$\text{Momentum (m): } \partial u_i / \partial t + \sum_{j=1}^3 [u_j \partial u_i / \partial x_j + (1/r) \partial P_{ij} / \partial x_j] = 0 \quad (E.14)$$

$$\text{Energy (e): } \partial p / \partial t + \sum_{i=1}^3 [\partial(p u_i) / \partial x_i + (2/3) \partial q_i / \partial x_i + (2/3) \sum_{j=1}^3 P_{ij} \partial u_j / \partial x_j] = 0 . \quad (E.15)$$

With the present customary form for the collision term $D_c f$ in the Boltzmann equation (E.1) which leads to the pressure tensor P_{ij} and the heat flux vector \underline{q} , the system of equations (E.13) to (E.15) is incomplete in that there are just five scalar equations but many more than five unknowns [ρ , p , u_i make five, plus τ_{ij} gives five more (a symmetric tensor has six independent components, but we have taken out p), plus q_i which makes 13 in all--cf. Hirschfelder, Curtiss, and Bird (1954), p. 492f]. Thus one must make appropriate assumptions for τ_{ij} and q_i in the equations of gas dynamics (E.13-15), and this is done by expanding the collision term $D_c f$ in powers of the ratio of gas-kinetic mean free

path, l_{gk} to a characteristic flow length L . The lowest order (Euler) approximation is obtained by putting all the collision terms equal to zero:

$$\tau_{ij}^{(0)} = 0 ; q_i^{(0)} = 0 \quad (i,j = 1,2,3) \quad . \quad (E.16)$$

The Euler equations are useful for explaining fluid flows when the only applied forces are normal, i.e. pressure. However, there is no friction as long as Eq. (E.16) applies, and thus the fluid cannot sustain shearing forces, such as the drag force on a surface in the fluid.

The next order term in the expansion, $O(l_{gk}/L)$, gives the Navier-Stokes approximation:

$$\tau_{ij}^{(1)} = \mu \partial u_i / \partial x_j ; q_i^{(1)} = -k \partial T / \partial x_i \quad , \quad (E.17)$$

which introduces the viscosity coefficient μ and the thermal conductivity k . These quantities depend on collisions of gas molecules with one another and with surfaces, and can be expressed in terms of the elementary kinetic theory of gases as follows^{E-3}:

$$\mu = (1/3) \rho v_a l_{gk} \quad (E.18)$$

$$k = f \mu c_v \quad (E.19)$$

$$D = (1/3) v_a l_{gk} \quad , \quad (E.20)$$

where the thermal mean speed v_a and the sound speed a are given as^{E-4}

$$v_a = \sqrt{8kT/\pi M} \quad (E.21a)$$

$$a = \sqrt{\gamma kT/M} \quad . \quad (E.21b)$$

Here c_v is the specific heat at constant volume per unit mass, D is the diffusion coefficient, l_{gk} is the gas-kinetic mean free path

$$l_{gk} = 1/(\sigma_{gk} n \sqrt{2}) \quad , \quad (E.22)$$

where σ_{gk} is the gas-kinetic collision cross section [$\sim (3-6) \times 10^{-15} \text{ cm}^2$ --see, e.g., Section 2.5, Eq. (3.28) for another application] and $n = \rho/M$ = no. of molecules per unit

E-3 The numerical coefficients in Eqs. (E.18) and (E.20) are respectively $5\pi/32 = 0.489$ and $3\pi/16 = 0.587$ for a rigid sphere, while f in Eq. (E.19) is the "Eucken factor" $(9\gamma - 5)/4 \sim 2-2.5$ with $\gamma = c_p/c_v$ (see, e.g., Hirschfelder, Curtiss, and Bird, 1954, p. 13ff).

E-4 Note that in Eq. (E.21) k is the Boltzmann constant, not the thermal conductivity which is here written as k .

volume. For the other numerical coefficients in Eq. (E.21) and (E.22), see, e.g., Jeans (1925, 1982).

The equations of fluid mechanics are non-linear and very difficult to solve in general. Traditionally aerodynamicists use similarity solutions to a great extent, with a number of dimensionless parameters which are discussed briefly in Section 5.5 and Table 5.3 in the text.

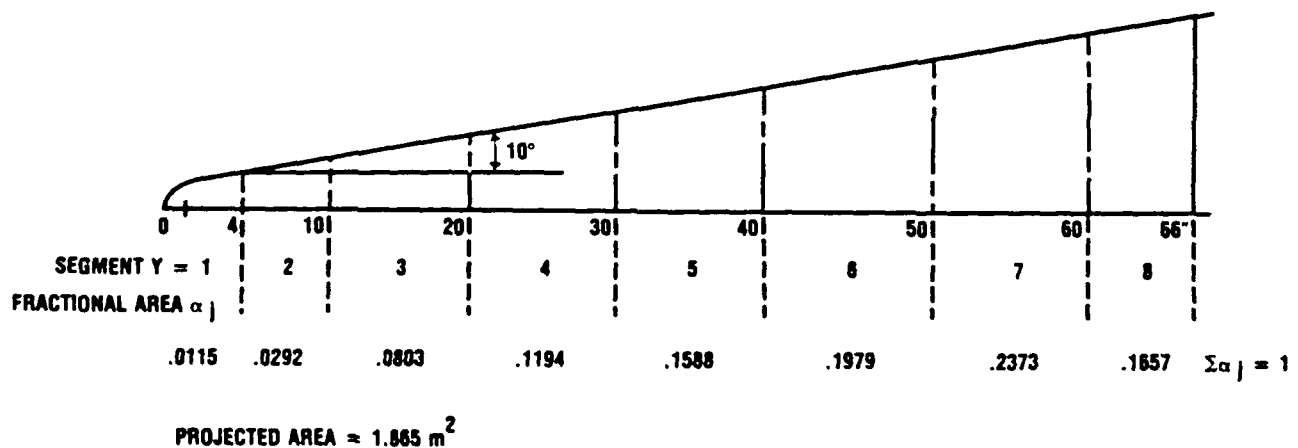
APPENDIX F

**SOME DETAILS OF THE CALCULATION OF
RV OPTICAL SIGNATURES**

APPENDIX F

SOME DETAILS OF THE CALCULATION OF RV OPTICAL SIGNATURES

Here we present some details of the calculation of reentry vehicle optical signature from Section 5.9. The geometrical profile of the RV is shown in Fig. F.1 which shows the eight segments into which the body is broken up for purposes of computation. The computation of the thermal emission signal in terms of the contributions of these eight segments is outlined in Table F.1.



11-10-66-7

Figure F.1. Simplified Geometrical Profile of an RV

Table F.1. Thermal Emission Signal Computation

A. To Compute Thermal Radiance ($W/m^2\text{-sr-}\mu m$) at the Higher Altitudes

Segment j	1	2	3	4	5	6	7	8
Fractional area α_j	.011	.029	.080	.12	.16	.20	.24	.17
<u>h = 300 kft. (91 km)</u>								
$T_j(K)$	810	560	477	422	394	377	-----	
$B(0.5, T_j)$	1.4E-6	2E-13	2E-17	9E-21	7E-23	3E-24		
$B(3.5, T_j)$	1400	150	41	13	7	4		
$B(12, T_j)$	140	64	42	30	24	20	$\Sigma_j \alpha_j B(\lambda, T_j)$	
$\alpha_j B(0.5, T_j)$	1.6E-8	5E-15	2E-18	1E-21	1E-23	2E-24	1.6E-8	
$\alpha_j B(3.5, T_j)$	16	4	3	2	1	3	29	
$\alpha_j B(12, T_j)$	2	2	3	4	4	13	27	
<u>h = 150 kft. (46 km)</u>								
$T_j(K)$	2590	2200	1420	1090	920	870	810	780
$B(0.5, T_j)$	5.7 E4	8 E3	6	1 E-2	1 E-4	2 E-5	1 E-6	4 E-7
$B(3.5, T_j)$	5.8 E4	4.1 E4	1.3 E4	5.3 E3	2.6 E3	2.0 E3	1.4 E3	1.2 E3
$B(12, T_j)$	810	660	360	240	180	160	140	130
$\alpha_j B(0.5, T_j)$	660	230	0.5	-				* 900
$\alpha_j B(3.5, T_j)$	670	1210	1070	640	420	400	340	190 * 5000
$\alpha_j B(12, T_j)$	9	19	29	29	28	32	33	22 * 200

Table F.1 (continued)

B. Thermal Emission Signal for Different Conditions

h	(kft)	300	150	75	25
	(km)	91	46	23	7.6
T	(K)	Variable- see A, above		2590	700
• $\lambda = 0.5 \mu\text{m}$: $\sum_j \alpha_j B(0.5, T_j)^*$		1.6 E-8	900	57000	5.3 E-9
$L_{T,\theta}^{**}$		1.5 E-8	840	53000	4.9E-9
• $\lambda = 3.5 \mu\text{m}$: $\sum_j \alpha_j B(3.5, T_j)^*$		29	5000	58000	640
$L_{T,\theta}^{**}$		38	6500	76000	840
• $\lambda = 12 \mu\text{m}$: $\sum_j \alpha_j B(12, T_j)^*$		27	200	810	110
$L_{T,\theta}^{**}$		45	340	1400	180

* $\text{W/m}^2\text{-sr-}\mu\text{m}$

** $\text{W/sr-}\mu\text{m}$, i.e., we have multiplied $\sum \alpha B(\lambda, T)$ by ϵA_b , ϵ from Table 5.4 and $A_b = 1.9 \text{ m}^2$ from Eq. (5.24).

APPENDIX G

**THE ILLUMINATION OF A FLAT PLATE
BY EARTHSINE**

APPENDIX G

THE ILLUMINATION OF A FLAT PLATE BY EARTHSHINE

The problem for a flat plate is defined in Fig. 5.7--see also Eqs. (5.29) and (5.30). Because of its complexity, I display how one evaluates the integral over energy radiated from various elements of the earth's surface:

$$E^*_{T,E} = \int dA_E \epsilon_E(\lambda) B(\lambda, T_E) \cos \phi_1 [R_E(\phi_a)]^{-2} \tau_E^{\cos \phi_a} . \quad (G.1)$$

After diffuse reflection from the target, the effective radiance seen by the sensor is

$$L_{T,E} = E^*_{T,E} \cos \phi_2 (\rho/\pi) . \quad (G.2)$$

To evaluate the integral in Eq.(G.1), change the coordinate ϕ_1 to $(\phi_a + \beta)$ --see Fig. G.1:

$$\phi_1 = \phi_a + \beta$$

$$s = R_E \tan \phi_a ; ds = R_E \tan^2 \phi_a d\phi_a \quad (G.3)$$

$$dA_E = 2 \pi R_E^2 \tan \phi_a \sec^2 \phi_a d\phi_a$$

$$R_E = R_E \sec \phi_a ; \tau_E(\phi_a) = \tau_E \sec \phi_a$$

and thus

$$E^*_{T,E} = 2 \pi \epsilon(\lambda) B(\lambda, T_E) I_T(\tau_E, \beta) , \quad (G.4)$$

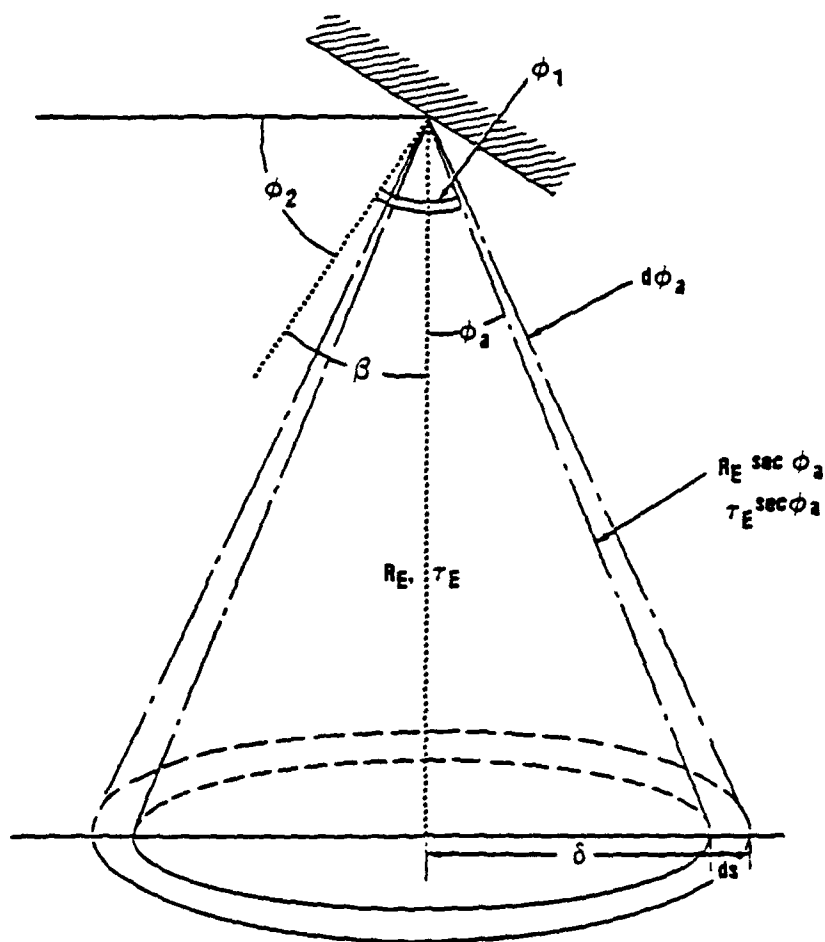
where

$$I_T(\tau_E, \beta) = \left\{ \int_0^\beta + (1/2) \int_{\beta}^{\pi/2} \right\} \tan \phi_a \cos(\phi_a + \beta) e^{-b \sec \phi_a} d\phi_a . \quad (G.5)$$

Here,

$$b = \ln(1/\tau_E) , \quad (G.6)$$

and the region of integration is split because a portion of the (2π) steradian seen from the earth is screened at an angle of attack $\beta \neq 0$. $I_T(\tau_E, \beta)$ is well behaved and falls off rapidly with increasing ϕ_a unless $b = 0$, i.e., unless $\tau_E = 1$.



7-28-61-7

Figure G.1. Sketch for the Evaluation of Eq. (G.1)

I have evaluated $I_T(\tau_E, \beta)$ for the representative case $\beta = \pi/4$, when Eq. (G.5) becomes

$$I_T(\tau_E, 45^\circ) = \int_0^{45^\circ} \tan \phi (\cos \phi - \sin \phi) e^{-b \sec \phi} d\phi / 2^{1/2} \quad (G.7)$$

Numerical values for $I_T(b)$ are shown in Fig. G.2 for $\beta = 45^\circ$.

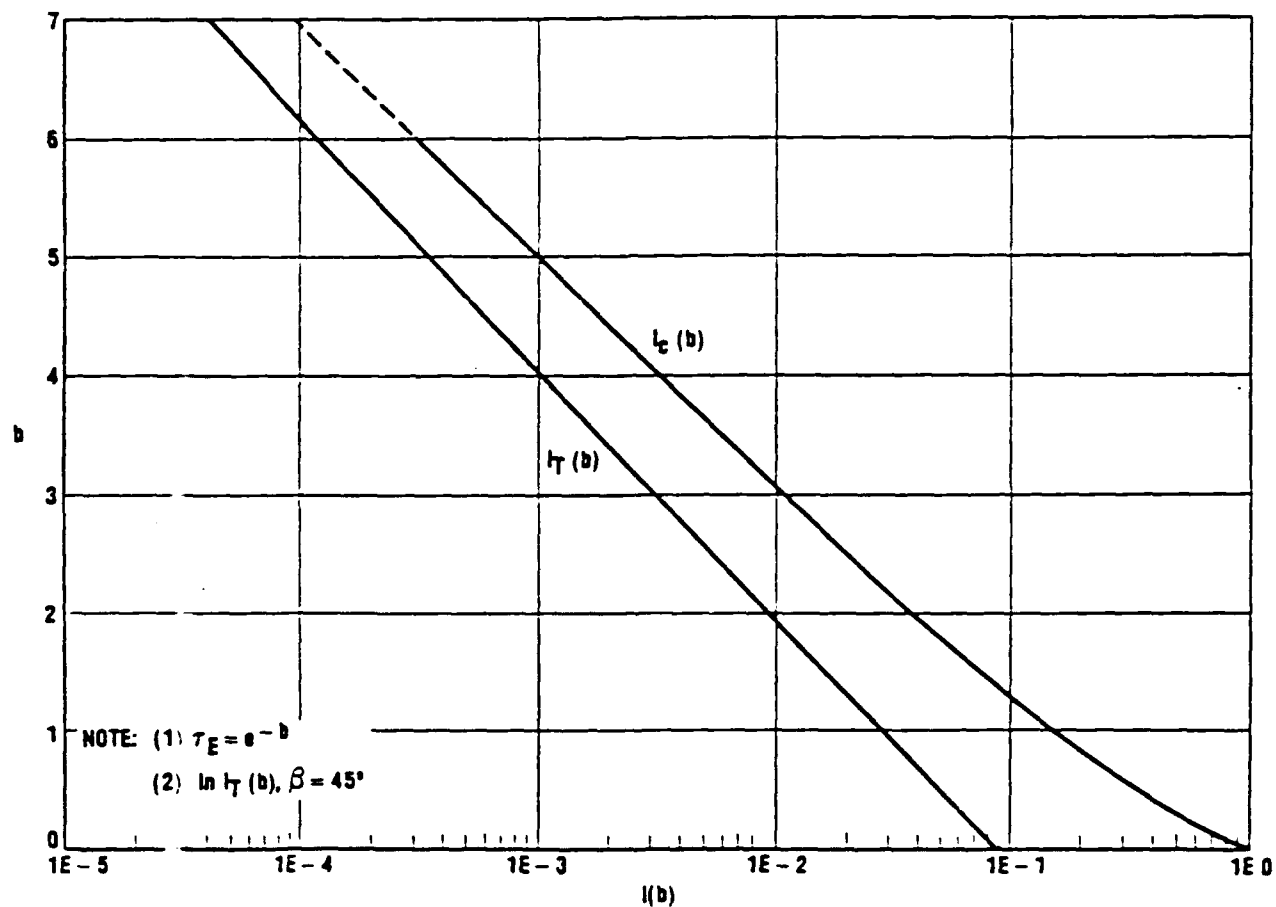


Figure G.2. The Integral $I(b)$

APPENDIX H

**ELECTROMAGNETIC-RADIATION EFFECTS ON
ELECTRICAL AND ELECTRONIC SYSTEMS**

(J. Malik, LANL, from Hoerlin, 1976)

APPENDIX H
ELECTROMAGNETIC-RADIATION EFFECTS ON
ELECTRICAL AND ELECTRONIC SYSTEMS
(J. Malik, LANL, from Hoerlin, 1976)

The electromagnetic radiation in the radio-frequency portion of the spectrum (EMP) can cause problems in electronic systems. The pulse from detonations above about 30 km is caused by the deflection of Compton electrons produced by gamma-ray interaction with the earth's magnetic field in the deposition region (20-40 km). The resulting transverse current in the large area of gamma-ray deposition produces a large coherent radiating element. With appropriate yield, detonation altitude and magnetic azimuth, the electric fields over large areas at the earth's surface can exceed 10^4 V/m. Such fields can cause detrimental effects on some types of electrical systems. The pulse width is less than a microsecond.

Starfish produced the largest fields of the high-altitude detonations; they caused outages of the series-connected street-lighting systems of Oahu (Hawaii), probable failure of a microwave repeater station on Kauai, failure of the input stages of ionospheric sounders and damage to rectifiers in communication receivers. Other than the failure of the microwave link, no problem was noted in the telephone system. No failure was noted in the telemetry system used for data transmission on board the many instrumentation rockets.

There was no apparent increase in radio or television repairs subsequent to any of the JI detonations. The failures were generally in the unprotected input stages of receivers or in rectifiers of electronic equipment; transients on the power line probably caused the rectifier failures. There was one failure in the unprotected part of an electronic system of the LASL Optical Station on top of Mount Haleakala on Maui Island. With the increase of solid-state circuitry over the vacuum-tube technology of 1962, the susceptibility of electronic equipment will be higher, and the probability of more problems for future detonations will be greater. However, if detonations are below line-of-sight, the fields and therefore system problems will be much smaller.

APPENDIX I

**SCATTERING OF SUNLIGHT
FROM A CLOUD**

APPENDIX I

SCATTERING OF SUNLIGHT FROM A CLOUD

I.1 INTRODUCTION

For the development of a space-based surveillance system in the atmospheric 2.7 μm absorption band the issue of false alarms due to the scattering of sunlight from clouds was addressed. An extensive experimental program using instruments mounted on high-altitude balloons and on U-2 high-altitude aircraft was conducted by Baird-Atomic--see Elliott, 1961, and Bauer, 1963, 1964, also Espinola, 1970.^{E-1}

The physics is quite different, depending on the wavelength between visible and LWIR and on the effective scattering angle. At wavelengths $< 4 \mu\text{m}$ a target can be seen principally because it scatters sunlight, while at the longer wavelengths (and at night) the principal contribution to the target signature comes from thermal emission from the body, with a relatively minor contribution from the scattering of earthshine (thermal emission from the surface of the earth and lower atmosphere). For large scattering angles,^{I-2} which is the case considered here, single scattering will predominate,^{I-3} while for small scattering angles (near-forward scattering) there are multiple scattering effects. Also, the size of the cloud can make a significant difference to its signature. Here we discuss some of these factors in a preliminary way, namely:

- a. Small versus large clouds
- b. Geometrical factors
- c. Effective diffuse reflectivity.

E-1 For more recent data and analyses, see Kisliuk, 1979, and Humphrey, 1984.

I-2 The scattering angle θ is so defined that $\theta = 0$ corresponds to forward scattering, $\theta = 180$ deg to back-scattering. See Fig. I-1.

I-3 For an empirical analysis of multiple scattering effects in this situation, see Young, 1978.

for the application of reflection rather than transmittance of sunlight. The scenario considered here is discussed in Section J.3, but first we distinguish between small and large clouds.

I.2 SMALL VERSUS LARGE CLOUDS

Given the scattering and extinction properties of cloud particles, one must distinguish between a small cloud in which all particles scatter the incident radiation, and a large cloud in which the incident radiation is extinguished within the cloud so that not all particles serve as scatterers of the incident radiation.

For a finite ("cubical") cloud of linear dimension L made up of n particles per unit volume, each of extinction/scattering cross sections σ_{ext} , σ_{sca} we define an extinction distance β^{-1} where

$$\beta = n \sigma_{\text{ext}} \quad . \quad (\text{I.1})$$

Consider a small cloud of dimension L , which is made up of $L^3 n$ (independent) scatterers, so that its total scattering cross section is

$$Q(\text{small}; \theta) = L^3 n (\partial \sigma_{\text{sca}} / \partial \Omega)_{\theta} \quad , \quad (\text{I.2})$$

where the mean differential cross section of a cloud droplet is given from Fig. 7.5. By contrast, for a *large* cloud, not all $L^3 n$ particles are available to provide effective scattering because the interior particles of the optically thick cloud, i.e., those which are more than a distance β^{-1} from the surface, are shielded from the incident solar radiation. Thus, the effective total number of scatterers is $L^2 \beta^{-1} n$, and so the total scattering cross section for a large cloud is

$$Q(\text{large}; \theta) = L^2 \beta^{-1} n (\partial \sigma_{\text{sca}} / \partial \Omega)_{\theta} = (L^2 / \sigma_{\text{ext}}) (\partial \sigma_{\text{sca}} / \partial \Omega)_{\theta} \quad . \quad (\text{I.3})$$

Equation (I.3) is only schematic in that there are some geometrical (angular) factors that have not been included here.

I.3 GEOMETRICAL FACTORS

Figure I.1 shows the geometry of the scattering process. We consider the coplanar problem with all of SA, DA, NA in the same plane so that

$$i + e + \theta = \pi \quad (\text{I.4a})$$

and also the condition of specular reflectance

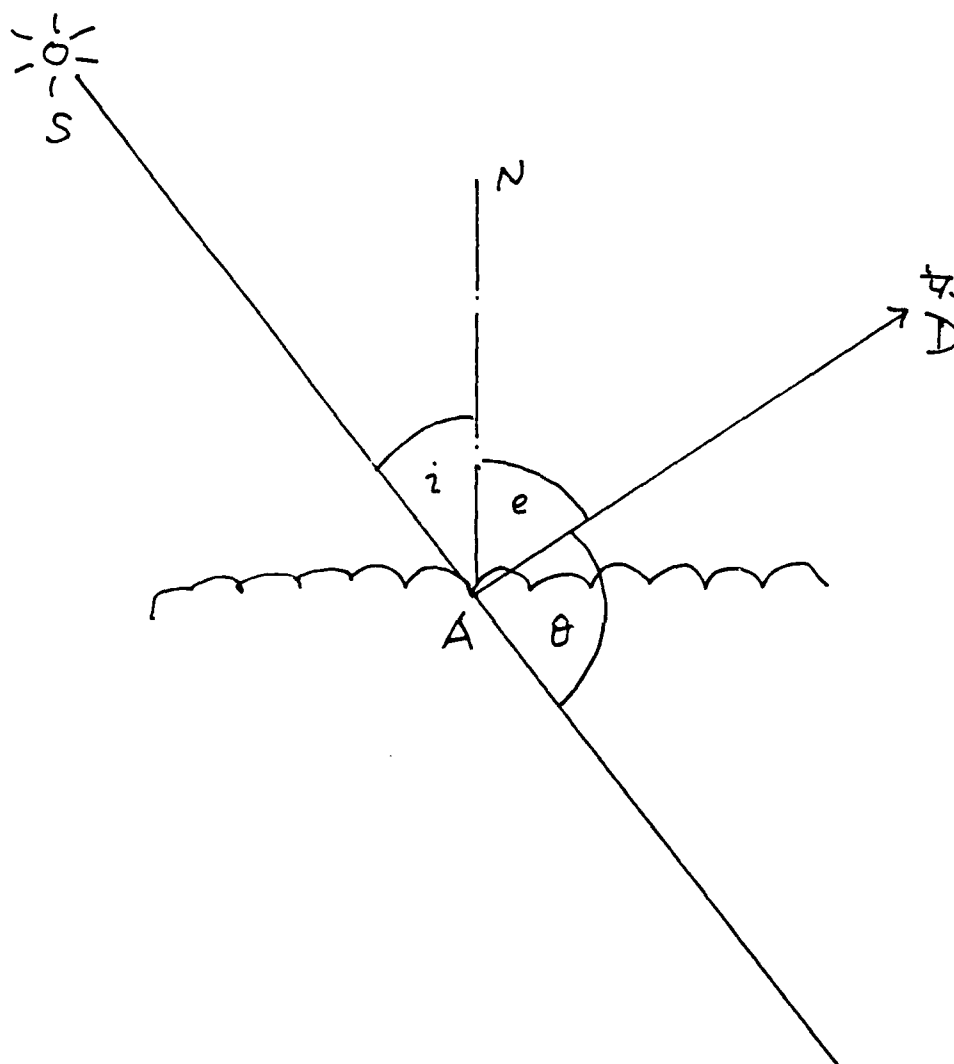


Figure I.1. Scattering Geometry

$$i = e \quad (I.4b)$$

which give the maximum amount of scattering for the case of specular reflection (which is not necessarily the case here).

It is clear that the actual scattering cross section Q (large; θ) of Eq. (I.3) actually depends on the macroscopic angles i , e , which determine the relation between the incident and reflected light beams relative to the macroscopic cloud as well as on the scattering angle θ for a particular particle, as represented by Fig. 7.4, 7.5, or I-2. It is useful to present a simple parameterization in terms of a Lambert's Law diffuse reflection coefficient $\eta(\theta)$, even though, as is pointed out in Bauer 1964, the description of a cloud as a Lambertian reflector is very poor, except possibly in the visible where there is a great deal of multiple scattering at small values of θ so that the single-scattering analysis is inappropriate.^{I-4}

We can define by the following expression (from Bauer, 1964^{I-5})

$$\eta_{\max}(\theta) = \pi (\partial \sigma_{\text{sca}} / \partial \Omega)_{\theta} [u \text{ (i.e.) } \sigma_{\text{ext}}]^{-1} \quad (I.5)$$

$$u \text{ (i.e.)} = 2 \cos i \cos e / \sin(\theta/2) \quad (I.6)$$

$$i = e = (\pi - \theta) / 2 \quad (I.4c)$$

Results at several different wavelengths are given in Fig. I.2; note that for $\theta < 30$ deg, $\eta > 1$ which clearly indicates that the formula for $\eta_{\max}(\theta)$ used here is inappropriate. At larger angles the reflectivity is fairly small.^{I-6} The physics of this is fairly easy to understand [cf., e.g., Bauer, 1964, below Eq. (3)]. Because the complex refractive index $N_1 - iN_2$ of the water droplets is not very different from one, the reflectivity at normal incidence from a plane slab, which is given by the expression

$$R = [(N_1 - 1)^2 + N_2^2] / [(N_1 + 1)^2 + N_2^2] \quad (I.7)$$

is quite small, comparable with the relative energy scattered through angles greater than 90 deg (see Table I.1).

I-4 Young, 1978, presented an empirical correction for multiple scattering effects.

I-5 It must be stressed that the expression for u is not a good one, although clearly something of this type is needed. There are problems both with the geometry and also with effects of single versus multiple scattering. Readers are solicited for a better expression!

I-6 The increased reflectivity in the visible for $\theta > 120$ deg is due to rainbow backscattering--see Fig. 7.4, 7.54, or I-2.

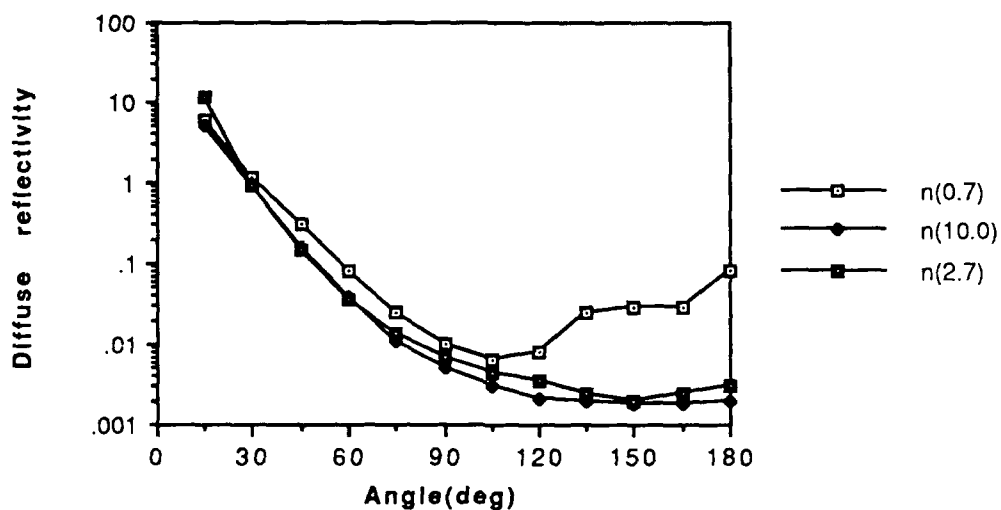


Figure I.2. Scattering From a Large Cloud at Different Wavelengths:
Effective Diffuse Reflectivity

Table I.1. Scattering Parameters at Different Wavelengths

Wavelength (μm)	0.7	2.7	10
$Q_{av} = 2\pi a_{av}/\lambda$ ($a_{av} = 4\mu\text{m}$)	36	9.3	2.5
σ_{sca}^* (10^{-6} cm^2)	1.45	1.38	
σ_{abs}^* (10^{-6} cm^2)	-	1.41	
σ_{ext}^{**} (10^{-6} cm^2)	1.45	1.45	1.45
$m = N_1 - iN_2^{***}$	1.331-3.05E-8	1.188-1.90E-2	1.218-5.08E-2
R [from Eq.(A.7)]	0.020	0.0074	0.010

* Bauer et al., 1984, p. 3-4--from E. Shettle, AFGL.

** σ_{ext} generally agrees with $2 \sigma_{geom} = 1.45$ to within a factor of 2 (Bauer et al., 1984, p. 3-4).

*** USAF, 1985, p. 18-16 (from E. Shettle).

The effective reflectivity R due to a slab of water (as against an assembly of particles) can be compared roughly with η ($\theta = 180$ deg). One would expect the actual reflectivity due to the particles to be smaller than R , especially in the LWIR where the Mie scattering parameter q_{av} for mean particle radius a_{av}

$$q_{av} = 2 \pi a_{av} / \lambda \quad (I.8)$$

is close to one, since if $q \ll 1$, there is very little scattering.

It must be stressed that the significance of the effective diffusivity is quite different at varying wavelengths. In the visible a target is seen by solar scattering, and at $\lambda = 2.7 \mu\text{m}$ the solar scattering is still greater than thermal emission in the daytime; but at $\lambda = 10 \mu\text{m}$ a cloud (or other target) is seen by its thermal emission supplemented by the scattering of earthshine, rather than by the scattering of sunlight.